Statistical mechanics of colloids and active matter in and out of equilibrium

Andrew Kaan Balin
St Cross College
University of Oxford

A thesis submitted for the degree of
Doctor of Philosophy

Trinity 2017

To my grandmother,
Marina Mitchell.

Acknowledgements

In completing this thesis, I am truly indebted to my supervisor, Julia Yeomans, for accepting me into her group and allowing me the freedom to explore and develop my interests. Indeed, the ambitious range of topics presented in this thesis would not have been possible without her appetite for exploring new ideas and questions, and her drive towards collaboration with the wider community. On that note, I would also like to express my gratitude to Dirk Aarts, Roel Dullens, Yongxiang Gao, and Arran Curran, with whom I have had the pleasure of collaborating.

A large part of this thesis would not have been possible were it not for the attention I received from Tyler Shendruk; I have benefited greatly from his knowledge, drive and contagious energy. I would also like to thank Amin Doostmohammadi and Andreas Zöttl for their mentorship on the various problems that we have tackled over the last couple of years.

Of course, I would never have begun this final chapter of my education were it not for those under whom I studied and researched while pursuing my undergraduate degree at the University of Warwick. To Rachel Edwards, Susan Stepney and Marzena Szymanska, I am very grateful. Not forgotten are the school teachers whose incalculable efforts gave me both the desire and the means to achieve what I have done, including Adam Laity, Peter Allen, Mark Vanstone, Chris Moncaster and Judith Eastburn to name only a few.

I would like to thank my good friends Dan and Russ for the $\mathcal{O}(10^5)$-message Facebook chat that has persisted between us for the last three years, providing a well from which I have drawn much mathematical and computational assistance — as well as some absolutely top bantz. A similar debt is owed to those I have shared office 4.10 with over the years: Arnold, Chico, Ferdinando, Luuk, and Matthew.

My time in Oxford would not have been the same without the new friends I've made along the way, including Amy, Angharad, Çınar, João, Mathijs, Mathura, the committee members I've served with in the St Cross College Common Room, and those I've had the pleasure of rowing with in Wolfson College Boat Club; I am similarly grateful for the continued friendship I have had from Angus, Ben, Chris, Dom, James, Mark and Sam. I am especially thankful to have met Anna, who has gotten me to escape Oxford for many a weekend trip, and without whom my time here would have been duller.

Lastly, I would like to thank my family for always providing me with the love and support that has allowed me to achieve everything I have done, both within this thesis and outside of it. To my Mum, Beverley; my Dad, Serdar; Peter, Alan, İlknur, and my Grandmother, Marina, I thank you all.

Abstract

Thermal and viscous forces compete for dominance at the microscopic lengthscales which govern the behaviour of many soft or biological systems. We study three systems of increasing complexity with the central goal of understanding the statistical or hydrodynamic nature of their mechanics.

First we study experiments that have been conducted on ferromagnetic colloidal rods. At equilibrium, the magnetically pinned rod is observed to randomly flip between two orientational states, which our theoretical analysis shows is due to a competition between entropic and Hamiltonian forces. We show analytically how entropic forces can arise by considering the coupling between observed and unobserved variables of a system.

Experiments in which a rod is driven out of equilibrium by a rotating field display three phases of steady-state behaviour as a function of driving frequency. Using Brownian dynamics simulations we match the lower critical frequency to the experimentally obtained values, showing that thermal fluctuations play an important role in this regime and propose a simple argument to demonstrate that hydrodynamic interactions between the substrate and rod affect the upper critical frequency.

We then turn to the biophysical topic of cell locomotion in viscoelastic media. In order to study how bacterial flagella interact with similarly-sized polymers in their environment, we construct a Stokesian dynamics model of a helical filament and bead–spring polymer. Simulating their interaction first for a pinned–rotating helix, then for a swimming helix, we demonstrate that large polymers become hydrodynamically entrained by the flagellum and coil around it, causing both pinned and swimming flagella to expend more work. For the swimming helix, this results in a reduction of swimming speed on average.

Finally, we consider an active nematic fluid confined to a channel and show that the inclusion of a passive colloid induces a global state of coherent flow maintained by the intrinsic activity of the system. This flow is persistent, and transports the colloid with it along the channel. By this mechanism, a passive colloid is able to spontaneously induce its own transport through an otherwise quiescent fluid.

Symbols and notation

Throughout this thesis we obey the following conventions. Rank-2 tensors and matrix quantities will be denoted by upright boldface symbols (e.g., the rotation matrix $\mathbf{R}$, and nematic order parameter $\mathbf{Q}$); vector quantities by italic boldface (e.g., position $\boldsymbol{r}$, and force $\boldsymbol{f}$); italic Roman or Greek script for all other physical quantities and constants (e.g., time t, and friction coefficient ζ).

Product operators are defined unambiguously by their counterparts in Einstein summation convention: $\boldsymbol{r}\boldsymbol{f} = r_i f_j$ denotes the tensor product of two vectors, $\boldsymbol{r} \cdot \boldsymbol{f} = r_i f_i$ denotes the scalar product, and $\mathbf{Q} : \mathbf{Q} = \mathrm{Tr}(\mathbf{Q}^T \mathbf{Q}) = Q_{ij} Q_{ij}$ denotes double contraction.

Publications

Authored publications contributing to this thesis

- Y. Gao, A.K. Balin, R.P.A. Dullens, J.M. Yeomans, D.G.A.L. Aarts; Thermal Analog of Gimbal Lock in a Colloidal Ferromagnetic Janus Rod, *Physical Review Letters*, **115**, 248301 (2015).
- A.K. Balin, A. Zöttl, J.M. Yeomans, T. Shendruk; Biopolymer dynamics driven by helical flagella, *Physical Review Fluids*, **2**, 113102 (2017).
- A.K. Balin, A. Doostmohammadi, J.M. Yeomans; Passive colloids induce active flow, *(In preparation)*.
- A.K. Balin, A. Zöttl, J.M. Yeomans, T. Shendruk; Polymer spooling by a swimming helix, *(In preparation)*.

Other contributions

- K.E. Klop, A. Zöttl, A.K. Balin, R.P.A. Dullens, J. M. Yeomans, D.G.A.L. Aarts; Orientational behaviour of silica rods in a Poiseuille flow, *(In preparation)*.
- A. Curran, Y. Liu, A.K. Balin, D.G.A.L. Aarts, R.P.A. Dullens; Driven Anisotropic Particle under Time-delayed Feedback Control, *(in preparation)*.

Contents

Appendices

1

Theory of Soft Matter

Understanding the crystalline structure of solids allowed physicists of the 20th century the ability to predict the macroscopic properties of a wide variety of materials. In many cases, the global behaviour of a crystal in response to an electric field or mechanical stress may be understood by the quantum mechanical interactions between neighbouring atoms in the lattice. The resulting field of *condensed matter physics* has been tremendously successful in uncovering the physics of crystalline solids, and has fuelled the information revolution from the invention of the semiconductor transistor in 1947 [1] to the more recent discovery of graphene [2].

However, there are many materials which do not yield to an analysis of this nature. In contrast to the 'hard' matter formed by crystals, these materials are often 'soft'; they can be flexible, fluid, granular or some combination of the these traits. Often, soft materials are governed by the behaviour of constituent particles much larger than the atom. For example, to understand foam or sand, it is not sufficient — or even that useful — to *only* understand the atoms they are composed of; instead their dynamics are dictated by an intermediate level of structure. In the case of foam, molecules organise to form bubbles, which in turn arrange to form the large-scale structure [3]. Sand, on the other hand, derives its properties from its granular composition; the atomic structure of the grains has little influence on its macroscopic properties. This intermediate level of structure in soft materials is normally termed the *mesoscopic* scale, and physics on this scale often results in the emergence of complex behaviour on the *macroscopic* scale [4].

For many decades, one of the largest fields of study within soft matter physics has been the physics of polymers, and the materials which they are used to make. This includes many everyday substances such as synthetic rubber and plastic, as well as a vast range of naturally occurring materials such as mucus and tree sap. Polymers also constitute many of the molecules required for life: DNA, RNA, proteins, and lipids [5]. The tight correspondence between biological *form* and *function* has been well documented, and so understanding the physics of polymer dynamics is a tremendously important endeavour, which has improved our knowledge of phenomena such as protein folding [6], viral self-assembly [7], and cell motility [8].

Biological soft matter is now understood to be fundamentally different from inert soft matter. In every living process, energy is constantly being converted from chemical energy into heat or mechanical work and therefore biological materials are constantly being driven out of equilibrium [9]. Moreover, this energy is injected throughout the bulk of the system, rather than just at the boundaries. This is fundamentally different to the type of nonequilibrium we might be familiar with: when we boil a kettle, we inject heat from the outside, however cells in our body constantly produce heat from within. This kind of bulk-driven soft matter is now termed *active matter* and there is currently a large community trying to understand its physics, which is thought to play a role in many complex processes observed in living systems including self-organisation, collective behaviour and pattern formation [9].

Despite the ubiquity of soft materials, the study of *soft condensed matter* is a relatively recent development in the natural sciences, with the first Nobel Prize in the field being awarded to Pierre-Gilles de Gennes in 1991 for his work on polymers and liquid crystals [10]. Active matter, specifically, is an even more recent subfield that grew rapidly in the early 2000s and is now a major branch of research [11].

Throughout this thesis we will be investigating the behaviour of mesoscale systems such as colloids, polymers, and biological microorganisms. At these length-scales, the fluid environment plays two crucial roles in determining the dynamics of such particles: (1) viscous drag counteracts external forces, and in the small-mass limit, inertial motion becomes negligible [12]; and (2) thermal fluctuations in the medium exert significant forces on the system, making its evolution stochastic and forcing us to treat its state in a statistical manner [13].

In this chapter we will discuss this phenomenology, developing first an understanding of viscous flow via the continuum Stokes' equations, and its extension to describing active fluids. Finally, we will introduce the basic concepts behind stochastic calculus with a view to building stochastic simulations of noisy systems. However, first we will present an overview of the thesis as a whole.

Overview

This thesis represents the culmination of work across various distinct projects in soft matter physics. Nevertheless, the thread that runs through the entire narrative is one of increasing complexity in parallel with a decrease in the dominance of thermal effects in favour of hydrodynamic effects.

In Chapter 2 we report on a rod-shaped ferromagnetic colloid in equilibrium. While many such rods, when packed tightly together, might form a soft granular fluid, we isolate a single particle to uncover some of the fundamental physics behind how it interacts with the thermal environment it is exposed to, and any strong magnetic and gravitational fields which it experiences. We find that a magnetic field compels the particle to randomly hop between two states of orientation and we discover that this hopping behaviour is mediated by a competition between entropic forces and potential forces. In Chapter 3 we look at what happens when we drive the rod out of equilibrium via a rotating magnetic field, providing a systematic theoretical description of the experimentally observed dynamics.

Chapters 4-6 represent an increase in complexity: we explore questions relating to how bacteria swim through biological fluids that contain polymers. Specifically, we study the interaction between a large polymer and a rotating helical filament that acts as a model for a bacterial flagellum. In Chapter 4 we develop this model system and describe the computational tools which we later use in Chapters 5 and 6 to simulate the interaction in the case of a pinned helix (a 'pump'), and a free helix (a 'swimmer'), respectively. The questions we ask include: What do the dynamics of a single polymer look like? What is the average behaviour of the polymers over many simulations? What does the energetics of the process look like? Does the polymer affect the swimming speed?

When many such swimming cells are concentrated together, they often collectively align and exhibit a type of flocking behaviour, similar to that seen in animals such as birds and fish. In Chapter 7 we look at how such *active fluids* behave when confined to a channel and observe the effects of including a passive colloidal particle in the system. We find that the inclusion of the colloid induces transition from a state characterised by zero flows in the system to one in which the fluid as a whole collectively begins flowing along one direction through the channel, transporting the colloid with it.

A note on contributions

As a result of the collaborative nature of the work involved, some data that are presented in this thesis were acquired by others. In Chapters 2 and 3, experiments and image analysis were conducted by Dr. Yongxiang Gao in the group of Prof. Dirk Aarts. However, all figures in Chapters 2 and 3 have been produced by the author even where experimental data have been used.

Chapter 5 describes a comparison between the author's simulations and multi-particle collision dynamics simulations conducted by Dr. Andreas Zöttl. In Fig. 5.1, we present analysis conducted by the author, which uses the data obtained by Dr. Zöttl.

1.1 Hydrodynamics of viscous media

1.1.1 The Stokes equations

The equations of motion for an incompressible Newtonian fluid are the Navier–Stokes equations [14]:

$$\rho\left(\partial_t + \boldsymbol{v}\cdot\boldsymbol{\nabla}\right)\boldsymbol{v} = \eta\nabla^2\boldsymbol{v} - \boldsymbol{\nabla}p + \boldsymbol{f} \tag{1.1}$$

$$\boldsymbol{\nabla}\cdot\boldsymbol{v} = \boldsymbol{0}. \tag{1.2}$$

The state of the fluid at any position and time is described by the velocity vector field $\boldsymbol{v}(\boldsymbol{r},t)$ — also termed the *flow field* — and pressure scalar field $p(\boldsymbol{r},t)$. The flow field evolves under the action of externally applied body forces represented by the quantity $\boldsymbol{f}(\boldsymbol{r},t)$. The two bulk properties which appear in Eqs. (1.1) are the mass density ρ and dynamic viscosity η.

In general, the full Navier–Stokes equations are hard to solve owing to the nonlinear and time-dependent nature of the left-hand-side of Eq. (1.1). However progress can be made by applying a nondimensionalisation using sensibly chosen velocity- and length-scales, v and L: $\boldsymbol{v}\to v\boldsymbol{v}^*$, $\boldsymbol{\nabla}\to\boldsymbol{\nabla}^*/L$, $p\to(\eta v/L)p^*$, $t\to(L/v)t^*$, and $\boldsymbol{f}\to(\eta v/L^2)\boldsymbol{f}^*$, and by defining the *Reynolds number*:

$$\mathrm{Re} = \frac{\rho v L}{\eta}. \tag{1.3}$$

For a given fluid-dynamical problem characterised by flow velocities on the order of v, and length-scales on the order of L, the Navier–Stokes equations become:

$$\mathrm{Re}\left(\partial_{t^*} + \boldsymbol{v}^*\cdot\boldsymbol{\nabla}^*\right)\boldsymbol{v}^* = \nabla^{*2}\boldsymbol{v}^* - \boldsymbol{\nabla}p^* + \boldsymbol{f}^*, \quad \boldsymbol{\nabla}^*\cdot\boldsymbol{v}^* = \boldsymbol{0}. \tag{1.4}$$

In this thesis we will solely consider microscopic systems in which the Reynolds number can be taken to be zero. The left-hand-side of Eqs. (1.4) therefore vanishes, and, by reintroducing the dimensional variables, produces the well known Stokes equations for viscous flow [12]:

$$\boldsymbol{\nabla}p - \eta\nabla^2\boldsymbol{v} = \boldsymbol{f}, \tag{1.5}$$

$$\boldsymbol{\nabla}\cdot\boldsymbol{v} = \boldsymbol{0}. \tag{1.6}$$

These equations describe how the pressure and velocity fields instantaneously respond to a force distribution in the fluid. Another dimensionless number that we will encounter in Chapters 4-6 when talking about polymers in rotational flow is the Deborah number: $\mathrm{De} = \tau_p \omega$, which is the ratio between the relaxation time of polymers in a solution τ_p, to a characteristic timescale of the flow $1/\omega$ — i.e., the period of the rotational flow.

1.1.2 Solving the Stokes equations

The Stokes equations simplify the Navier–Stokes equations in two key ways: (1) They are linear in both p and $\boldsymbol{v}$, so we may find solutions by the method of Green's functions [15]; and (2) They are time-independent, meaning that solutions for p and $\boldsymbol{v}$ are functions of the instantaneous distribution $\boldsymbol{f}$ only.

A point-force placed at the origin is given by the distribution $\boldsymbol{f}\delta(\boldsymbol{r})$, and the resulting solution can be found exactly [12]:

$$\boldsymbol{v}(\boldsymbol{r}) = \frac{\boldsymbol{f}}{8\pi\eta} \cdot \left(\frac{\mathbf{I}}{r} + \frac{\boldsymbol{r}\boldsymbol{r}}{r^3} \right), \; p(\boldsymbol{r}) = \frac{\boldsymbol{f} \cdot \boldsymbol{r}}{4\pi r^3}, \tag{1.7}$$

with $r = \sqrt{r_x^2 + r_y^2 + r_z^2}$. This point-force is known in this context as the *stokeslet*, and its corresponding velocity response is obtained by its contraction with the Green's function for the Stokes equations, which is known as the *Oseen tensor*:

$$\mathbf{G}(\boldsymbol{r}) = \frac{1}{8\pi\eta} \left(\frac{\mathbf{I}}{r} + \frac{\boldsymbol{r}\boldsymbol{r}}{r^3} \right). \tag{1.8}$$

Because of the linearity of Eqs. (1.5), we can sum its solutions to find the flow field due to any distribution of forces $\boldsymbol{f}(\boldsymbol{r})$:

$$\boldsymbol{v}(\boldsymbol{r}) = \int \mathrm{d}\boldsymbol{r}' \mathbf{G}(\boldsymbol{r} - \boldsymbol{r}') \boldsymbol{f}(\boldsymbol{r}'). \tag{1.9}$$

1.1.3 The multipole expansion

If we consider a localised distribution of forces in a fluid, we can study how $\boldsymbol{v}(\boldsymbol{r})$ behaves far away by Taylor expanding Eq. (1.9):

$$\begin{aligned} u_i(\boldsymbol{r}) &= \int \left[\mathrm{G}_{ij}(\boldsymbol{r}) - r'_k \mathrm{G}_{ij,k}(\boldsymbol{r}) + \frac{1}{2} r'_k r'_l \mathrm{G}_{ij,kl}(\boldsymbol{r}) - ... \right] f_j(\boldsymbol{r}')\mathrm{d}\boldsymbol{r}' \\ &= \mathrm{G}_{ij}(\boldsymbol{r}) \int f_j(\boldsymbol{r}')\mathrm{d}\boldsymbol{r}' - \mathrm{G}_{ij,k}(\boldsymbol{r}) \int r'_k f_j \mathrm{d}\boldsymbol{r}' + \frac{1}{2}\mathrm{G}_{ij,kl}(\boldsymbol{r}) \int r'_k r'_l f_j \mathrm{d}\boldsymbol{r}' - ... \\ &= \mathrm{G}_{ij}(\boldsymbol{r}) F_j + \mathrm{G}_{ij,k}(\boldsymbol{r}) D_{jk} + \frac{1}{2}\mathrm{G}_{ij,kl}(\boldsymbol{r}) Q_{jkl} - .... \end{aligned} \tag{1.10}$$

where we have used Einstein's index convention to sum over repeated indices and $\mathrm{G}_{ij,k}$ and $\mathrm{G}_{ij,kl}$ are the first and second tensor derivatives of the Oseen tensor respectively. This is called the *multipole expansion* by analogy to electrodynamics [12]. It allows us to decompose the far-field velocities due to a complicated force distribution in terms of its lowest order contributions. We can see that the first term has the same structure as the stokeslet[1] in Eq. (1.7), and so we identify $\boldsymbol{F}$ as the net force on the fluid, $\int \boldsymbol{f}(\boldsymbol{r}')\mathrm{d}\boldsymbol{r}'$.

The next term in the equation is the *dipole*, whose strength is given by the first moment of the force distribution, $\mathbf{D} = -\int \boldsymbol{r}'\boldsymbol{f}\mathrm{d}\boldsymbol{r}'$. We can further decompose this into a traceless tensor with a symmetric and antisymmetric part:

$$\mathbf{D} - \frac{1}{3}\mathrm{Tr}\ \mathbf{D} = \mathbf{S} + \mathbf{T}. \tag{1.11}$$

The symmetric part is referred to as the *stresslet*, and can be thought of as resulting from a pair of colinear equal and opposite forces near each other. Depending on the sign of the dipole, the resulting field is either extensile (⟵⟶), or contractile (⟶⟵). The antisymmetric part, termed the *rotlet*, results from a distribution of forces that impart a net torque on the fluid; in the most basic case it is due to a pair of equal and opposite noncolinear forces (↑↓).

Higher order terms such as the quadrupole Q_{ijk} result from higher order moments of the force distribution, and can become dominant in the near-field. By

---

[1] Sometimes the term *stokeslet* is used to refer to the flow field created by a point-force, as well as the point-force itself. Here, we use the term interchangeably to mean either the force or the field — and similarly for the related terms *rotlet*, *dipole*, *quadrupole* etc.

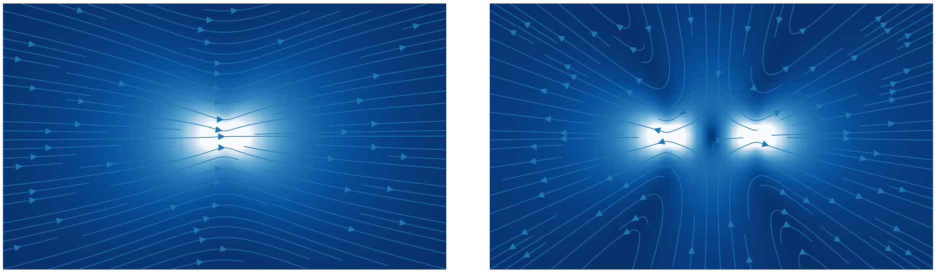

(a) Stokeslet (→)

(b) Dipole (←→)

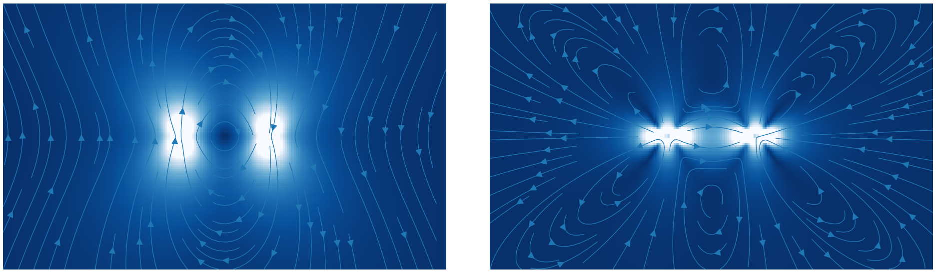

(c) Rotlet (↑ ↓)

(d) Quadrupole (←→ →←)

Figure 1.1: Flow fields due to different distributions of forces corresponding to the lowest order terms in the multipole expansion.

approximating an immersed body (such as a colloid or swimmer) as a distribution of forces, we can often understand a lot about the response of a fluid to their dynamics. The flow fields generated by some of these force distributions are shown in Fig. 1.1.

1.2 Locomotion in viscous media

1.2.1 Biophysical overview

Motility in microorganisms

The ability for organisms to generate motion in response to their environment is one of the defining features of life, and is in general termed *motility*. In the macroscopic world, we take this ability for granted as we have evolved a central nervous system that can command the actuation of limbs that have especially evolved to execute our will or instinct to move. The fact that even unicellular organisms have evolved a similar ability to sense and respond to their environment through motion, and use this ability to perform complex tasks and functions is therefore astounding.

By way of example, mammalian sperm cells periodically beat long protruding filaments called axonemes, which are composed of bundles of flexible, tube-like proteins. Upon their deposition in the anterior vagina, they propel themselves away from the acidic exogenous environment and into the cervical canal, where a lining of mucus acts as a filter for cells with inadequate motility [16]. Later, they utilise thermotaxis and chemotaxis (thermal and chemical sensing) to seek out a single cell in the Fallopian tube: the female oocyte. In order to penetrate the egg cell, they enter into a mode of hyperactivation, in which their swimming beat changes in such a way as to increase the force they can apply and break through the oocyte cell wall [17]. The journey of the spermatozoon highlights many of the various challenges that are faced by all swimming microorganisms. However, evolution has produced a number of different swimming mechanisms, and so problems like swimming through mucus and navigating chemical gradients are solved in different ways by different organisms.

Bacteria often inhabit host organisms, either as pathogens or as symbiotes [18]. In the former case, bacterial motility is thought to strongly enhance their infectious virulence [19]. For example, *Helicobacter pylori* (*H. pylori*) require motility in order to burrow into the mucus lining of the stomach, where they can often cause gastritis or stomach ulcers [20]. Although in a lot of cases, infections are characterised by the formation of biofilms in which bacteria become immobile and adhere to one another in a polymeric matrix, it has been suggested that subpopulations of motile bacteria burrow through the biofilm providing ‘irrigation channels’ which increase the nutrient uptake within the greater population [21]. It is the observations of such phenomena that beg for a better understanding of the physics of cell motility in biologically realistic environments.

Model organisms

Broadly speaking, cells swim via one of two categories of mechanisms: flagella or cilia. Flagella are long appendages which gather at one end of the cell and beat or rotate periodically generating thrust. Cilia, on the other hand, are often shorter, and distributed evenly across the surface of the cell. Their asymmetrical beating pattern — consisting of a power stroke and recovery stroke — generates fluid flow across the cell's body [8]. In this thesis we will concentrate primarily on swimmers driven by rotating flagella.

The most widely studied swimming bacteria are *Escherichia coli* (*E. coli*) which occur naturally in the intestinal tract of mammals, and some strains of which are known to cause infections [22]. They swim using a number of helical flagella which are each driven by a bacterial flagellar motor: a large protein complex that produces a torque on the flagellum powered by a proton gradient across the cell membrane [23]. The helical shape of the flagellum means that as it is rotated it acts like a corkscrew, pushing the cell through the fluid. When the motors are all rotating anticlockwise, the filaments bundle together and operate cooperatively. However, when one or more of the motors switch to clockwise rotation, the cooperation between the flagella breaks down, and thrust ceases [24]. This causes the cell to reorient its direction randomly, and when anticlockwise rotation starts again, the cell continues swimming, but in a different direction.

As the motors periodically switch between anticlockwise and clockwise rotation, the resulting type of swimming is known as *run-and-tumble* motion, in which the cell's trajectory is composed of straight 'run' segments interrupted by 'tumble' events [25]. Importantly the tumbling events occur randomly with a rate that is dependent on the chemical surroundings of the cell. This chemistry-dependent tumbling rate leads to *chemotaxis*, which is the ability for the bacteria to swim along chemical gradients.

Though *E. coli* are often used as a model organism due to a wide variety of strains that have been cultivated over the years for *in vitro* experimentation, *Salmonella typhimurium* also utilise multiple helical flagella to achieve locomotion [8]. Thus, helically driven cells constitute a widely studied class of swimming microorganisms.

Artificial microswimmers

Studying the physics of swimming sperm and bacteria has medical applications to fertility and infection, however it is also worth noting that the emerging fields of micro- and nanorobotics often draw direct inspiration from biology. Taking a biomimetic approach, a number of artificial magnetic microswimmers have been developed whose motion is actuated by the influence of external fields [26]. For example, inspired by the rotating flagella of microbes, helical magnetic ribbons have been observed to swim under the influence of a rotating magnetic field [27]. Another broad class of artificial swimmers are active ‘Janus’ colloids — so-named after the two-faced god of the Roman pantheon — which are composed of complementary hemispheres with different surface chemistry that creates a net unidirectional flow across their surface [28].

From a *biological* view point, while the first resembles more closely the swimming strategy of a flagellated microbe, the second class better approximates the behaviour of a ciliated microorganism. However, as we shall see in the next section, an arguably more fundamental *physical* difference is due to the effect that an externally applied force or torque (such as that applied by the magnetic field) has on the fluid flow far away from the particle.

1.2.2 Far-field hydrodynamics

The Scallop Theorem

Underpinning the modern theoretical work on microbe hydrodynamics is a principle known as *The Scallop Theorem*, which was outlined in a lecture by E.M. Purcell (1977) titled *Life at Low Reynolds Number* [29]. First, it is useful to consider what is meant by ‘low Reynolds Number’ when discussing the world inhabited by microorganisms.

We saw in Sec. 1.1.1 that the Reynolds number is a nondimensional number given by $\mathrm{Re} = \rho v L/\eta$, which characterises the magnitude of inertial forces in a fluid to viscous forces. For an *E. coli* that has a characteristic length $L \approx 2\,\mu\mathrm{m}$ and swimming velocity $v \approx 30\,\mu\mathrm{m\,s^{-1}}$ in water (which has a density $\rho \approx 10^3\,\mathrm{kg\,m^{-3}}$, and viscosity $\eta \approx 10^{-3}\,\mathrm{kg\,s^{-1}\,m^{-1}}$), the Reynolds number is roughly 6×10^{-5}. For all intents and purposes, we can consider microbes swimming in a world where $\mathrm{Re} = 0$, and hence all inertia disappears. Such a world is described by the Stokes equations, Eqs. (1.5), which we have already seen are amenable to solution via Green's method.

One important property of the Stokes equations is that they are time-independent. While high Reynolds number flows carry inertia and therefore take time to dissipate when the forces $\boldsymbol{f}$ disappear, at low Reynolds number, flow fields are instantaneous solutions of the forces at any given time. This means that only the sequence of motions that a swimmer performs governs its motion, and not how fast it performs them. If the swimming stroke is *reciprocal*, meaning that the reverse sequence is identical to the forward sequence, then no swimming can be achieved. This is known as the *Scallop Theorem*, as scallops, which swim at high Reynolds number by the reciprocal opening and closing of a single hinge, would be prohibited from swimming in the microscopic world [29].

The swimming techniques mentioned in the previous section all break reciprocity: the power stroke and recovery stroke of cilia are asymmetric; sperm send travelling waves along their flagella; and helical flagella are chiral, which means that continuous rotation breaks time-reversal symmetry.

Dipolar flow fields

With an understanding of how cells achieve motion, the next step is to understand the kind of fluid flow they create as they swim. Let us consider a flagellated bacterium such as an *E. coli* cell. Recall that in Sec. 1.1.3 we described how the fluid flow around a moving body could be approximated by considering the distribution of forces it exerts on the fluid. It is tempting to think that far away from the swimming cell, the thrust imparted by flagellum my be coarsely approximated as a point force acting on the fluid. This would lead us to conclude that only the stokeslet term in the multipole expansion survives, and therefore, by Eq. (1.7), the flow decays as $|\boldsymbol{v}| \sim 1/r$. However, this is not the case. Swimmers, by their very nature, must be force- and torque-free as they are *self*-motile, and rely on no external forces or torques to generate motion. Hence the leading order term in the multipole expansion of any swimmer must be dipolar, producing a flow field similar to the one shown in Fig. 1.1(b).

Just as the flagellum of the cell imparts a backwards thrust on the fluid, the cell body (or 'head') must impart an equal and opposite force on the fluid. Far away from the swimmer, the fluid experiences these two forces as an extensile force-dipole (←→). There are also types of cells whose swimming may be approximated by a contractile force-dipole (→←) such as the alga *Chlamydomonas reinhardtii*, which has two flagella on its front that pull the cell forwards on each stroke. The former type of cells are called *pushers*, while the latter type are called *pullers*. The far-field flow created by a puller has the same structure as that of a pusher, shown in Fig. 1.1(b), except with the direction of the streamlines reversed.

Returning to the *E. coli*, as we consider flow in regions nearer and nearer the cell, we must take into account higher order terms in the multipole expanison. Spagnolie and Lauga (2012) provide a decomposition of the flow field due to different parts of the cell anatomy [30]. As the bacterial flagellar motor generates a torque, an equal and opposite torque must be applied to the flagellum and cell body, hence to counteract the fast rotation of the flagellum, the body counter-rotates slowly. The result of this on the fluid is the generation of two equal and opposite rotlet fields which add to a rotlet-dipole. A force-quadrupolar field becomes important nearer the swimmer as a weak offset force-dipole corrects for the shape asymmetry between the head and flagellum, and the finite size of the head itself must be corrected for by a source-dipole.

The same is not true in the case of artificial swimmers that are actuated by external fields. For example, the magnetic ribbons discussed in Sec. 1.2.1 are rotated by external fields and hence apply a net torque on the fluid. Their flow-field therefore has the signature of a rotlet, rather than a rotlet-dipole created by a torque-free motile cell.

Studying far-field flows such as these is theoretically important for understanding the interactions between swimmers and geometrical boundaries [30, 31], synchronisation between beating filaments [32, 33], and swimmer–swimmer interactions that give rise to collective behaviour [34, 35]. However such analysis can tell us nothing about the details of *how* cells swim — for example, how the geometry of the flagellum affects swimming speed or efficiency. For this we must model their specific geometry, and find ways to solve for the hydrodynamics of their motion. This has been done for flagella using *slender body theory* [8], in which a filament element locally has an anisotropic drag due to its elongation along its central contour $\boldsymbol{r}(s)$, and experiences hydrodynamic interactions with the rest of the filament — found by integrating $\int \mathbf{G}[\boldsymbol{r} - \boldsymbol{r}(s)] \cdot \boldsymbol{f}(s) \mathrm{d}s$, excluding a region within a cutoff distance δ of $\boldsymbol{r}$.

1.3 Hydrodynamics of active matter

From active particles to active matter

So far we have been thinking about individual active *particles*; that is, particles which internally convert stored or ambient chemical energy into mechanical work. When many such particles interact with one another, *collective behaviour* often emerges. On the macroscopic scale, we are familiar with many species which self-organise into flocks, herds, or schools in order to evade predators, migrate as groups, or collectively conserve energy [36]. The dynamics of such flocks are are often governed in a decentralised manner and simple individual-based models have successfully demonstrated that global flocking can emerge as a result of local alignment interactions between nearby agents [37, 38]. As a result, observers of such flocks will tend to notice spontaneous flows and density waves as if the flock itself was a fluid-like medium [39, 40].

Despite the fundamentally different physics of the microscopic world, similar collective behaviours are observed across a wide range of active particles including bundles of microtubules driven by dynein molecular motors [41], dense suspensions of flagellated bacteria such as *B. subtilis* [42], and externally driven swimming colloids [43]. These systems all exhibit fluid-like behaviour including vortices, turbulence and coherent flow [44].

The nematic interaction

Our goal is to understand these seemingly universal features of active matter within the framework of hydrodynamics. We have already seen in Sec. 1.1.1 how the continuum velocity field of a viscous Newtonian fluid can be described by the Stokes Equations, and we wish to extend this description to active matter. However, active fluids differ from Newtonian fluids in two major ways: (1) Due in part to the rod-like shape of most active particles, as well as their tendency to swim along a defined axis, interactions between particles often favour local alignment; and (2) their activity means that energy is constantly injected into the system from within the bulk rather than just at the boundaries.

As a result of (1), particles tend to locally align along a position-dependent axis called the *director*: $\hat{\boldsymbol{n}}(\boldsymbol{r})$. If the interaction does not favour polarity, this type of interaction is called *nematic* alignment. We can take a mean-field approach in defining the nematic order parameter for this system,

$$\mathbf{Q} = q\left(\hat{\boldsymbol{n}}\hat{\boldsymbol{n}} - \frac{1}{3}\mathbf{I}\right), \tag{1.12}$$

which has a magnitude q. This tensor is symmetric and traceless by construction and is invariant under the transformation $\hat{\boldsymbol{n}} \to -\hat{\boldsymbol{n}}$. This order parameter must be incorporated into the equations of motion for the active fluid in order to capture its full dynamics.

Due to (2) we must incorporate bulk energy production into our hydrodynamic equations; this can be done by defining an active stress $\mathbf{\Pi}_a$ to reflect the fact that the constituent particles create dipolar stresslet fields.

Nematohydrodynamics

Beris and Edwards (1994) give the hydrodynamic equations for the flow field and nematic order parameter [45]:

$$\begin{aligned} \boldsymbol{\nabla} \cdot \boldsymbol{v} &= 0, && (1.13) \\ \rho\left(\partial_t + \boldsymbol{v} \cdot \boldsymbol{\nabla}\right)\boldsymbol{v} &= \boldsymbol{\nabla} \cdot \mathbf{\Pi}, && (1.14) \\ \left(\partial_t + \boldsymbol{v} \cdot \boldsymbol{\nabla}\right)\mathbf{Q} &= \mathbf{S} + \Gamma\mathbf{H}. && (1.15) \end{aligned}$$

These equations are explicitly parameterised by the fluid density, ρ, and the rotational diffusion coefficient for the particles Γ.

The dynamical equations for $\boldsymbol{v}$ and $\mathbf{Q}$ depend on the stress $\boldsymbol{\Pi}$, a generalised advection term $\mathbf{S}$, and the molecular field $\mathbf{H}$. The molecular field describes the relaxation of the orientational order towards the minimum of the free energy: $\mathbf{H} = -\frac{\delta \mathcal{F}}{\delta \mathbf{Q}} + \frac{1}{3}\mathrm{Tr}\left(\frac{\delta \mathcal{F}}{\delta \mathbf{Q}}\right)\mathbf{I}$. The free energy of the nematic phase is given by the Landau–de Gennes bulk free energy plus an elastic bend–splay term:

$$\mathcal{F} = \left(1 - \frac{\gamma}{3}\right)\mathrm{Tr}(\mathbf{Q}^2) + \frac{\gamma}{3}\mathrm{Tr}(\mathbf{Q}^3) + \frac{\gamma}{4}\mathrm{Tr}(\mathbf{Q}^2)^2 + \kappa \mathrm{Tr}[(\boldsymbol{\nabla}\mathbf{Q})^2], \tag{1.16}$$

where κ is the elastic constant, and the isotropic–nematic transition parameter γ effectively controls the temperature of the nematic phase. At high temperature ($\gamma < 3$), $\mathbf{Q} = \mathbf{0}$ minimises the free energy, and the fluid becomes isotropic. We will only be concerned with $\gamma > 3$ (strictly) to ensure the system is in the nematic phase.

The advection term arises due to the response of the nematic particles to velocity gradients arising from fluid strain $\mathbf{E}$ and vorticity $\boldsymbol{\Omega}$:

$$\mathbf{S} = (\xi\mathbf{E} + \boldsymbol{\Omega})\mathbf{Q}' + \mathbf{Q}'(\xi\mathbf{E} - \boldsymbol{\Omega}) - 2\xi\mathbf{Q}'\mathrm{Tr}[\mathbf{Q}(\boldsymbol{\nabla}\boldsymbol{v})^T], \tag{1.17}$$

$$\mathbf{E} = \frac{1}{2}\left[\boldsymbol{\nabla}\boldsymbol{v} + (\boldsymbol{\nabla}\boldsymbol{v})^T\right], \quad \boldsymbol{\Omega} = \frac{1}{2}\left[(\boldsymbol{\nabla}\boldsymbol{v})^T - \boldsymbol{\nabla}\boldsymbol{v}\right], \tag{1.18}$$

where $\mathbf{Q}' = \mathbf{Q} + \mathbf{I}/3$. The tumbling parameter ξ describes how the nematic particles respond to external velocity gradients. The response will either be dominated by strain for large ξ (flow-aligning regime) or by vorticity for low ξ (tumbling regime).

The stress tensor comprises three components, $\boldsymbol{\Pi} = \boldsymbol{\Pi}_{\mathrm{v}} + \boldsymbol{\Pi}_{\mathrm{e}} + \boldsymbol{\Pi}_{\mathrm{a}}$, which measure contributions from the viscous, elastic and active stresses respectively. The viscous stress is familiar from the Navier–Stokes equations:

$$\boldsymbol{\Pi}_{\mathrm{v}} = 2\eta\mathbf{E}, \tag{1.19}$$

and the elastic stress is

$$\boldsymbol{\Pi}_{\mathrm{e}} = -p\mathbf{I} + 2\xi\left(\mathbf{Q} + \frac{1}{3}\mathbf{I}\right)\mathrm{Tr}[\mathbf{QH}] - \xi\mathbf{H}\left(\mathbf{Q} + \frac{1}{3}\mathbf{I}\right) \tag{1.20}$$

$$-\xi\left(\mathbf{Q} + \frac{1}{3}\mathbf{I}\right)\mathbf{H} - \boldsymbol{\nabla}\mathbf{Q} : \frac{\delta\mathcal{F}}{\delta(\boldsymbol{\nabla}\mathbf{Q})} + \mathbf{QH} - \mathbf{HQ}. \tag{1.21}$$

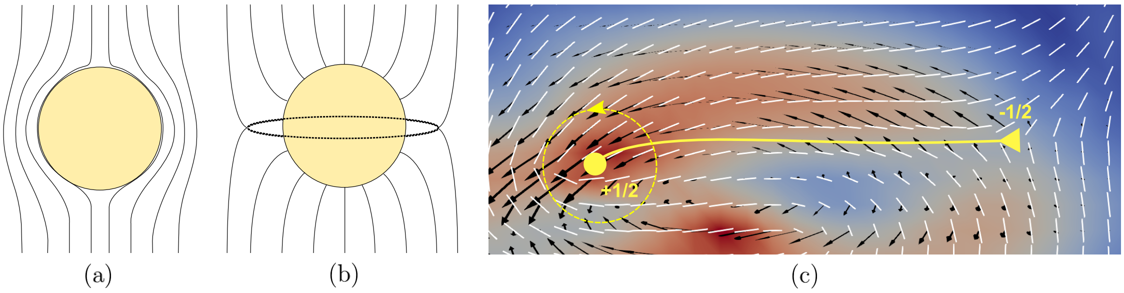

Figure 1.2: (a) 'Boojum' defect caused by inclusion of a colloid with planar anchoring conditions, and (b) 'Saturn ring' defect caused by inclusion of a colloid with normal anchoring conditions. (c) Extensile active nematic fluid with a $+1/2$ defect moving away from a $-1/2$ defect. Flow strength $|\boldsymbol{v}|$ is shown on the heatmap (a.u.), flow strength and direction by the arrows, and nematic director field $\hat{\boldsymbol{n}}$ by the white lines. Snapshot taken from a simulation from Chapter 7.

Because the active particles can be assumed to be dipolar, we can model the particles as contributing stresslets aligned with the local director. This gives rise to an active stress: $\mathbf{\Pi}_{\mathrm{a}} = -\zeta \mathbf{Q}$, where the activity parameter is $\zeta > 0$ for extensile fluids (comprised of pushers), and $\zeta < 0$ for contractile fluids (comprised of pullers).

In Chapter 7 we will make use of a hybrid lattice-Boltzmann method to solve these equations, with appropriate boundary conditions, for an active nematic confined to a channel.

Topological defects

It is rarely possibly to satisfy Eqs. (1.13) with a smoothly varying director $\hat{\boldsymbol{n}}$, because boundary conditions imposed by the inclusion of colloids, or the topology of the domain are often incompatible [46]. A simple example of this is occurs when we consider a sphere which imposes planar anchoring of the nematic director field near its exterior surface. Because any vector field on the surface of a sphere must have at least two discontinuities [47], it is impossible to satisfy this boundary condition everywhere: there will be two locations where the director is undefined [48]. In the case of a uniform ambient director, these two defects appear on antipodal points of the sphere as shown in Fig. 1.2(a). In the case of a sphere with normal anchoring, this can be satisfied across the surface of the sphere, but at some radius away the ambient homogeneous director will dominate over the surface-induced isotropic director and a ‘saturn ring’ defect will form as shown in Fig. 1.2(b).

Point defects are also possible. These are defined in 2-dimensions as points around which there is a net winding of the director $\hat{\boldsymbol{n}}$. Because of the nonorientability of $\hat{\boldsymbol{n}}$, nematic liquid crystals are able to host half-integer charge defects as shown in Fig. 1.2(c). They can be created or annihilated in pairs, or be removed from the system at the boundary (as long as the boundary does not impose too strong an anchoring condition) [49]. In active liquid crystals, $+1/2$ defects are known to be motile due to the unbalanced elastic and active stresses they impart on the fluid, while $-1/2$ defects are not [50, 51].

1.4 Stochastic calculus

1.4.1 Brownian motion and the Langevin equation

The Langevin equation gives the simplest phenomenological description of the motion of a particle subject to thermal fluctuations [52]. In 3-dimensions, the spatial trajectory $\boldsymbol{r}(t)$ of a spherical particle of mass m and radius a is found by equating its acceleration to the various forces acting on it and solving the resulting equation. For a particle that experiences viscous drag of strength $\lambda = 6\pi\eta a$, deterministic external forces $\boldsymbol{f}(\boldsymbol{r}, t)$, and fluctuating thermal forces $\boldsymbol{\xi}(t)$, this equation is:

$$m\frac{\mathrm{d}^2\boldsymbol{r}}{\mathrm{d}t^2} = -\lambda\frac{\mathrm{d}\boldsymbol{r}}{\mathrm{d}t} + \boldsymbol{f}(\boldsymbol{r}, t) + \boldsymbol{\xi}(t). \tag{1.22}$$

We seek a model for the noise that must have certain properties. Firstly, it must be fluctuating on timescales much faster than those of observation. In reality — barring quantum effects — the forces that act on the particle might deterministically obey the dynamics governed by a many-particle Hamiltonian that captures all the intermolecular forces in the medium. However, we assume that enough time passes between observations of the system that the forces we measure are statistically independent from one another. If the medium is in thermal equilibrium, we also expect these forces to be normally distributed with mean of zero and a variance related to the temperature of the medium.

A good model for $\boldsymbol{\xi}(t)$ that satisfies these criteria is *white noise*, which is statistically unbiased ($\langle\boldsymbol{\xi}(t)\rangle = 0$) and uncorrelated ($\langle\boldsymbol{\xi}(t)\boldsymbol{\xi}(t')\rangle = 2D\mathbf{I}\delta(t-t')$). D is the diffusion coefficient of the particle, which is related to the drag λ by the Einstein–Smoluchowski relation, $D = k_{\mathrm{B}}T/\lambda$ [53]. This is a specific example of a fluctuation–dissipation relation.

For the remainder of this work we will be working in the limit $m \to 0$, i.e., the *overdamped* regime. This limit of Eq. (1.22), along with the statistical properties of the noise, allow us to write the overdamped Langevin equation for the particle:

$$\begin{aligned} \frac{\mathrm{d}\boldsymbol{r}}{\mathrm{d}t} &= \mu\boldsymbol{f}(\boldsymbol{r},t) + b\,\boldsymbol{\zeta}(t), && (1.23)\\ \langle\boldsymbol{\zeta}(t)\rangle &= 0, && (1.24)\\ \langle\boldsymbol{\zeta}(t)\boldsymbol{\zeta}(t')\rangle &= \mathbf{I}\delta(t-t'), && (1.25) \end{aligned}$$

where the mobility $\mu = 1/\lambda$ is the viscous response of the particle to an applied force, and the Einstein–Smoluchowski relation is encapsulated in $b = \sqrt{2k_{\mathrm{B}}T/\mu}$.

When there is no external force present, these equations must reduce to simple Brownian motion, which is well known to be described by the Wiener process $\boldsymbol{w}(t)$, which has a number of properties [54]: (1) $\boldsymbol{w}(t)$ is a continuous function of time; (2) it is wildly fluctuating and nowhere differentiable; (3) it is unbiased: $\langle\boldsymbol{w}(t)\rangle = \boldsymbol{w}(0) := \mathbf{0}$; (4) its mean-square grows with time: $\langle\boldsymbol{w}(t)^2\rangle = t$; (5) its increments $\Delta\boldsymbol{w}_i = \boldsymbol{w}(t_i) - \boldsymbol{w}(s_i)$ over nonoverlapping intervals of time $[s_i, t_i]$ are independent. Properties (3) and (4) apply equally well to the increments $\Delta\boldsymbol{w}$: (3) $\langle\Delta\boldsymbol{w}\rangle = \mathbf{0}$, and (4) $\langle\Delta\boldsymbol{w}(t)^2\rangle = \Delta t$, and this remains true in the limit $\Delta t \to \mathrm{d}t$, and $\Delta\boldsymbol{w} \to \mathrm{d}\boldsymbol{w}$.

Equation (1.23) appears to suggest that the white noise is the derivative of the Wiener process: $\mathrm{d}\boldsymbol{w}/\mathrm{d}t = \boldsymbol{\zeta}(t)$, however property (2) precludes us from being able to write this explicitly as it results in the Langevin equation becoming ill-defined. Instead, we may make the heuristic identification that $\mathrm{d}\boldsymbol{w} = \boldsymbol{\zeta}(t)\mathrm{d}t$, which allows us to recast the Langevin equation as a stochastic differential equation (SDE):

$$\mathrm{d}\boldsymbol{r} = \mu\boldsymbol{f}\ \mathrm{d}t + b\ \mathrm{d}\boldsymbol{w}, \tag{1.26}$$

with a corresponding fluctuation–dissipation relation $b^2 = 2k_\mathrm{B}T\mu$. This means that, given a realisation of a Wiener process $\boldsymbol{w}(t)$, we can integrate (1.26) to find the trajectory,

$$\boldsymbol{r}(t) - \boldsymbol{r}(0) = \int_0^t \mu\boldsymbol{f}(t)\ \mathrm{d}t + \int b\ \mathrm{d}\boldsymbol{w}, \tag{1.27}$$

as long as we can define the integral $\int b\ \mathrm{d}\boldsymbol{w}$. Let us assume that $\boldsymbol{f}(t) = \mathbf{0}$, so that we are dealing with Brownian motion. To define the integral, we apply the same procedure as we do with standard calculus, and partition the time in Eq. (1.27) into discrete periods, $[t_1, t_2, ...t_n]$, where a subscript i on a variable denotes evaluation at the corresponding time, e.g., $\boldsymbol{f}_i = \boldsymbol{f}(t_i)$. We can then construct the trajectory (with $\boldsymbol{r}_0 = \mathbf{0}$) as the sum of noise increments,

$$\boldsymbol{r}_n = \sum_{i=0}^{n} b[\boldsymbol{w}_{i+1} - \boldsymbol{w}_i]. \tag{1.28}$$

We can ask whether this discretisation ensures that $\boldsymbol{r}_n$ behaves in the way we expect $\boldsymbol{r}(t)$ to behave. We see that the mean final displacement is zero ($\langle \boldsymbol{r}_n \rangle = \mathbf{0}$) by noting that property (3) tells us that $\langle \Delta\boldsymbol{w} \rangle = \mathbf{0}$. We can also compute the second moment:

$$\begin{aligned} \langle \boldsymbol{r}_n^2 \rangle &= b^2 \sum_{j=1}^{n}\sum_{i=1}^{n} \langle [\boldsymbol{w}_{i+1} - \boldsymbol{w}_i] \cdot [\boldsymbol{w}_{j+1} - \boldsymbol{w}_j] \rangle && (1.29) \\ &= b^2 \sum_{i=1}^{n} \langle [\boldsymbol{w}_{i+1} - \boldsymbol{w}_i]^2 \rangle && (1.30) \\ &= b^2 t_n && (1.31) \end{aligned}$$

where in the 2nd line we have used the property (5) that nonoverlapping increments $\Delta\boldsymbol{w}$ are independent, and in the 3rd line we have used property (4). This shows that the discretisation Eq. (1.28) produces the correct statistical properties for $\boldsymbol{r}_n$ to be a good model for $\boldsymbol{r}(t)$, and gives us the required tools for solving the most basic Langevin equation: $\lambda\dot{\boldsymbol{r}} = \boldsymbol{\xi}(t)$.

1.4.2 Langevin equation with anisotropic mobility

We have just discussed the special case of isotropic translational diffusion, in which the particle responds equally to forces in all directions. However, there are situations where the diffusion or response to forces are anisotropic. This could be perhaps due to a nearby wall or obstacle that makes motion along certain axes 'easier' or 'harder', which in turn affects the strength of the noise experienced by the particle in those directions. Alternatively, we might think of $\boldsymbol{r}$ not as a 3-dimensional vector corresponding to the position of a particle, but a $3N$-dimensional vector describing the positions of a collection of N particles immersed in the medium. Hydrodynamic interactions between these particles would then make the force–response relationship anisotropic as well as coupling the noise experienced by one particle to that experienced by a distant particle.

These considerations force us to consider a more general case of the Langevin SDE in Eq. (1.26) in which the mobility and noise strength are *tensors* $\boldsymbol{\mu}(\boldsymbol{r}_t)$, and $\mathbf{b}(\boldsymbol{r}_t)$ that in general might depend on the position(s) $\boldsymbol{r}(t)$. For notational convenience we write $\mathbf{b} = \mathbf{b}(\boldsymbol{r}_t)$, and $\boldsymbol{\mu} = \boldsymbol{\mu}(\boldsymbol{r}_t)$. The general Langevin SDE is:

$$\begin{aligned} \mathrm{d}\boldsymbol{r} &= \boldsymbol{\mu}\boldsymbol{f}\,\mathrm{d}t + \mathbf{b}\,\mathrm{d}\boldsymbol{w}, && (1.32) \\ \langle \mathbf{b}^T\mathbf{b} \rangle &= 2k_{\mathrm{B}}T\boldsymbol{\mu}\,\delta(t-t'), && (1.33) \end{aligned}$$

where the fluctuation–dissipation relation has taken the form of an ensemble-averaged tensor equation. However, this creates a problem of interpreting the integral $\int \mathbf{b}\,\mathrm{d}\boldsymbol{w}$. When we attempt to discretise it in the same way that we did in Eq. (1.28), we are given a choice of where in the time interval $[t_i, t_{i+1}]$ to evaluate $\mathbf{b}(\boldsymbol{r}_t)$:

$$\boldsymbol{r}_n = \sum_{i=0}^{n} \mathbf{b}(\boldsymbol{r}_s)[\boldsymbol{w}_{i+1} - \boldsymbol{w}_i], \qquad \text{for } s \in [t_i, t_{i+1}]. \tag{1.34}$$

Under the normal rules of calculus, such a choice does not matter in the limit $\Delta t \to 0$, but in stochastic calculus it does [54]. As a result, the following two interpretations of the stochastic integral have emerged:

$$\begin{aligned} \text{Itô:} \quad & \int \mathbf{b}(\boldsymbol{r})\,\mathrm{d}\boldsymbol{w} && \Longrightarrow \sum_{i=0}^{n} \mathbf{b}(\boldsymbol{r}_{t_i})[\boldsymbol{w}_{i+1} - \boldsymbol{w}_i], && (1.35) \\ \text{Stratonovich:} \quad & \int \mathbf{b}(\boldsymbol{r}) \circ \mathrm{d}\boldsymbol{w} && \Longrightarrow \sum_{i=0}^{n} \frac{1}{2}[\mathbf{b}(\boldsymbol{r}_{t_i}) + \mathbf{b}(\boldsymbol{r}_{t_{i+1}})][\boldsymbol{w}_{i+1} - \boldsymbol{w}_i]. && (1.36) \end{aligned}$$

While Itô calculus is the preferred choice for truly stochastic processes due to the 'nonanticipating' nature of its evaluation, the preferred choice for modelling physical phenomena turns out to be the Stratonovich approach [55]. More recently, it has been shown that noisy electric circuits with feedback can be tuned to obey either Stratonovich or Itô calculus [56]. However, any interpretation other than the Itô one appears to pose a problem, as the calculation of $\boldsymbol{r}_{t_{i+1}}$ contains itself. However it can be shown that, by a suitable transformation, a Stratonovich SDE may be turned into an Itô SDE that contains an extra 'drift' term [54]:

$$\begin{aligned} \mathrm{d}\boldsymbol{r} &= \left[\boldsymbol{\mu}\boldsymbol{f} + \frac{1}{2}\mathbf{b}^T\boldsymbol{\nabla}\cdot\mathbf{b}\right]\mathrm{d}t + \mathbf{b}\ \mathrm{d}\boldsymbol{w}, && (1.37)\\ \langle\mathbf{b}^T\mathbf{b}\rangle &= 2k_{\mathrm{B}}T\boldsymbol{\mu}\ \delta(t-t'). && (1.38) \end{aligned}$$

In this thesis, an appropriate treatment of this drift term will be considered in various cases, including for the rotational stochastic dynamics of a colloidal rod (Chapter 3), and the for the many-particle interactions in Stokesian dynamics simulations (Chapters 4-6).

2

Entropic hopping of a colloidal rod

2.1 Background

Entropic forces govern many phenomena on the microscopic level, where fluctuations can drive a system away from its global energy minimum, allowing it to find configurations that are said to be *entropically* favoured.

The simplest example of an entropic force arises in the freely-jointed chain model of a polymer [57]. In this model, a polymer is comprised of a series of spherical beads separated by vectors of fixed length, each with a random orientation. The free energy of this system with a fixed end-to-end vector $\boldsymbol{r}_N$ can be shown to be $\mathcal{F} \propto k_\mathrm{B}Tr_N^2$. This gives rise to an effective thermodynamic force $\boldsymbol{f} = -\boldsymbol{\nabla}\mathcal{F} \propto -k_\mathrm{B}T\boldsymbol{r}_N$, which opposes any instantaneous extension $\boldsymbol{r}_N$. As the statistics of this system is described by the microcanonical ensemble — meaning the free energy is entirely entropic — this force is a pure entropic force.

Physical measurements of this force have been conducted through molecular stretching experiments, where a tethered polymer is externally manipulated by an optical trap that applies a force to a glass bead attached to the free end. By measuring the force required to achieve a fixed extension, force–extension curves have been found for various proteins and DNA molecules [58–60]. These experiments serve as a striking demonstration of fundamental statistical physics and offer hints of the biological importance of entropic forces [61].

In addition to providing the basis for elasticity in polymers, entropic forces also govern their dynamics in micropore translocation processes [62]. Sung and Park (1996), and later Muthukumar (1999) determined that a polymer diffusing through a pore has to overcome an entropic barrier due to the confinement [63, 64]. Translocation into and out of confined spaces may also be dominated by entropic effects due primarily to geometry. It was argued by Ali *et al.* (2006) that the spherical nature of viral capsids (out of which DNA is injected into a host cell through a porous channel) could in part be explained by their findings that polymer ejection our of spherical capsules tended to be faster than out of ellipsoidal ones [65].

In a ground-breaking experiment, the true entropic barrier-like nature of translocating through a micropore was demonstrated by Zhang *et al.* (2011) who reported the stochastic 'resonance' of a polymer confined to a dumb-bell shaped capsule comprising of two cavities separated by a pore [66]. Just like a particle in a double-well potential which randomly hops from one minimum to another across an energy barrier, they observed that a polymer periodically migrates from one cavity to another in equilibrium.

More recently, entropic forces have been found to play a crucial role in biomolecular self-organisation [67, 68], and particle diffusion through constrictive environments, around obstacles and along rough substrates [69–72].

In all of these experiments, entropic forces are usually identified on a heuristic basis following the freely-jointed-chain argument above, in which a number of distinguishing factors are observed: (1) that the forces are proportional to temperature; (2) that the dynamics are not entirely governed by a Hamiltonian or potential landscape; and (3) that purely geometric effects (such as confinement or spatial configuration) have a strong influence on the equilibrium distribution. Depletion interactions are also usually considered to be entropic forces [73].

Despite this increasing amount of experimental work, relatively little has been done theoretically to formalise the notion of entropic forces. A first attempt to formalise this idea and apply it to Brownian motion was made by Neumann (1980) [74], and this was expanded upon by Roos (2014) [75]. In their studies, they claim Brownian motion can be explained as a 'radial' entropic force that acts to push a particle away from its starting location. However, this is problematic as the force then depends on the particle's history, which cannot be the case for a memoryless Brownian particle. Most notably outside soft matter physics, Verlinde (2011) has put forward a hypothesis that explains gravitation as an emergent entropic force [76], and Wissner-Gross and Freer (2013) have suggested that path-entropic forces (i.e., entropic forces that arise due to path-derivatives of entropy functionals $S[\boldsymbol{X}(t)]$) play a role in 'intelligent' self-organisation [77]. In these studies, entropic forces are usually heuristically defined as some kind of derivative of either the entropy or free energy of the system. However, their interpretations of the entropic force are inconsistent, and it is apparent that a better understanding is required.

In this chapter we report on the entropic origin of a novel 'hopping' transition observed in the orientational states of a magnetic rod in a static field. Experiments conducted by our colleagues show that the rod hops between horizontal and vertical states with respect to a glass substrate, despite the latter state coming at an energetic cost of $\sim 3-4\ k_{\mathrm{B}}T$ in gravitational potential. When averaged over long times, we observe two peaks in the angle distribution corresponding to these two states.

We derive a statistical description of the states of the rod which match the experimental findings with no adjustable parameters. Our analysis finds that this transition is mediated by a competition between entropic and Hamiltonian forces, and we develop a generalised theory for entropic forces by considering the statistical interactions between hidden variables and observed variables in a system.

2.2 Experimental results

2.2.1 Synthesis and experiment design

This section details experiments conducted by Dr. Yongxiang Gao (in the group of Prof. Dirk Aarts) in which a single ferromagnetic rod is imaged by an optical microscope at high frequency, with its orientation subsequently tracked by automated

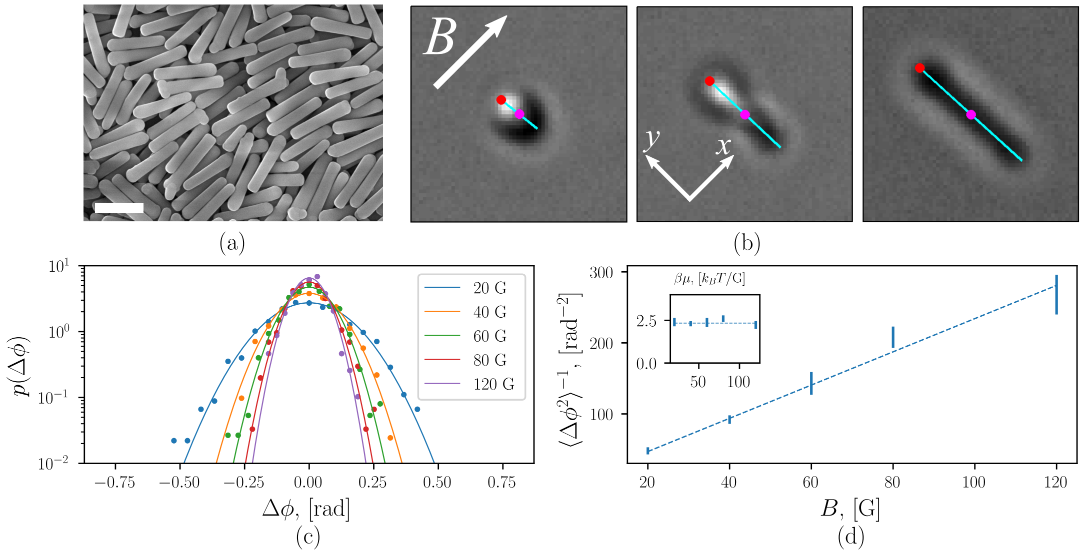

Figure 2.1: (a) Scanning electron micrograph of a dense collection of silica rods at ×5500 magnification (scale bar: 4 µm). (b) Optical snapshots of a single rod at three different points in time; lines displaying the detected projected length are overlaid. (c) Histogram of azimuthal angles when trapped by magnetic fields of varying strength with fitted Gaussians overlaid. (d) Applying the equipartition theorem ($k_BT \approx \mu B \langle \phi^2 \rangle$) to calculate μ using the fitted variances from (c).

image analysis. Experiments were carried out on rod-like silica particles. A high resolution image of a dense collection of these particles taken using a scanning electron microscope is shown in Fig. 2.1(a). The synthesis protocol is detailed in Ref. [78], and is based on a method of growing rod-like silica particles [79], where anisotropic growth is induced in an emulsion droplet in which silica condensation takes place. Typically, the rods grow with a width of 0.6–0.7 µm, and length 3–4 µm. To synthesise magnetic rods, the emulsion droplets were doped with magnetite (Fe_3O_4) nanoparticles on one end — hence giving rise to their bipartite Janus-rod structure. After the application of a saturating magnetic field, the rods retained a net magnetization $\boldsymbol{\mu}$, roughly perpendicular to their long axis.

The rods were suspended in water, mounted in a glass cell, and allowed to sediment to the bottom surface due to their density relative to water, $\Delta\rho = \rho_r - \rho_w \approx 0.9 \times 10^3\,\mathrm{kg\,m^{-3}}$. All experiments were conducted at room temperature on an inverted light microscope equipped with a ×60 oil-immersion lens. Bright

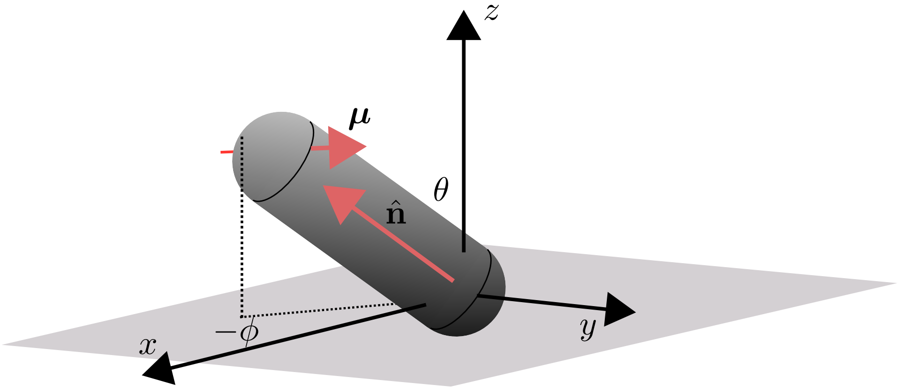

Figure 2.2: Orientational geometry of rod. The rod's long axis is spanned by $\hat{\boldsymbol{n}}$ and makes an angle θ with the z-axis. Its projection in the xy-plane subtends an angle ϕ with the x-axis. A permanent magnetic moment $\boldsymbol{\mu}$ is embedded in one end of the rod and rotates rigidly with it. The gravitational field acts in the -ve z-direction, and an external magnetic field $\boldsymbol{B}$, when applied, is along the x-direction, causing the rod to rotate from the configuration shown to one where $\boldsymbol{\mu}$ aligns with B.

field images were acquired at 20 frames per second.

Three typical snapshots of a rod are shown in Fig. 2.1(b). As the rod sediments in the image plane, it has a maximal projected length when lying flat on the surface of the slide and minimal projected length when standing vertically, normal to the surface. The geometry of the system is shown in Fig. 2.2. The image plane is spanned by $(\hat{\boldsymbol{x}}, \hat{\boldsymbol{y}})$, in which the rod's orientation vector $\hat{\boldsymbol{n}}$ makes the azimuthal angle ϕ. The polar angle, θ measures the alignment of the rod with the surface-normal.

Using an automated image analysis procedure, the lines shown in Fig. 2.1(b) are fitted to the projected image of the rod. The orientation and length of these lines are used to infer ϕ and θ respectively at each point in time.

2.2.2 Magnetic trapping

An external magnetic field was applied to the sample using a pair of Helmholtz coils with an approximate range of 0-150 gauss (G). In this chapter, the external magnetic field is always taken to lie along the x-direction.

When no magnetic field is present, the rod undergoes rotational Brownian motion in the plane, though gravity suppresses thermal fluctuations that drive its orientation away from the plane. In other words, the presence of the wall and gravity together roughly confine the particle's orientation to within the xy-plane.

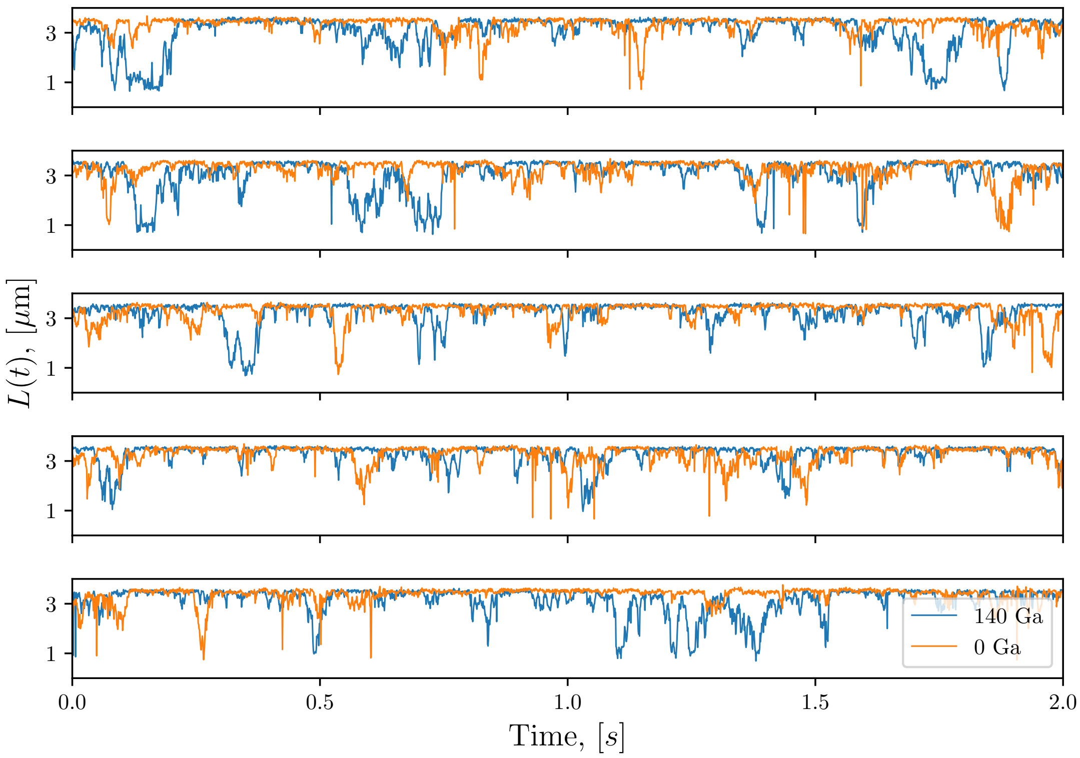

Figure 2.3: Five contiguous segments of a 10 second rod tracking experiment showing the projected length of the rod in the horizontal image plane in the presence of a magnetic field (blue) and without (orange).

When a magnetic field $\boldsymbol{B} = (B, 0, 0)$ is applied, the magnetic moment $\boldsymbol{\mu}$ is forced to align with the field in the x-direction. As $\boldsymbol{\mu}$ is perpendicular to the long-axis of the rod, the rod is then trapped, and lies along the y-axis [as can be seen in Fig. 2.1(b)].

To measure the strength of the magnetic moment, we can make use of the equipartition theorem: $\frac{1}{2}k_\mathrm{B}T = \langle -\boldsymbol{\mu} \cdot \boldsymbol{B} \rangle \approx \frac{1}{2}\mu B \langle \Delta\phi^2 \rangle$. For a given magnetic field strength B, we can measure the fluctuation $\Delta\phi(t)$ at each time step. The variance of these data then yield the strength μ. Figure 2.1(c) shows the distribution of $\Delta\phi$ for magnetic field strengths in the range 20–120 G, and Fig. 2.1(d) shows a linear relationship between $\langle \Delta\phi^2 \rangle$ and B, confirming that over the field strengths tested, the rod is ferromagnetic. Typically, the rods are synthesised with an approximate magnetic moment of strength 1–2 $k_BT\,\mathrm{G}^{-1}$.

With the same rod, two tracking experiments were conducted: one with a 0 G external field for 10 minutes, and one at 140 G for 20 minutes. Using the

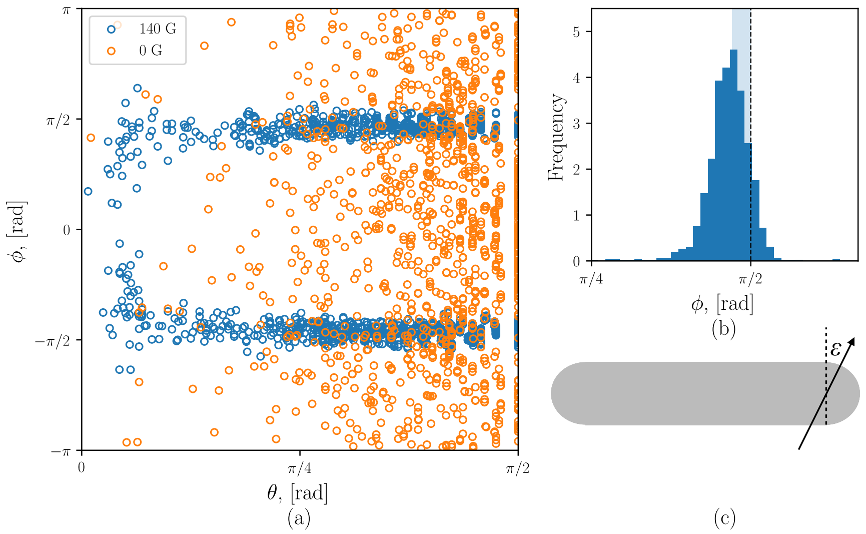

(a)

(b)

(c)

Figure 2.4: (a) Rod angles $(\theta(t), \phi(t))$ for 0 G field (orange) and 140 G field (blue) demonstrates the magnetic trapping (for clarity, only every tenth sequential point is displayed). (b) Histogram of $|\phi(t)|$ data shows a peaks shifted away from $\pi/2$ by a small amount ϵ. (c) The peak shift in (b) occurs because the magnetic moment $\boldsymbol{\mu}$ is not perfectly perpendicular to the rod, but makes an angle ϵ with the cross-sectional plane of the rod. For the rod used in these experiments, we measured $\epsilon = 7.2(1)^\circ$

calibration procedure described above, the rod was measured to have a magnetic moment strength $\mu = 1.2(1)\, k_B T\, \mathrm{G}^{-1}$.

Figure 2.3 shows the timeseries data for the computed projected length of a rod in both experiments. Inspection of the data reveal that when there is no magnetic field present, excursions from the maximal projected length are rare and short-lived. This is due to the effect of gravity, which confines the rod to horizontal orientations flush with the surface. However, when a magnetic field is applied, such excursions become more common and longer-lived: the rod is observed to ‘hop’ between horizontal and vertical states.

In Fig. 2.4, we can see the effects of the magnetic field on the scattered data $(\theta(t), \phi(t))$. When there is no magnetic field, the data are uniformly distributed in ϕ (due to azimuthal Brownian rotation) but sparser at smaller θ (due to gravity). However, under a magnetic field, the rod’s orientation becomes strongly trapped along the y-axis which manifests itself as the azimuthal angle being apparently tightly distributed around $\pm\phi/2$. However, plotting a histogram of $\phi(t)$ [Fig. 2.4(b)] reveals that it is distributed about $\phi_0 = \pm\phi/2 \mp \epsilon$ with $\epsilon = 7.2(1)^\circ$ being a small offset angle. This can be explained by reconsidering our assumption that the magnetic moment forms at an angle precisely perpendicular to the axis of the rod. If instead, we assume imperfections in the synthesis which result in the magnetic moment being formed at an angle ϵ to the cross sectional plane of the rod [as demonstrated in Fig. 2.4(c)], then we would expect the axis of the rod to be distributed about $\phi_0 = \pm\phi \mp \epsilon$ under a magnetic field.

The statistical mechanism for this 'hopping' process will be the focus of the remainder of this chapter. We will initially focus on the ideal case for a rod with $\epsilon = 0$, but will relax this restriction in order to fit our theory to the data.

2.3 Computing the probability distribution

2.3.1 Geometrical description

The geometry of the rods we use, including their axis-perpendicular magnetic moment, is similar to that described by Dhar *et al.* (2007) [80], however they only study the dynamic properties of the rods when placed in a rotating magnetic field. The shape of a rod is that of a hemispherically capped cylinder, which we term *cylindrospherical*. To denote the direction of the long axis of the rod, we use a vector $\hat{\boldsymbol{n}}$ which makes an angle θ with the z-axis in the laboratory frame, and an angle ϕ in the xy-plane. These are the experimentally observable degrees of freedom. However, the embedded permanent magnetic moment $\boldsymbol{\mu}$ is perpendicular to $\hat{\boldsymbol{n}}$ (assuming $\epsilon = 0$) and requires a third angle γ to parameterise its direction in the cross-sectional plane of the rod. This angle is not measurable experimentally but it is nevertheless important for a full description of the rod.

If we consider the fixed-body coordinate system of the rod, (x', y', z'), then $\hat{\boldsymbol{n}}$ lies along the z'-axis and $\boldsymbol{\mu}$ lies mostly (or entirely, for $\epsilon = 0$) along the x'-axis which in general breaks axial symmetry. We use the conventional Euler angle description [80] to relate the fixed-body frame of the rod to the lab-frame via

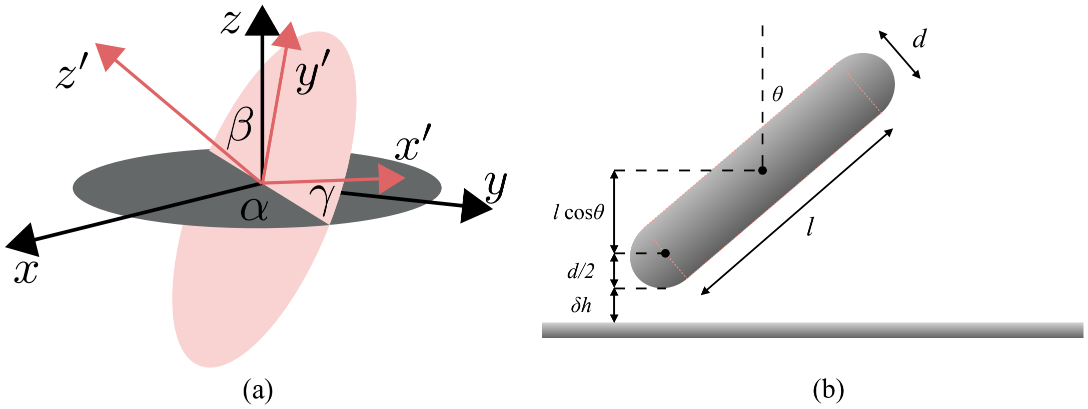

Figure 2.5: (a) Euler angles for describing the fixed-body orientation of the rod, where $\boldsymbol{n} = \boldsymbol{z}'$, $\boldsymbol{\mu} = m\hat{\boldsymbol{x}}'$, $\beta = \theta$, $\alpha = \phi + \pi/2$. (b) Decomposition of the centre-of-mass height of the rod into an angular component $l\cos\theta$, constant component $d/2$, and pure translational component δh.

$(x', y', z')^T = \mathbf{R}_z(\alpha)\mathbf{R}_x(\beta)\mathbf{R}_z(\gamma)(x, y, z)^T$, where $\mathbf{R}_i(\chi)$ denotes rotation about lab-frame axis i, through angle χ. Under this conventional description, the Euler angles are related to the angles ϕ and θ by: $\alpha = \phi + \frac{\pi}{2}$, and $\beta = \theta$ [Fig. 2.5(a)].

Hence, each state of the rod $(\boldsymbol{\mu}, \hat{\boldsymbol{n}})$ can be described in terms of these angles and gives rise to an instantaneous energy $\mathcal{H} = -\boldsymbol{\mu} \cdot \boldsymbol{B} - \bar{m}gh$, where $\bar{m} = \Delta\rho V$ is the effective mass for a rod with volume V, and h is the height of the centre-of-mass of the rod. We calculate the volume by summing the volume of the cylindrical section plus the two hemispherical caps: $V = \frac{4}{3}\pi(d/2)^3 + \pi l(d/2)^2$. The height is given by $h = d/2 + l\cos\theta + \delta h$, where δh is the minimum separation between the surface and the rod as shown in Fig. 2.5(b). We may also write the height as $h = l(\hat{\boldsymbol{n}} \cdot \hat{\boldsymbol{z}}) + d/2 + \delta h$, making explicit the dependence of the gravitational energy term on $\hat{\boldsymbol{n}}$. The potential energy therefore comprises an orientational part $\mathcal{H}_{\text{rot}}(\hat{\boldsymbol{n}}, \boldsymbol{\mu})$ plus a translational part $\mathcal{H}_{\text{tr}}(\delta h)$. The $d/2$ term in h contributes only a constant to the total energy and is therefore ignored. Likewise, the translational part of the potential is entirely decoupled from the orientational part, and as δh is not measured in experiments anyway, it may be also be ignored.

2.3.2 Canonical ensemble description

Full system Hamiltonian

Dropping the subscript, and defining $g\hat{\boldsymbol{z}} = -\boldsymbol{g}$, we can write the full orientational energy as:

$$\mathcal{H}(\hat{\boldsymbol{n}}, \boldsymbol{\mu}) = -\boldsymbol{\mu} \cdot \boldsymbol{B} - \frac{\bar{m}l}{2}\hat{\boldsymbol{n}} \cdot \boldsymbol{g}. \tag{2.1}$$

We assume that the states $(\hat{\boldsymbol{n}}, \boldsymbol{\mu})$ form a canonical ensemble, and that the probability distribution function (pdf) from which states are drawn is proportional to the Boltzmann factor:

$$p(\hat{\boldsymbol{n}}, \boldsymbol{\mu}) \propto \exp\left[-\mathcal{H}(\hat{\boldsymbol{n}}, \boldsymbol{\mu})/k_{\mathrm{B}}T\right] \tag{2.2}$$

Our ultimate goal is to obtain the marginal pdf for the polar angle, $p(\theta)$. For this, we first need to rewrite Eq. (2.2) in terms of the angles (θ, ϕ, γ). This can be achieved by evaluating the quantities in Eq. (2.1) in the rod's fixed-body frame. Recall that the transformation which converts vectors in the lab-frame to the rod-frame is given by $\mathbf{R} = \mathbf{R}_z(\alpha)\mathbf{R}_x(\beta)\mathbf{R}_z(\gamma)$. Writing out this transformation, and substituting in $\alpha = \phi + \pi/2$, and $\beta = \theta$ yields:

$$\mathbf{R} = \begin{bmatrix} -\sin\phi\cos\gamma - \cos\phi\cos\theta\sin\gamma & \sin\phi\sin\gamma - \cos\phi\cos\theta\cos\gamma & \cos\phi\sin\theta \\ \cos\phi\cos\gamma - \sin\phi\cos\theta\sin\gamma & -\sin\phi\cos\theta\cos\gamma - \cos\phi\sin\gamma & \sin\phi\sin\theta \\ \sin\theta\sin\gamma & \sin\theta\cos\gamma & \cos\theta \end{bmatrix}.$$

The quantities $\boldsymbol{B} = B\hat{\boldsymbol{x}}$ and $\boldsymbol{g} = -g\hat{\boldsymbol{z}}$ in the lab-frame transform to $\boldsymbol{B}' = B\mathbf{R}\hat{\boldsymbol{x}}$ and $\boldsymbol{g}' = -g\mathbf{R}\hat{\boldsymbol{z}}$ in the rod-frame, where the magnetic moment and rod orientation vectors are written $\boldsymbol{\mu}' = \mu\hat{\boldsymbol{x}}'$ and $\hat{\boldsymbol{n}}' = \hat{\boldsymbol{z}}'$. We can then evaluate the potential as:

$$\mathcal{H}(\phi, \theta, \gamma) = -\mu B\hat{\boldsymbol{x}}' \cdot (\mathbf{R}\hat{\boldsymbol{x}}) + \frac{\bar{m}gl}{2}\hat{\boldsymbol{z}}' \cdot (\mathbf{R}\hat{\boldsymbol{z}}). \tag{2.3}$$

Using the explicit form for $\mathbf{R}$ gives:

$$\mathcal{H}(\phi, \theta, \gamma) = -\mu B\left(\sin\phi\cos\gamma + \cos\phi\cos\theta\sin\gamma\right) + \frac{\bar{m}gl}{2}\cos\theta. \tag{2.4}$$

This has global minima at $(\theta = \pi/2, \phi = \pi/2, \gamma = 0)$ and $(\theta = \pi/2, \phi = -\pi/2, \gamma = \pi)$ which both correspond to the rod lying flat in the plane, with $\boldsymbol{\mu}$ directed along

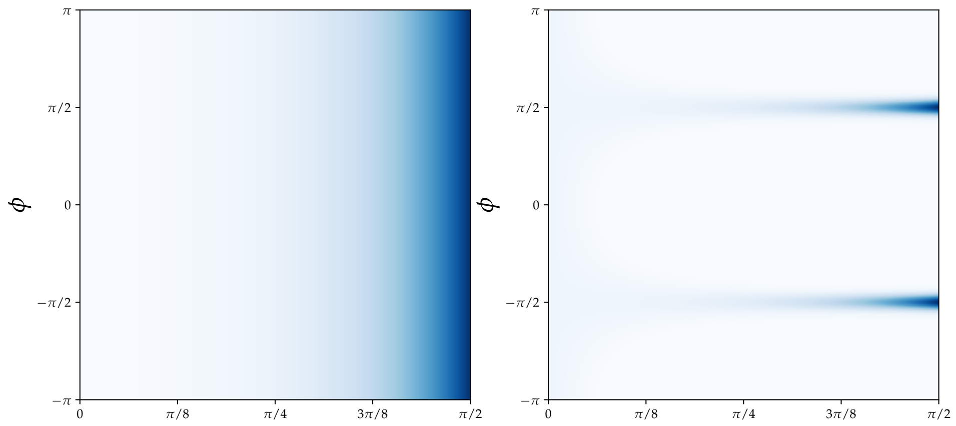

(a) θ (b) θ

Figure 2.6: Marginal probability distribution for rod orientation over observable degrees of freedom, $p(\phi, \theta)$, for (a) $B = 0\,\mathrm{G}$, and (b) $B = 140\,\mathrm{G}$.

$\hat{\boldsymbol{x}}$, and with $\hat{\boldsymbol{n}}$ directed along +ve or −ve $\hat{\boldsymbol{y}}$ respectively, as observed (up to corrections in ϵ) in Fig. 2.4(a).

We can imagine configuring the system in the global potential minimum described above and then investigate what happens as θ is varied. With fixed $\phi = \phi_0 = \pi/2$ and $\gamma = \gamma_0 = 0$, the potential as a function of θ becomes $\mathcal{H}(\theta|\phi_0, \gamma_0) = -\mu B + (\bar{m}gl/2)\cos\theta$. This energy monotonically increases as θ is decreased from $\pi/2$ to 0. Therefore, we can rule out the hopping behaviour being due to ergodic thermal motion in a double-well potential. There is only a saddle point at $\theta = 0$, so the potential alone cannot explain why the $\theta = 0$ state becomes more favourable relative to the no-field case.

Marginal distribution over observable angles

The pdf over the angles, $p(\phi, \theta, \gamma)$ can be computed using Eqs. (2.2) and (2.4). However, as γ is not observable in the experiment due to the axisymmetry of the rod, we wish to calculate the marginal distribution that may be found by integrating γ out of the full pdf:

$$p(\phi, \theta) = \frac{1}{\mathcal{Z}} \int_0^{2\pi} \mathrm{d}\gamma \ \exp\left[\frac{\mu B}{k_\mathrm{B} T} \left(\sin\phi\cos\gamma + \cos\phi\cos\theta\sin\gamma\right) - \frac{\bar{m}gl}{2k_\mathrm{B}T}\cos\theta\right]. \quad (2.5)$$

This integral may be performed analytically to obtain,

$$p(\phi,\theta) = \frac{1}{\mathcal{Z}} \exp\left[-\frac{\bar{m}gl}{2k_{\mathrm{B}}T}\cos\theta\right] I_0\left(\frac{\mu B}{k_{\mathrm{B}}T}\sqrt{1-\cos^2\phi\sin^2\theta}\right), \tag{2.6}$$

where $I_0(x)$ is the modified Bessel function of the first kind. This function is plotted in 2-dimensions over $\theta \in [0, \pi/2]$ and $\phi \in [-\pi, \pi]$ for $B = 0\,\mathrm{G}$ and $140\,\mathrm{G}$ in Figs. 2.6(a) and 2.6(b) respectively. These analytical distributions qualitatively match the experimental results in Fig. 2.4(a).

2.3.3 Distribution over polar angles

The next step is to integrate out the dependence of $p(\phi,\theta)$ on ϕ to obtain the marginal distribution over polar angles, $p(\theta)$. For convenience, we set $a = \bar{m}gl/2k_{\mathrm{B}}T$ and $b = \mu B/k_{\mathrm{B}}T$. The distribution $p(\theta)$ is found by numerically integrating the Bessel function:

$$p(\theta) = \frac{\mathrm{e}^{-a\cos\theta}}{\mathcal{Z}} \int_{-\pi}^{\pi} I_0\left(b\sqrt{1-\cos^2\phi\sin^2\theta}\right) \mathrm{d}\phi. \tag{2.7}$$

The only parameters that enter our model are a and b, which both contain experimentally measurable quantities, and hence there are no free parameters.

To compare the $p(\theta)$ with experiment, we first have to transform it so that it represents a real probability on the measure θ. The absolute probability of observing a polar angle Θ in the range $[\theta, \theta + \mathrm{d}\theta]$ is $\mathrm{Prob}[\theta < \Theta < \theta + \mathrm{d}\theta] \approx p(\theta)\sin\theta\mathrm{d}\theta$. Hence it is the quantity $p(\theta)\sin\theta$ that we must compare with the histogram of $\theta(t)$ data obtained experimentally.

This comparison is shown in Fig. 2.7(a). The data clearly show an increased absolute probability of observing low-θ (i.e., vertical) states. The theory fits the data well with no free parameters. However there appears to be a systematic excess in frequency for very low-θ data around $\theta \approx \pi/16$. This is likely due to systematic error in the image analysis procedure uniformly underestimating the projected length, L_p, for low-θ.

To factor out such error, we plot the relative frequencies in Fig. 2.7(b). The theoretical relative likelihood $p(\theta|140\,\mathrm{G})/p(\theta|0\,\mathrm{G})$ fits these data well but at low-θ

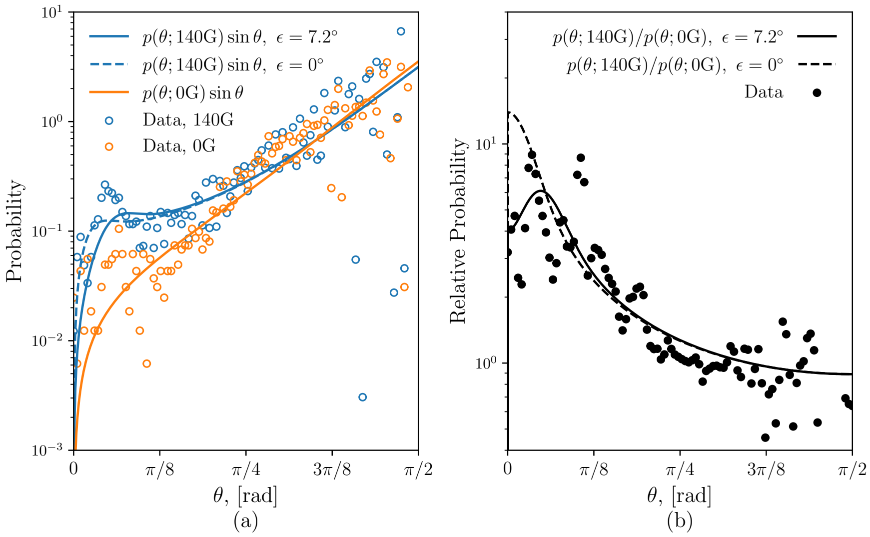

(a) (b)

Figure 2.7: (a) Histogram of $\theta(t)$ shows a markedly increased tendency for vertical states (small-θ) to be realised when a magnetic field is present (blue circles) with respect to a free rod (orange circles). The curves represent absolute probability weightings $p(\theta)\sin\theta$ where we have analytically found $p(\theta)$ using independently measured parameters μ, ϵ, m, L, and d. (b) The relative distribution $p(\theta|140\,\text{G})/p(\theta|0\,\text{G})$ agrees well with the theoretical calculations, showing an $\mathcal{O}(10)$ increase in likelihood for small-θ states due to the magnetic field compared to no field.

there is a divergence between the two. In particular, there is a peak at around $\theta \approx \pi/16$ in the relative frequencies in the data, but the theory predicts the peak to occur at exactly $\theta = 0$.

Up until now in the theory, we have not accounted for a finite ϵ-angle imperfection in the orientation of the magnetic moment relative to the cross-sectional plane of the rod. To correct for this, we follow the same procedure as above in deriving $p(\theta)$, but in Eq. (2.3), we use $\boldsymbol{\mu}' = \cos\epsilon\boldsymbol{x}' + \sin\epsilon\boldsymbol{z}'$. This results in a potential energy:

$$\begin{aligned}\mathcal{H}(\phi,\theta,\gamma) &= -\mu B(\cos\epsilon[\sin\phi\cos\gamma + \cos\phi\cos\theta\sin\gamma] \quad (2.8)\\ &\quad + \sin\epsilon\cos\phi\sin\theta) + \frac{\bar{m}gl}{2}\cos\theta, \quad (2.9)\end{aligned}$$

and marginal pdf:

$$\begin{aligned}p(\phi,\theta) &= \frac{1}{\mathcal{Z}}\exp\left(-a\cos\theta - b\sin\epsilon\cos\phi\sin\theta\right) \quad (2.10)\\ &\quad \times I_0\left(b\cos\epsilon\sqrt{1-\cos^2\phi\sin^2\theta}\right). \quad (2.11)\end{aligned}$$

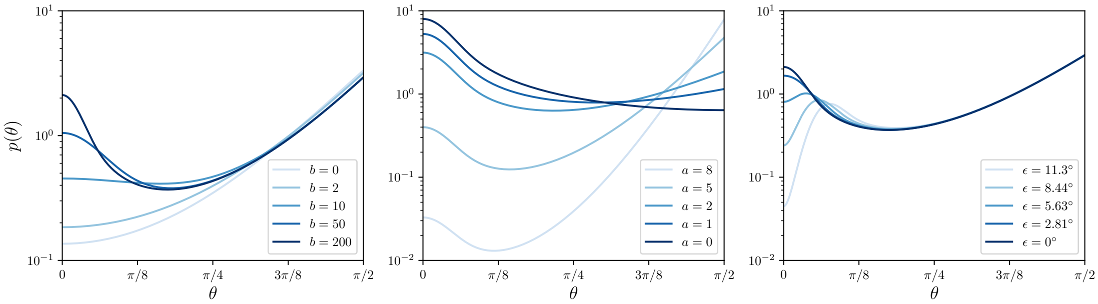

(a) (b) (c)

Figure 2.8: Marginal pdf for rod polar angle, $p(\theta)$. (a) The transition from monostability to bistability as a function of increasing external magnetic field, B. The gravitational field strength a is kept constant. (b) Increasing the gravitational energy (eg., by increasing rod size) very quickly suppresses the low-θ states. Decreasing the gravitational energy, however, results in the $\theta = 0$ state dominating. (c) Increasing the magnetic moment offset angle ϵ gradually destroys the peak at $\theta = 0$.

This more complicated expression may be numerically integrated to compute $p(\theta)$. The results are shown together with the previous results for $\epsilon = 0$ in Fig. 2.7. The correction due to ϵ alters the absolute probabilities in the low-θ region. The relative likelihood now does display a peak in roughly the same location as the data.

2.4 Theoretical investigation

2.4.1 Transition to bistability

Both the data and the equilibrium theory show that the system transitions from a monotonic pdf in the case of no magnetic field — where gravity alone suppresses low-θ excursions — to a bistable pdf in which the low-θ state becomes relatively favoured. We can get a better idea of this transition by plotting $p(\theta)$ for a larger range of b, as shown in Fig. 2.8(a), where the gravitational energy scale calculated for the rod is kept constant at the measured $a = \bar{m}gl/2k_\mathrm{B}T$.

When no magnetic field is present, vertical (low-θ) states are exponentially suppressed. At moderate ($b \approx 10$) magnetic field strengths a peak at $\theta = 0$ emerges, and becomes increasingly prominent. At large field strengths ($b \approx 200$) the peak becomes almost as prominent as the $\theta = \pi/2$ ground state.

We may also ask what the effect of increasing or decreasing the gravitational energy strength would be. This may be achieved for instance, by altering the length

l of the cylindrical section of the rod at constant diameter d, or equivalently by varying the relative density $\Delta\rho$ of the particle in the synthesis process. In the limit $l \to 0$, the aspect ratio of the particle approaches 1 and, assuming contact with the glass slide, we have a vanishing gravitational potential ($a \to 0$). In this limit, the vertical ($\theta = 0$) state becomes increasingly probable until it becomes more likely than the horizontal state ($\theta = \pi/2$). In Fig. 2.8(b), this transition can be observed clearly. As a decreases, the relative magnitude $p(0)/p(\pi/2)$ increases and passes through 1. When $a = 0$ exactly, $p(\theta)$ becomes a monotonically decreasing function of θ, which is qualitatively opposite to the case of finite a with $b = 0$.

In the opposite limit, as a is modestly increased ($b = 8$), the vertical state becomes strongly suppressed even though the magnetic field strength ($b = 140$) is much higher.

We also investigate how ϵ affects the shape of the pdf. Increasing ϵ quickly destroys the stability of the vertical state. This is because ϵ has the effect of attributing a strong magnetic potential cost to the vertical state as well as the gravitational cost. The low-θ peak decreases in magnitude, and shifts to larger θ for increasing ϵ. We can understand this by noting that in the limit $\epsilon \to \pi/2$, $\boldsymbol{\mu}$ and $\hat{\boldsymbol{n}}$ become colinear, and hence the Hamiltonian of the system takes the form $\mathcal{H} = -\hat{\boldsymbol{n}} \cdot \tilde{\boldsymbol{f}}$, where $\tilde{\boldsymbol{f}} = -\mu\boldsymbol{B} + (\bar{m}l/2)\boldsymbol{g}$ is an effective external field. As the gravitational field is much weaker than the magnetic field, this may be approximated as $\mathcal{H} \approx -\mu B\hat{\boldsymbol{n}} \cdot \hat{\boldsymbol{x}}$ leading to $p(\phi, \theta) = \frac{1}{\mathcal{Z}} \exp[-(\mu B/k_{\mathrm{B}}T) \cos\phi \sin\theta]$ and $p(\theta) = \frac{1}{\mathcal{Z}} I_0[(\mu B/k_{\mathrm{B}}T) \sin\theta]$, which suppresses low-$\theta$ states strongly for large $\mu B/k_{\mathrm{B}}T$.

2.4.2 Entropic barrier

We have shown that the overall effect of applying a large magnetic field is to encourage the population of low-θ states that are otherwise gravitationally suppressed, revealing a minimum at $\theta_c \neq 0$. By considering the quantity $(-)\ln p(\theta)$, the minimum of $p(\theta)$ corresponds to an effective barrier that separates the two bistable states. We have shown that this barrier cannot be entirely due to the potential landscape $\mathcal{H}(\phi, \theta, \gamma)$ and so we must look to entropic arguments to explain its origin.

Our question now is how to interpret the marginal pdf $p(\theta)$ obtained by integrating out the other degrees of freedom in the joint distribution $p(\phi,\theta,\gamma)$, when the degrees of freedom (ϕ,θ,γ) are coupled in a nonlinear fashion. This is a general question that we may ask of any system whose state $\boldsymbol{X} = (X_1, X_2, ...X_n)$ comprises of n degrees of freedom with nonlinear coupling.

Linearly coupled system

It is instructive to first look at a linearly coupled system which we define as one in which the forces in the system are a linear function of its state variables: $\boldsymbol{F} = -\mathbf{K}\boldsymbol{X}$. Such a system derives from a Hamiltonian that may be written in harmonic form $\mathcal{H}(\boldsymbol{X}) = \frac{1}{2}\boldsymbol{X}^T\mathbf{K}\boldsymbol{X}$ where $\mathbf{K}$ is a symmetric matrix of coupling coefficients. First we partition the system into two interacting subsystems, $\boldsymbol{X} = (\boldsymbol{x},\boldsymbol{y})$, where $\boldsymbol{x} = (x_1, x_2, ..., x_n)$ represents the state of the degrees of freedom of interest whose marginal pdf we wish to isolate by integrating out the degrees of freedom $\boldsymbol{y} = (y_1, y_2, ...y_m)$. The coupling tensor may be decomposed into subcomponents $\mathbf{K} = \begin{bmatrix}\mathbf{K}_{xx} & \mathbf{K}_{xy}\\ \mathbf{K}_{xy}^T & \mathbf{K}_{yy}\end{bmatrix}$. Therefore, the Hamiltonian of this system is written in full as:

$$\begin{aligned}\mathcal{H}(\boldsymbol{x},\boldsymbol{y}) &= \mathcal{H}_x(\boldsymbol{x}) + \mathcal{H}_y(\boldsymbol{y}) + \mathcal{H}_{xy}(\boldsymbol{x},\boldsymbol{y}) &\quad (2.12)\\ &= \frac{1}{2}\boldsymbol{x}^T\mathbf{K}_{xx}\boldsymbol{x} + \frac{1}{2}\boldsymbol{y}^T\mathbf{K}_{yy}\boldsymbol{y} + \boldsymbol{x}^T\mathbf{K}_{xy}\boldsymbol{y}, &\quad (2.13)\end{aligned}$$

where $\mathcal{H}_x$ and $\mathcal{H}_y$ are the pure Hamiltonians for each subsystem when uncoupled, and $\mathcal{H}_{xy}$ is the interaction potential. From this, $p(\boldsymbol{x})$ may be obtained by integrating over the joint distribution $p(\boldsymbol{x},\boldsymbol{y}) \propto \mathrm{e}^{-\mathcal{H}(\boldsymbol{x},\boldsymbol{y})}$ — where we have set $k_\mathrm{B}T = 1$. This can be done by the standard method of Gaussian integrals (described in Appendix A.1) with the result that

$$p(\boldsymbol{x}) = \sqrt{\frac{\det\mathbf{K}}{\det\mathbf{K}_{yy}}}\exp\left[-\frac{1}{2}\boldsymbol{x}^T\left(\mathbf{K}_{xx} - \mathbf{K}_{xy}\mathbf{K}_{yy}^{-1}\mathbf{K}_{xy}^T\right)\boldsymbol{x}\right]. \quad (2.14)$$

This is simply a Gaussian distribution for an equivalent system $\{\boldsymbol{x}\}$, with Hamiltonian $\mathcal{H}'(\boldsymbol{x}) = \frac{1}{2}\boldsymbol{x}^T\mathbf{K}'\boldsymbol{x}$ containing the effective coupling tensor $\mathbf{K}' = \mathbf{K}_{xx} - \mathbf{K}_{xy}\mathbf{K}_{yy}^{-1}\mathbf{K}_{xy}^T$. This effective coupling tensor can be found by considering the quantity $\langle\mathcal{H}_{xy}\rangle_{y|x} = \langle\boldsymbol{x}^T\mathbf{K}_{xy}\boldsymbol{y}\rangle_{y|x}$, i.e., the interaction potential averaged over the hidden variables $\{\boldsymbol{y}\}$ and conditioned on the observables $\{\boldsymbol{x}\}$.[1] Computing this conditional expectation (details of which can be found in Appendix A.1), we find that it is equal to $-\frac{1}{2}\boldsymbol{x}^T\mathbf{K}_{xy}\mathbf{K}_{yy}^{-1}\mathbf{K}_{xy}^T\boldsymbol{x}$. Inserting this result into Eq. (2.14) gives:

$$\ln p(\boldsymbol{x}) \propto -\mathcal{H}_x(\boldsymbol{x}) - \langle \mathcal{H}_{xy}(\boldsymbol{x},\boldsymbol{y})\rangle_{y|x} \tag{2.15}$$

When considering the equilibrium state of subsystem $\{\boldsymbol{x}\}$, the effect of the linear coupling to $\{\boldsymbol{y}\}$ is therefore to perturb the pure system Hamiltonian $\boldsymbol{x}^T\mathbf{K}_{xx}\boldsymbol{x}$. In particular, the quantity $\ln p(\boldsymbol{x})$ is negatively proportional to the effective Hamiltonian $\mathcal{H}'(\boldsymbol{x}) = \frac{1}{2}\boldsymbol{x}^T\mathbf{K}'\boldsymbol{x}$, which as a quadratic function of $\boldsymbol{x}$, has a single minimum. Therefore, linear coupling to unobserved degrees of freedom (1) allows us to interpret $\ln p(\boldsymbol{x})$ in terms of an effective potential landscape, and (2) does not allow the emergence of bistability in $p(\boldsymbol{x})$ such as the one reported above.

Furthermore, we can inspect the gradients of $\ln p(\boldsymbol{x})$ with respect to $\boldsymbol{x}$. In doing so we find:

$$-\frac{\partial}{\partial \boldsymbol{x}}\ln p(\boldsymbol{x}) = \boldsymbol{f}_x(\boldsymbol{x}) + \langle \boldsymbol{f}_{xy}(\boldsymbol{x},\boldsymbol{y})\rangle_{y|x}. \tag{2.16}$$

This explicitly gives the gradients in $\ln p(\boldsymbol{x})$ in terms of a pure force $\boldsymbol{f}_x(\boldsymbol{x})$, and an ensemble averaged force $\langle \boldsymbol{f}_{xy}(\boldsymbol{x},\boldsymbol{y})\rangle_{y|x}$ which we identify as an entropic force due to its intrinsic statistical nature.

We note that with no coupling, for instance a 2-dimensional harmonic potential $H(x,y) = \frac{1}{2}k_x x^2 + \frac{1}{2}k_y y^2$, then the marginal log-distribution is trivially proportional to the pure potential landscape: $\ln p(x) \propto -\frac{1}{2}k_x x^2$.

---

[1] The expectation of a function $f(x,y)$ over y, conditioned on x is defined as $\langle f(x,y)\rangle_{y|x} = \int f(x,y)p(y|x)\mathrm{d}y = \int f(x,y)p(x,y)/p(x)\mathrm{d}y$.

Nonlinearly coupled systems

If we cannot write the Hamiltonian of $\boldsymbol{X} = (\boldsymbol{x}, \boldsymbol{y})$ in quadratic form, then interpreting $\ln p(\boldsymbol{x})$ becomes trickier. By definition:

$$\begin{aligned}
\ln p(\boldsymbol{x}) &:= \ln\left\{\frac{1}{\mathcal{Z}}\int_{\{y\}} \mathrm{d}\boldsymbol{y}\ \mathrm{e}^{-\mathcal{H}(\boldsymbol{x},\boldsymbol{y})}\right\} && (2.17)\\
&= \ln\left\{\int_{\{y\}} \mathrm{d}\boldsymbol{y}\ \mathrm{e}^{-\mathcal{H}_x(\boldsymbol{x})-\mathcal{H}_y(\boldsymbol{y})-\mathcal{H}_{xy}(\boldsymbol{x},\boldsymbol{y})}\right\} - \mathcal{F} && (2.18)\\
&= -\mathcal{H}_x(\boldsymbol{x}) + \ln\left\{\int_{\{y\}} \mathrm{d}\boldsymbol{y}\ \mathrm{e}^{-\mathcal{H}_y(\boldsymbol{y})-\mathcal{H}_{xy}(\boldsymbol{x},\boldsymbol{y})}\right\} - \mathcal{F}, && (2.19)
\end{aligned}$$

where $\mathcal{F} = -\ln\mathcal{Z}$ is the free energy of the combined system.

In this case, the perturbation term in braces cannot be interpreted as easily as before. It is clearly not the same as its counterpart in the linearly coupled case, $\langle\mathcal{H}_{xy}(\boldsymbol{x}, \boldsymbol{y})\rangle_{y|x}$, and hence we cannot say that $\ln p(\boldsymbol{x})$ represents an effective Hamiltonian or potential landscape.

However, we are able to connect this to our previous result by taking the gradient with respect to states $\{\boldsymbol{x}\}$:

$$\frac{\partial}{\partial\boldsymbol{x}}\ln p(\boldsymbol{x}) = -\frac{\partial}{\partial\boldsymbol{x}}\mathcal{H}_x(\boldsymbol{x}) - \frac{\int_{\{y\}}\mathrm{d}\boldsymbol{y}\ \frac{\partial\mathcal{H}_{xy}}{\partial\boldsymbol{x}}\mathrm{e}^{-\mathcal{H}_y(\boldsymbol{y})-\mathcal{H}_{xy}(\boldsymbol{x},\boldsymbol{y})}}{\int_{\{y\}}\mathrm{d}\boldsymbol{y}\ \mathrm{e}^{-\mathcal{H}_y(\boldsymbol{y})-\mathcal{H}_{xy}(\boldsymbol{x},\boldsymbol{y})}}. \qquad (2.20)$$

By multiplying the second term on the right-hand-side by $\frac{\exp[-\mathcal{H}_x(\boldsymbol{x})]}{\exp[-\mathcal{H}_x(\boldsymbol{x})]}$, it can be seen that it has the form $\int_{\{y\}}\mathrm{d}\boldsymbol{y}[\partial\mathcal{H}_{xy}/\partial\boldsymbol{x}]p(\boldsymbol{x},\boldsymbol{y})/p(\boldsymbol{x}) = \int_{\{y\}}\mathrm{d}\boldsymbol{y}[\partial\mathcal{H}_{xy}/\partial\boldsymbol{x}]p(\boldsymbol{y}|\boldsymbol{x})$. This is the expectation of $\boldsymbol{\nabla}_{\boldsymbol{x}}\mathcal{H}_{xy}(\boldsymbol{x}, \boldsymbol{y}) = -\boldsymbol{f}_{xy}$ over $\{\boldsymbol{y}\}$ conditioned on $\boldsymbol{x}$. Hence, the gradient of $\ln p(\boldsymbol{x})$ has the same form as in Eq. (2.16). Although $\ln p(\boldsymbol{x})$ can no longer be interpreted as an effective Hamiltonian, its gradient has the form of a total thermodynamic force: containing in general, contributions from both energetic and entropic forces.

Magnetic rod thermodynamics

In our notation for the degrees of freedom of the rod, the Hamiltonian [Eq. (2.4)] $\mathcal{H}(\phi, \theta, \gamma)$ is nonlinear but can be decomposed into components

$$\mathcal{H}(\phi, \theta, \gamma) = \mathcal{H}_{\mathrm{mag}}(\phi, \theta, \gamma) + \mathcal{H}_{\mathrm{gr}}(\theta), \qquad (2.21)$$

where $\mathcal{H}_{\rm mag}$ is the magnetic term and $\mathcal{H}_{\rm gr}$ is the gravitational term. Then, for the gradient of $\ln p(\theta)$ we can write:

$$\frac{\partial}{\partial\theta}\ln p(\theta) = -\frac{\partial\mathcal{H}_{\rm gr}}{\partial\theta} - \left\langle \frac{\partial\mathcal{H}_{\rm mag}}{\partial\theta} \right\rangle_{\phi,\gamma|\theta}. \tag{2.22}$$

This tells us that the thermodynamic force^2 acting on the variable θ is a competition between the purely energetic gravitational force, and the entropic force due to the magnetic trapping. Eq. (2.22) explicitly tells us why it was naive to characterise the observation of hopping as counter-intuitive. Recall we argued that from the global energy minimum, changing θ alone only increased the gravitational energy while keeping the magnetic energy constant. Mathematically this argument corresponds to stating: $\frac{\partial\mathcal{H}}{\partial\theta} = \frac{\partial\mathcal{H}_{\rm gr}}{\partial\theta} < 0$ as $\frac{\partial\mathcal{H}_{\rm mag}}{\partial\theta}|_{\phi_0,\gamma_0} = 0$, hence low-$\theta$ states should be suppressed regardless of $\mathcal{H}_{\rm mag}$. However, Eq. (2.22) tells us that we must take into account the entropic cost of fluctuations in $\frac{\partial\mathcal{H}_{\rm mag}}{\partial\theta}$ across the entire ensemble of angles (ϕ,γ).

In Fig. 2.9 we plot slices of the magnetic potential $\mathcal{H}_{\rm mag}$ in (γ,ϕ) for three different values of θ: $\theta=\pi/2$ where the rod is flat, $\theta=\pi/20$ where it is near vertical, and an intermediate angle $\theta=3\pi/8$ roughly corresponding to the θ at which $\ln p(\theta)$ is a minimum. Despite the fact that in each slice, the minimum energy is constant and zero (corresponding to total alignment between $\boldsymbol{\mu}$ and $\boldsymbol{B}$), we see that this minimum undergoes a transition from being tightly constrained in both ϕ and γ, to being more loosely constrained along just a single degree of freedom $(\phi+\gamma)$. To see why this is, we consider expanding $\mathcal{H}_{\rm mag}$ around the minimum $(\phi_0=\pi/2, \gamma_0=0)$ in the two opposing limits of θ:

$$\begin{aligned} \mathcal{H}_{\rm mag}|_{\theta=\frac{\pi}{2}} &= -\mu B\cos\gamma\sin\phi && (2.23)\\ \implies \mathcal{H}_{\rm mag}|_{\theta=\frac{\pi}{2}} &\approx \frac{1}{2}\mu B(\Delta\phi^2+\Delta\gamma^2), && (2.24)\end{aligned}$$

and

$$\begin{aligned} \mathcal{H}_{\rm mag}|_{\theta=0} &= -\mu B\sin(\phi+\gamma) && (2.25)\\ \implies \mathcal{H}_{\rm mag}|_{\theta=0} &\approx \frac{1}{2}\mu B(\Delta\phi+\Delta\gamma)^2, && (2.26)\end{aligned}$$

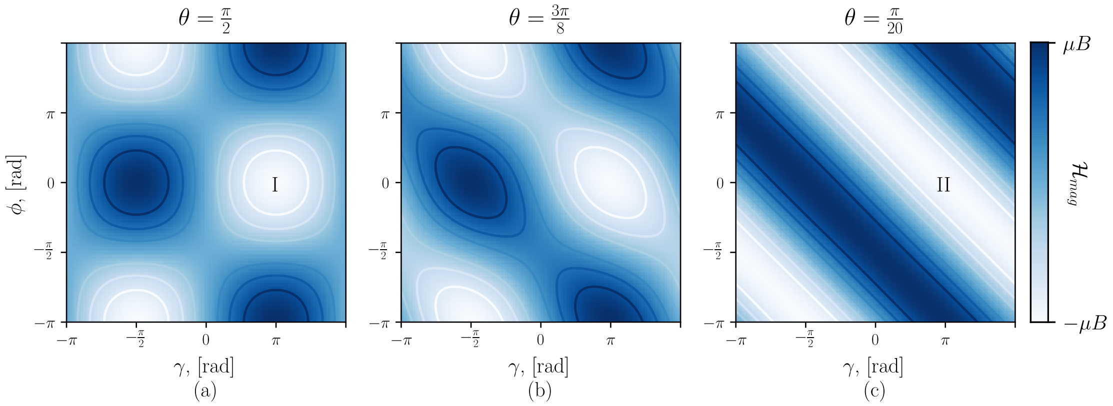

(a) (b) (c)

Figure 2.9: Slices in θ of the Hamiltonian $\mathcal{H}_{\text{mag}}(\phi, \theta, \gamma)$ for three polar angles $\theta \in \{\frac{\pi}{2}, \frac{3\pi}{8}, \frac{\pi}{20}\}$ shows the loss of a degree of freedom. When the rod is lying flat, ϕ and γ are independently constrained, but when vertical only the compound angle $(\phi + \gamma)$ is constrained. This results in the entropic favouring of vertical states compared to intermediate states despite the gravitational cost. Contours denote isopotentials. The lowest such contour encloses an area I, which undergoes a drastic expansion to the area II as the rod approaches vertical orientation.

where $\Delta\phi = \phi - \phi_0$, and similarly for $\Delta\gamma$.

When the rod is entirely vertical, the Hamiltonian suffers a loss of one degree of freedom: $\mathcal{H}(\theta, \phi, \gamma) \to \mathcal{H}(\theta, \phi + \gamma)$. This means that as the rod is continuously brought to the vertical position, even though the gravitational energy is increasing, a much larger region of phase-space suddenly becomes available to the rod due to the (ϕ, γ)-averaged magnetic energy. This can be seen in Fig. 2.9, where the contours represents isopotentials. As θ is brought to near-vertical, the area enclosed by the lowest isopotential undergoes a drastic expansion (I → II).

Hence, this system unambiguously exhibits a competition between the pure gravitational force $\boldsymbol{f}_{\text{gr}}(\theta)$, and the entropic magnetic force $\langle \boldsymbol{f}_{\text{mag}}(\phi, \gamma|\theta) \rangle_{\phi,\gamma,\theta}$. These forces have opposing directions, and this results in the emergence of two metastable states. The barrier that separates these states is defined by the minimum in $\ln p(\theta)$ which occurs when $\boldsymbol{f}_{\text{gr}}(\theta) = -\langle \boldsymbol{f}_{\text{mag}}(\phi, \gamma|\theta) \rangle_{\phi,\gamma,\theta}$.

---

[2] In discussing the rod orientation, we use term ‘force’ in the generalised sense, though of course these ‘forces’ are manifested mechanically as torques.

2.5 Conclusions

In this chapter we have applied techniques from equilibrium statistical mechanics to understand the observed hopping of a magnetic Janus-rod between horizontal and vertical orientations. While the vertical state comes at an energetic cost due to gravity, we have shown that it is entropically favoured. In thermally excited systems, fluctuations away from potential minima have a statistical importance; in the case of the rod, in the vertical configuration, a much larger region of phase-space is available to it due to a loss of degree of freedom in the potential energy.

In classical mechanics, this loss of one degree of freedom is associated with *gimbal lock*: a phenomenon where a mechanical instrument controlled by Euler-like rotations irreversibly loses a degree of freedom when two axes coincide [81]. Unlike this, however, the rod in our system is not controlled by Euler-angle rotations; rather it is controlled by frame-independent external forces which result from a potential energy which suffers the loss of one degree of freedom. While in mechanical systems, gimbal lock results in a reduction of control of the system, for a thermal system, an analogue of gimbal lock in the potential energy function results in an entropic gain of explorable phase space.

In order to develop our understanding of the entropic forces that govern the statistical behaviour of the rod, we considered a system $\{\boldsymbol{X}\} = \{(\boldsymbol{x}, \boldsymbol{y})\}$ in which a 'hidden' subsystem $\{\boldsymbol{y}\}$ interacts strongly with the subsystem of interest, $\{\boldsymbol{x}\}$. We showed that at a given $\boldsymbol{x}$, the observable subsystem experiences a real Hamiltonian force $\boldsymbol{f}_x = -\boldsymbol{\nabla}_{\boldsymbol{x}}\mathcal{H}_x(\boldsymbol{x})$ plus an entropic force $\langle -\boldsymbol{\nabla}_{\boldsymbol{x}}\mathcal{H}_{xy}(\boldsymbol{x}, \boldsymbol{y})\rangle_{y|x}$ due to an average over the subsystem interactions. This has a general applicability and produces nontrivial entropic forces in situations where the hidden variables are coupled to the observables in a nonlinear fashion, as in the case of the rotating rod.

3

Colloidal rods in rotating fields

So far in this thesis we have been considering equilibrium physics only, but from this chapter onwards the systems we will be studying will be driven out of equilibrium either externally or actively.

In the previous chapter we considered a microscopic ferromagnetic rod and its behaviour in a static external field. In this chapter we will look at how this rod behaves when driven out of equilibrium by a rotating magnetic field. Experimental observations show that as a function of driving frequency, the rod exhibits three distinct phases of behaviour. We explore the mechanical, thermal and hydrodynamic effects that are responsible for this behaviour both analytically and numerically.

3.1 Field-driven orientational phase

3.1.1 Experimental observations

The experiments described here were performed by Dr. Yongxiang Gao and Prof. Dirk Aarts using the same methods as described in the previous chapter except for the addition of a magnetic field rotating in the xy-plane of sedimentation: $\boldsymbol{B} = (B\cos\omega_B t, B\sin\omega_B t, 0)$. These experiments resemble previous work done by Dhar *et al.* (2007), and the qualitative results are the same. Three different steady-state behaviours are observed as a function of driving frequency ω_B:

1. $0 < \omega_B < \tilde{\omega}_1$: At low driving frequencies, the rod lies horizontally and rotates synchronously at a frequency $\omega = \omega_B$ in the xy-plane of the sedimentation.
2. $\tilde{\omega}_1 < \omega_B < \tilde{\omega}_2$: The rod stands vertically upright and rotates synchronously about its long axis at a frequency $\omega = \omega_B$.
3. $\tilde{\omega}_2 < \omega_B$: The rod lies flat in the plane again, but rotates asynchronously with an oscillating frequency $\omega(t)$ whose time-average is less than the driving frequency ω_B.

The first crossover happens smoothly across a range of frequencies around $\tilde{\omega}_1$, while the high-frequency transition occurs sharply. The critical frequencies $\tilde{\omega}_1$ and $\tilde{\omega}_2$ are also observed to be increasing functions of the magnetic interaction strength $|\mathcal{H}_{\mathrm{mag}}| \sim \mu B$. These experimental observations can be seen in the traces of projected length $L(t)$, shown in Fig. 3.1(a) for a rod with a magnetic moment $\mu = 2.1(1)\, k_B T\, \mathrm{G}^{-1}$, rotating in a field of strength $B = 50\,\mathrm{G}$. As in the previous chapter, the projected length of the rod is a measure of the degree to which it lies in the xy-plane. In this particular case we observe the time-averaged projection $\langle L(t) \rangle$ to cross over from L_{max} (horizontal) to L_{min} (vertical) at $\tilde{f}_{\mathrm{max}} \approx 0.5\,\mathrm{Hz}$, and then back to L_1 again at $\tilde{f}_2 \approx 15\,\mathrm{Hz}$. In experiments, the critical frequency is defined as the frequency at which $\langle L(t) \rangle_t = (L_{\mathrm{min}} + L_{\mathrm{max}})/2$. In Fig. 3.1(b) we can see the phase behaviour clearly as $\langle L(t) \rangle_t$ is plotted across the entire range of frequencies.

3.1.2 Mechanical theory

Qualitative explanation

The qualitative results in this experiment can be explained by classical mechanics alone, and such analyses has been given by Dhar *et al.* (2007), and Ghosh *et al.* (2013) who both use the equations of motion of the Euler angles to find the three steady-state regimes observed in experiments [80, 82]. A similar asynchronous decoupling has also been observed in different kinds of driven particles such as Quincke rotors [83–85]. In this section. we provide a simplified but insightful analysis that reproduces the qualitative phase behaviour.

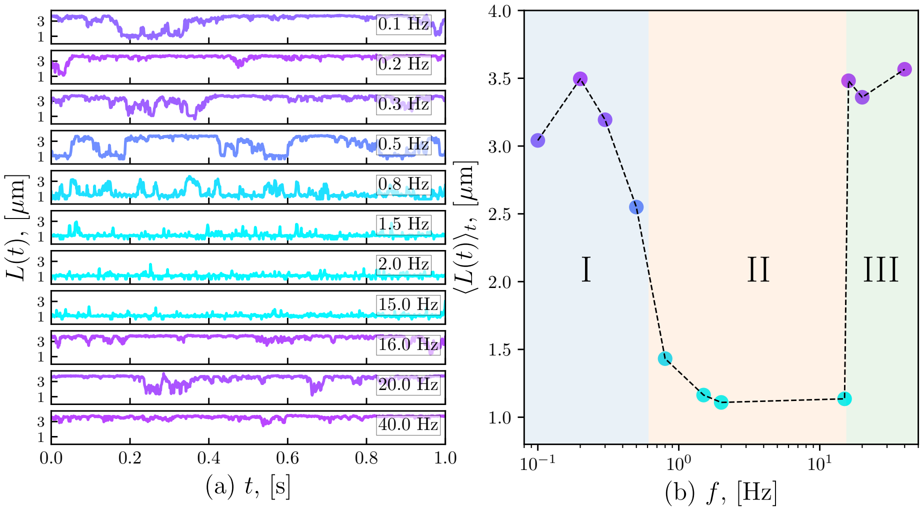

Figure 3.1: Rod orientation in a 50 G rotating field. (a) Traces of projected length $L(t)$ of a rod driven at different frequencies shows a crossover from high-$L(t)$ to low-$L(t)$ at low f, and a sharp transition back again at $\tilde{f}_2 \approx 15\,\text{Hz}$. Colours correspond to mean projected length across entire simulation, $\langle L(t)\rangle_t$. (b) $\langle L(t)\rangle_t$ for different frequencies shows this crossover and transition clearly. We define $\tilde{f}_1$ as the frequency at which $\langle L(t)\rangle = \frac{1}{2}(L_{\text{max}} + L_{\text{min}})$ and measure it to be $\tilde{f}_1 \approx 0.65$. The three phases separated by $\tilde{f}_1$ and $\tilde{f}_2$ are: I. horizontal–synchronous rotation; II. vertical–synchronous rotation; and III. horizontal–asynchronous rotation.

First, we consider the mechanical interaction between a rotating field $\boldsymbol{B}(t)$ and a sphere of radius r, with a rotational drag coefficient $\zeta = 8\pi\eta r^3$, and embedded magnetic moment $\boldsymbol{\mu}$. Neglecting noise, the equation of motion for this system in the overdamped limit is $\boldsymbol{\tau} = \zeta\boldsymbol{\omega}$. The torque is given by $\boldsymbol{\mu}\times\boldsymbol{B}(t)$, and in the steady state, the sphere will rotate along with the field, with some drag-induced lag, satisfying

$$\mu B \sin\alpha = \zeta\omega_B, \tag{3.1}$$

where α is the lag angle between the field and the sphere. It is clear that as ω_B is increased, α will also increase until $\sin\alpha$ reaches its maximal value of unity. At this point $\omega_B = \mu B/\zeta$ and any further increase in ω_B will destroy this steady state, leading to asynchronous behaviour.

In the present experiments, however, the anisotropy of the colloid results in there being two separate drag coefficients $\zeta_\perp$ ad $\zeta_\parallel$ corresponding to the two modes of rotation: about one of the colloid's short axes, or about its long axis respectively.

Because rotation about the long axis is ‘easier’ than rotation about the shorter axes, $\zeta_{\parallel} < \zeta_{\perp}$. Based on these considerations, the phase behaviour described in Sec. 3.1.1 may be explained qualitatively by the following:

1. $0 < \omega_B < \frac{\mu B}{\zeta_{\perp}}$: At low driving frequencies, gravity traps the rod in the xy-plane, until the viscous drag can no longer support the driving torque.
2. $\frac{\mu B}{\zeta_{\perp}} < \omega_B < \frac{\mu B}{\zeta_{\parallel}}$: The rod stands vertically upright in order to rotate about its easy axis, and does so until ω_B is too large to support any mode of rotation.
3. $\frac{\mu B}{\zeta_{\parallel}} < \omega_B$: The rod lies flat in the plane again due to gravity, but rotates asynchronously with the external field with an oscillating frequency $\langle \omega(t) \rangle_t < \omega_B$.

Thus we can identify the critical frequencies as $\tilde{\omega}_1(\mu B) = \frac{\mu B}{\zeta_{\perp}}$ and $\tilde{\omega}_2(\mu B) = \frac{\mu B}{\zeta_{\parallel}}$ which, as observed in experiment, are increasing functions of B.

Quantitative mismatch

So far this theory has qualitatively explained the observed experimental results, even though we have neglected interactions with the wall, and the effect of thermal noise. However, to make a quantitative comparison we must first estimate the friction coefficients $\zeta_{\perp}$ and $\zeta_{\parallel}$. There are two possible choices we can use: (1) the friction coefficients of an ellipsoid obtained exactly [12], or (2) the friction coefficients of a cylindrical rod using an asymptotic approach [86].

The results of these calculations are as follows (see Appendix B.1 for details):

Friction, [$k_{\mathrm{B}}T$ s]	Ellipsoid	Cylinder
$\zeta_{\perp}$	6.00(6)	9.1(1)
$\zeta_{\parallel}$	0.82(3)	1.35(4)

For this calculation, we have taken the full length of the rod to be $L = 3.5(1)$ µm and diameter $d = 0.65(3)$ µm to match the dimensions (and error) of the rod used in the experiment. The calculations show that the friction of the ellipsoid is smaller; this agrees with intuition since ellipsoids present a smaller profile, have a smaller surface area, and are smoother than cylinders of the same length.

Table 3.1: Lower and upper critical frequencies $\tilde{f}_{1,2}$ as predicted by the mechanical theory, $2\pi\tilde{f}_{1,2} = \mu B/\zeta_{\perp,\parallel}$, using ellipsoid (Ell.) and cylinder (Cyl.) friction coefficients, compared with experimentally obtained values (Exp.). All predictions are significant overestimates other than the underlined prediction which is a significant under-estimate.

	50 G			100 G			150 G		
	Ell.	Cyl.	Exp.	Ell.	Cyl.	Exp.	Ell.	Cyl.	Exp.
$\tilde{f}_1$	2.4(2)	1.6(1)	0.65(5)	4.9(4)	3.2(3)	1.7(2)	7.3(6)	4.8(4)	2.2(2)
$\tilde{f}_2$	19(2)	$\underline{12(1)}$	15.5(5)	39(4)	24(3)	20.5(5)	58(7)	35(4)	24.5(5)

We use these calculated friction coefficients to find the predicted critical frequencies $\tilde{f}_{1,2} = \tilde{\omega}_{1,2}/2\pi$ and compare them with the experimental observations. The rod used in the experiments was measured to have a magnetic moment strength $\mu = 2.1(1)\, k_B T\, \mathrm{G}^{-1}$, and it was tested for a range of frequencies at three field strengths, $B = \{50, 100, 150\}$G. Using these values, we get the predictions for the lower and upper critical frequencies shown in Table 3.1, along with the experimentally observed frequencies.

With the exception of one point (underlined), the predictions from the mechanical theory significantly overestimate the critical frequencies. We also note that while the mechanical theory predicts a linear relationship between $\tilde{f}$ and B, the experimentally observed $\tilde{f}_2(B)$ values exhibit a nonlinear relationship [This is better seen in Fig. 3.2(b)]. Additionally, the experiments show a smooth crossover between phases I-II, and a sharp transition between phases II-III, which our mechanical theory fails to distinguish between.

These discrepancies must have one of three sources: (1) Neither the ellipsoidal nor the cylindrical friction coefficients are correct in describing the friction of the cylindrospherical rod in the experiments; (2) The friction coefficients do not take into account any hydrodynamic interactions with the wall; (3) Thermal fluctuations might have some role, as we saw for the magnetic rod in the previous chapter.

The first possible cause (1) may be disqualified on the basis that the rod's cylindrospherical shape means that its friction should be *less* than that of a cylinder due to its rounded ends (which make it both smoother, and reduce its total surface area). Lower friction should in turn mean higher critical frequencies $\tilde{f}_{1,2}$ which would drive the discrepancy in the opposite direction. In particular, there appears to be a nonlinear relationship between $\tilde{f}$ and B, so no constant friction coefficient can explain this discrepancy.

3.2 Brownian dynamics simuations

3.2.1 Methods

In order to test the effect that thermal noise has on the system, we designed Brownian dynamics (BD) simulations to see if statistical fluctuations alone can be responsible for the discrepancy observed in the previous section. In this model, a horizontal plane is present but only interacts sterically with the rod. Thus, these simulations are designed to study only the effect of noise, not hydrodynamic interactions. In this section, we will be discussing both the magnetic moment of the rod, and the rod's mobility tensor (the inverse of its friction tensor). As before, we will denote the mobility as $\boldsymbol{\upmu}$, and the magnetic moment as $\boldsymbol{\mu}$.

As stated in Sec. 1.4.2, when the mobility tensor of a particle depends on its current state, the stochastic differential equation (SDE) that describes its dynamics is most faithfully interpreted using the Stratonovich convention. This results in a mobility-dependent drift term entering the SDE as shown in Eq. (1.37). As the full state of the rotating rod is defined by $(\hat{\boldsymbol{n}}, \boldsymbol{\mu})$, and the rotational mobility of the rod $\boldsymbol{\upmu}^{r}$, depends on $\hat{\boldsymbol{n}}$,

$$\boldsymbol{\upmu}^{\mathrm{r}}(\hat{\boldsymbol{n}}) = \upmu^{\mathrm{r}}_{\parallel}\hat{\boldsymbol{n}}\hat{\boldsymbol{n}} + \upmu^{\mathrm{r}}_{\perp}(\mathbf{I} - \hat{\boldsymbol{n}}\hat{\boldsymbol{n}}), \tag{3.2}$$

a proper treatment of this drift term is required.

An added complication is the integration of rotational motion, which constrains the dynamics, as $|\hat{\boldsymbol{n}}| = 1$, $|\boldsymbol{\mu}| = \mu$ and $\boldsymbol{\mu}\cdot\hat{\boldsymbol{n}}$ must be maintained throughout — under rotation, a pair of vectors must maintain their length, and relative orientations. It is possible to formulate the equations of motion in terms of the rotation matrices or Euler angles introduced in the previous chapter. However, while these descriptions worked well in describing static quantities such as the rod Hamiltonian or pdf, they work less well in describing rotational dynamics due to the phenomenon of gimbal lock which happens when two axes of rotation coincide and the system loses a degree of freedom.

In this section we therefore follow the prescription of Delong *et al.* (2015) who describe a Brownian dynamics method using *quaternion* integration [87]. In this formulation, the orientational state of the particle is described by the normalised unit quaternion. A quaternion is a 4-component vector consisting of a scalar and 3-vector: $\boldsymbol{\theta} = (s, \boldsymbol{p})$ along with a normalisation condition, $||\boldsymbol{\theta}||^2 = s^2 + \boldsymbol{p} \cdot \boldsymbol{p} = 1$. Quaternion multiplication is denoted by $\boldsymbol{\theta}_3 = \boldsymbol{\theta}_1 \boldsymbol{\theta}_2$ and defined as:

$$\begin{bmatrix} s_3 \\ \boldsymbol{p}_3 \end{bmatrix} := \begin{bmatrix} s_1 s_2 - \boldsymbol{p}_1 \cdot \boldsymbol{p}_2 \\ s_1 \boldsymbol{p}_2 + s_2 \boldsymbol{p}_1 + \boldsymbol{p}_1 \times \boldsymbol{p}_2 \end{bmatrix}. \tag{3.3}$$

This definition for multiplication forms a group with identity element $(1, \mathbf{0})$, and an inverse for each element $\boldsymbol{\theta} = (s, \boldsymbol{p})$ defined by $\boldsymbol{\theta}^{-1} = (s, -\boldsymbol{p})$. Any rigid-body orientation can be represented by an axis $\hat{\boldsymbol{n}}$, and an an angle γ indicating a rotation about that axis. We can associate these with the quaternion:

$$\boldsymbol{\theta}_{\boldsymbol{n},\gamma} = (\cos(\gamma/2), \sin(\gamma/2)\hat{\boldsymbol{n}}) \tag{3.4}$$

Using this definition, it can be shown that the quaternion multiplication [Eq. (3.3)] represents successive rotations.

To transform from a 3-vector description of angular velocity, to the quaternion angular velocity requires a 4 × 3 matrix, $\boldsymbol{\Psi}$,

$$\dot{\boldsymbol{\theta}} = \boldsymbol{\Psi}\boldsymbol{\omega}, \tag{3.5}$$

$$\boldsymbol{\Psi} = \begin{bmatrix} -\boldsymbol{p}^T \\ s\boldsymbol{I} - \mathbf{P} \end{bmatrix}, \tag{3.6}$$

where $\mathbf{P}$ is defined by $\mathbf{P}\boldsymbol{r} = \boldsymbol{p} \times \boldsymbol{r}$. This matrix also has the property that evolution under Eq. (3.5) satisfies the constraint that $||\boldsymbol{\theta}||^2 = 1$ is kept constant.[1]

The Itô SDE for rotational diffusion of a quaternion becomes

$$\mathrm{d}\boldsymbol{\theta} = (-\tilde{\boldsymbol{\mu}}^r \nabla_\theta \mathcal{H} + k_\mathrm{B} T \nabla_\theta \cdot \tilde{\boldsymbol{\mu}}^r)\,\mathrm{d}t + \sqrt{2 k_\mathrm{B} T}\ \tilde{\mathbf{b}}^r\ \mathrm{d}\boldsymbol{w}^r, \tag{3.7}$$

---

[1] Proof: $\frac{1}{2}\frac{\mathrm{d}}{\mathrm{d}t}\boldsymbol{\theta}^T\boldsymbol{\theta} = \boldsymbol{\theta}^T\dot{\boldsymbol{\theta}} = \boldsymbol{\theta}^T\boldsymbol{\Psi}\boldsymbol{\omega} = \boldsymbol{\Psi}^T\boldsymbol{\theta}\boldsymbol{\omega} = (-s\boldsymbol{p} + s\boldsymbol{p} + \boldsymbol{p} \times \boldsymbol{p})\boldsymbol{\omega} = \mathbf{0}\,\square$.

where $\tilde{\boldsymbol{\upmu}}^r = \boldsymbol{\Psi}\boldsymbol{\upmu}^{\mathrm{r}}\boldsymbol{\Psi}^T$, and $\tilde{\mathbf{b}}^r(\tilde{\mathbf{b}}^r)^T = \tilde{\boldsymbol{\upmu}}^r$. We also solve for the translational Brownian motion of the particle's centre of mass, $\boldsymbol{r}$, using a standard Itô SDE

$$\mathrm{d}\boldsymbol{r} = \boldsymbol{\upmu}^{\mathrm{t}}\boldsymbol{f}\mathrm{d}t + \sqrt{2k_{\mathrm{B}}T}\mathbf{b}^t\mathrm{d}\boldsymbol{w}^t, \tag{3.8}$$

where $\boldsymbol{\upmu}^{\mathrm{t}}$ is the translational mobility tensor, $\mathbf{b}^r$ its decomposition, and $\boldsymbol{w}^r$ the translational noise on the particle.

In our BD simulation, we integrate these equations using Fixman's midpoint scheme (see Appendix B.2 for details) [87, 88]. The simulation is initialised with the starting orientations of the rod, and its magnetic moment, $(\hat{\boldsymbol{n}}_0, \boldsymbol{\mu}_0)$. We compute the magnetic torque acting on the particle at a time t using the rotation matrix generated by the quaternion: $\tau_B = (\mathbf{R}[\boldsymbol{\theta}_t]\boldsymbol{\mu}_0) \times \boldsymbol{B}(t)$, with

$$\mathbf{R}[\boldsymbol{\theta}_t] = 2\left[\boldsymbol{p}\boldsymbol{p}^T + s\mathbf{P} + \left(s - \frac{1}{2}\right)\mathbf{I}\right]. \tag{3.9}$$

We account for a wall (defined by the $z = 0$ plane) using a soft potential which applies a force $\boldsymbol{f}$ on the rod proportional to its overlap, $(-)\delta h$. If r_z is the centre-of-mass coordinate of the rod, then $\delta h = r_z - (l\cos\theta + d)/2$ as in Fig. 2.5(b). The repulsive force is due to a one-sided harmonic potential with a strength $k_{\text{wall}} = 100\, k_B T\, \upmu\mathrm{m}^{-1}$:

$$\mathcal{H}_{\text{wall}}(\delta h) = \begin{cases} 0, & \text{for } \delta h \geq 0, \\ \frac{1}{2}k_{\text{wall}}\delta h^2, & \text{otherwise.} \end{cases} \tag{3.10}$$

This results in a contact force normal to the plane, $\boldsymbol{f}_{\text{wall}} = f_{\text{wall}}\hat{\boldsymbol{z}}$, and in general produces a moment on the rod, $\boldsymbol{r}_c \times \boldsymbol{f}_{\text{wall}}$, where $\boldsymbol{r}_c$ is the contact point relative to the rod centre-of-mass. We approximate the contact point as being on the lower of the two ends of the rod, $\boldsymbol{r}_c \approx -\frac{1}{2}\mathrm{sgn}(n_z)(l + d)\hat{\boldsymbol{n}}$. The gravitational force on the particle $\boldsymbol{f}_{\text{grav}} = -gm^*\hat{\boldsymbol{z}}$, together with the steric torque applied by the wall work together to keep the particle 'sedimented' horizontally on the plane.

We use the mobility tensor for a cylinder, $\upmu^{\mathrm{r}}_{\perp} = \zeta_{\perp}^{-1}$, $\upmu^{\mathrm{r}}_{\parallel} = \zeta_{\parallel}^{-1}$ because, as we saw in the previous section, using the cylinder friction coefficients gives a closer approximation to the experimental data.

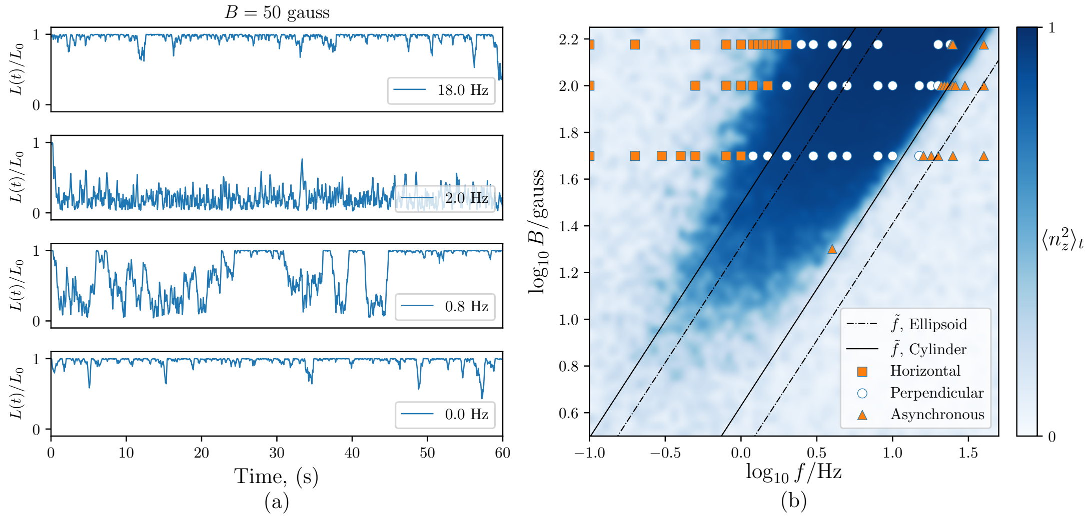

Figure 3.2: (a) Traces of projected length $L(t)$ of $\hat{\boldsymbol{n}}$ in a Brownian dynamics simulation with a 50 G field rotating at different frequencies. (b) Heatmap: Mean-square perpendicular component of rod orientation $\langle n_z^2 \rangle_t$ for simulations across a range of magnetic field B, and frequency, f. Points: Experimentally obtained data showing steady state phase of the rod (□: synchronous–horizontal; ○ synchronous–perpendicular; △, asynchronous–horizontal) for experiments conducted at different fields and frequencies. Lines: Predicted lower and upper critical frequencies $\tilde{f}_{1,2}$ using simple mechanical theory with the friction coefficients for an ellipsoid (solid line), and a cylinder (dashed–dotted line).

3.2.2 Results

From our simulations we can generate similar data as that obtained by experiments. In particular, we are able to observe traces of the rod's projected length $L(t) = \sqrt{n_x(t)^2 + n_y(t)^2}$, similar to Figs. 3.1 and 2.3, with the exception that this projection does not account for the diameter, hence $L_{\text{min}} = 0$. Four such traces are shown in Fig. 3.2(a) for a rod in a $B = 50\,\text{G}$ field rotating at different frequencies. The same qualitative behaviour is observed: when $L(t)$ remains low for the entire simulation (e.g., in the $f_B = 2\,\text{Hz}$ trace), this signifies that the rod is rotating at a near-vertical orientation.

Performing fast simulations of this type enables us to map out the entire phase-space over (f, B). In Fig. 3.2(b) we plot a heatmap of the mean-square perpendicular orientation $\langle n_z^2 \rangle_t$ across a range of driving frequencies, and external fields. The dark region in the figure corresponds to the region of parameter-space where the rod tends to align vertically in the steady state. At lower magnetic fields, the vertical

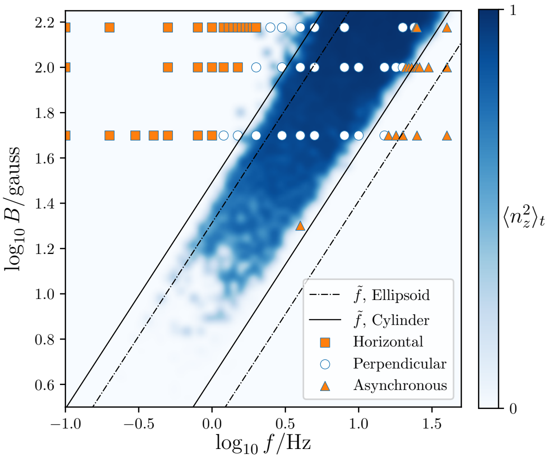

(b)

Figure 3.3: Same as Fig. 3.2(b), except simulations were conducted at $k_\mathrm{B}T = 0.01$. At large enough magnetic fields compared to those used in experiments, the phase boundaries are predicted very well by the mechanical theory in Sec. 3.1.2.

phase disappears, as the magnetic field interaction becomes insufficient to overcome the gravitational potential that keeps the rod flat.

The experimental data (square, circular and triangular points) are overlaid on Fig. 3.2(b), along with the curves $\tilde{f}_{1,2} = \mu B/\zeta_{\perp,\|}^{\text{ell.,cyl.}}$ obtained from the mechanical theory. In comparing these to the results of the simulation, we make two key observations.

Firstly, the left-boundary of the dark region (which gives the lower critical frequency $\tilde{f}_1$) matches the experimental $\tilde{f}_1$ very well, capturing the nonlinear relationship between $\tilde{f}$ and B. We see that the crossover from horizontal to vertical is similar to the experiments in its smoothness. This suggests that thermal noise could have a role to play in this critical regime. Our second main observation is that the right-boundary of the vertical phase (corresponding to $\tilde{f}_2$), matches the mechanical theory, and *not* the experimental results.

3.3 Discussion

3.3.1 Lower critical frequency: thermal effects

Increasing the driving frequency, f_B, pushes the system further and further away from equilibrium. At small frequencies, however, it is reasonable to suggest that some of the physics that we observed in the previous chapter might carry over. In particular, the fact that we observe the rod to robustly occupy the vertical state at frequencies lower than classical mechanics predicts hints that this might be the case.

If it is purely thermal effects that are responsible for this, then we expect that turning the noise down in our simulations should lead to the depopulation of these mechanically ‘forbidden’ states. We reran the set of simulations shown in Fig. 3.2(b) except with $k_{\mathrm{B}}T = 0.01$, allowing a small amount of noise in order to avoid mechanically unstable steady states.

The results are shown in Fig. 3.3. Clearly, for sufficient magnetic field strength, neglecting noise results in mechanical behaviour that is very well predicted by the theory developed in Sec. 3.1.2. Therefore, we conclude that the discrepancy between this theory and experiments is due to the effects of noise.

3.3.2 Upper critical frequency: hydrodynamic effects?

In Sec. 3.1.2, we identified the two most plausible sources of discrepancy between the experiments and theory: the effects of noise, and the effects of hydrodynamic interactions with the plane. We have shown that the presence of noise shifts the lower critical frequency downward in a manner that is consistent with experiments; however it does not alter the upper critical frequency.

We therefore hypothesise that it is hydrodynamic interactions with the wall which result in the nonlinear relationship between $\tilde{f}_2$ and B. In theory it should be possible to test this using a Brownian dynamics approach similar to that described above, except with the mobility tensor for a cylinder near a wall, $\boldsymbol{\mu}_w = \mu_{w,\parallel}\hat{\boldsymbol{n}}\hat{\boldsymbol{n}} + \mu_{w,\perp}(\mathbf{I} - \hat{\boldsymbol{n}}\hat{\boldsymbol{n}})$. However, unlike the mobility tensor used in this chapter, the components $\mu_{w,\{\perp,\parallel\}}$ are themselves functions of the rod’s orientation and position relative to the plane, (n_z, r_z). Moreover, hydrodynamic interactions result in a coupling between the translational motion of the ellipsoid and its rotation that complicates the situation further.

Nevertheless, work has been done by de Corato *et al.* (2015) using a finite element procedure to map out the full mobility tensor coefficients (including the coupling) in order to use these as an input in a Brownian dynamics solver [89]. Lisicki *et al.* (2016) showed that analytic progress is possible by calculating the corrections to the bulk mobility tensor for a spheroid near a wall [90]. While this work, in theory, is applicable to our problem, the fact that our rods are in close contact with the wall at all times poses a difficulty: close to the wall, the mobilities vanish due to diverging friction coefficients, making integration of Eq. (3.7) difficult.

However a possible hydrodynamic mechanism for the nonlinearity in $\tilde{f}_2(B)$ is as follows. In the previous chapter we described how the true orientation of the embedded magnetic moment was slightly off-perpendicular, such that $\hat{\boldsymbol{n}} \cdot \boldsymbol{\mu} = \sin \epsilon$, with a small offset angle $\epsilon \approx \mathcal{O}(1^\circ)$. This would mean that rotation in the vertical phase would actually occur about some axis offset from $\hat{\boldsymbol{n}}$, i.e., the rod would appear to precess, and as it did so such nonaxisymmetric rotation could cause its height δh to be a function of the rotational frequency via the rotational-translational coupling that occurs due to the interactions with the plane. As Lisicki *et al.* show [90], the first order correction to the bulk rotational friction coefficient is $\zeta = \zeta_{\text{bulk}} + 1/(\delta h)^3 \zeta_{\text{corr}}$, this would imply a height dependence entering into the critical frequency:

$$2\pi \tilde{f}_2 = \frac{\mu B}{\zeta_{\text{bulk}} + \frac{1}{\delta h(\tilde{f}_2)^3} \zeta_{\text{corr}}}, \tag{3.11}$$

in which the height itself, being a function of frequency, gives rise to a nonlinearity. To test this, we calculated the first-order corrections to the translational–rotational coupling tensor given by Lisicki *et al.* for a rod precessing with an angle ϵ, but found that this did not result in any vertical translation. Therefore, if hydrodynamic effects are responsible for the discrepancy observed in $\tilde{f}_2$ via the mechanism outlined above, this must come from higher-order corrections to the friction tensor.

3.4 Conclusions

In this chapter we have attempted to interpret the phase behaviour of an externally driven magnetic rod via three competing physical factors. We first showed that the three observed phases could be explained qualitatively by a simple classical mechanical theory of an axisymmetric particle rotating in a viscous medium.

However, when we tried to compare this theory quantitatively with the data we found that the two critical transition frequencies $\tilde{f}_{1,2}$ did not agree between theory and experiment.

We hypothesised that either thermal effects or hydrodynamic effects could account for this discrepancy, and to explore this possibility we conducted Brownian dynamics simulations of the system to understand the role of noise. We found that thermal fluctuations were able to explain the shifting of the lower transition frequency $\tilde{f}_1$, concluding that, in a similar vein to Chapter 2, thermal fluctuations favour the vertical orientation despite its gravitational cost. In the previous chapter, this was due to the entropic benefit of the vertical orientation, and here, as the system is out of equilibrium we hypothesise that it is the minimisation of *entropy production* that stabilises this vertical state.

For the upper critical frequency, $\tilde{f}_2$, the Brownian dynamics failed to explain the discrepancy which suggests that noise is not the responsible factor. We conclude that it is possible that hydrodynamic interactions are the cause, and provide a hypothetical mechanism by which interactions with the horizontal wall are able to introduce a nonlinearity in $\tilde{f}(B)$. However with our existing numerical and analytical machinery [89, 90], we were unable to quantitatively verify this.

4

Hydrodynamics of a helical flagellum

Over the next three chapters, we turn our attention to biophysics as we ask: How is the swimming of a flagellated microorganism affected by the presence of large polymers in its surrounding medium? This question has been asked in various ways over recent years as a part of an ongoing effort to better understand the behaviour of motile cells in biologically relevant fluids; however a complete answer has yet remained elusive [91, 92].

The focus of the following chapters will be on viscoelasticity, which is where the response of the environment in general comprises of two parts: a viscous response and an elastic response [13]. While much previous effort has been poured into understanding swimming in *continuum* viscoelastic media [93], we will be working in a very different regime in which our active 'swimmer' experiences the effect of a single nearby polymer in an otherwise Newtonian viscous fluid. Here, our specific aim is to understand the interaction between a helical flagellum and a polymer, and demonstrate that this approach can shed new light on the question of swimming through dilute polymer suspensions.

In this chapter we develop a simulation model for an externally-actuated rigid helix and demonstrate that it faithfully reproduces the hydrodynamic properties which we expect. We will achieve this in two ways, first by matching the roto-translational mobility matrix we obtain to that predicted by slender body theory, and secondly by comparing the flow fields generated by our simulation to experiments on a macroscopic rigid helix.

In the next chapter, we will assess our minimal model's candidacy as a proxy for the biological system of interest — a cell with a helical flagellum — by comparing these hydrodynamic results to a more biologically faithful model simulated using multiparticle collision dynamics (MPCD). Then, we will study the polymer–helix interaction for the cases of a stationary rotating 'pump', and, in Chapter 6, a freely swimming helix.

4.1 Background

While the physics of swimming microbes in Newtonian viscous fluids has been well characterised, attention has recently turned towards understanding how active microorganisms behave in more biologically relevant media where the presence of large biopolymers, elastic filaments, or exopolymer secretions can dictate dynamics. In such complex fluids, motility enhancement [94], as well as retardation [95–97], have both been reported in various experimental and theoretical studies.

Experiments by Shen and Arratia (2011) have shown that in dilute polymer solutions, the undulatory swimmer *C. elegans* is hindered by elasticity; the authors claim that this hindrance is due to the stretching of polymers at hyperbolic points of the flow field generated by the organism [98]. However, in a later experiment (2013) the same authors showed that the motility of *C. elegans* is *enhanced* in a dense solution of rodlike polymers, due to the anisotropic mechanical response of the medium which forms a network [99]. Theoretical investigations for undulatory swimming have also been performed. Lauga (2007) has shown by asymptotic calculations that a small-amplitude waving sheet is hindered by elasticity [100], while Teran, Fauci and Shelley (2010) have performed a numerical analysis of a large-amplitude sheet showing enhancement instead [101]. More recently, Thomases and Guy (2014) have shown both enhancement and hindrance as a function of the swimming beat, reproducing both results [102].

Experimental work on helical swimmers in viscoelastic media has been developed since the 1970s [103, 104] and similar effects on motility have been observed. Liu, Powers and Breuer (2011) have performed macroscopic experiments on a scaled-up model of a helical flagellum [105]. In their experiment, a helical wire is rotated at various rates and they find an enhancement of swimming speed occurs when the rotation rate balances the relaxation rate of the polymers (reaching a peak at Deborah number $\mathrm{De} \approx 1$), but at higher rates (around $\mathrm{De} \approx 2$), its locomotion begins to be hindered. Spagnolie, Liu and Powers (2013) later showed numerically that this basic dependence on Deborah number is also very geometry-dependent: for small helical radii the motility is hindered as predicted by small-amplitude theoretical calculations [106].

Biological helical swimmers exhibit an even richer phenomenology due in part to their greater mechanical complexity (e.g., for *E. coli*, a bundle of flagella and a counter-rotating body), as well as their biochemisty. For example, the swimming of the ulcer-causing bacteria, *H. pylori*, through gastric mucus *in vivo* is highly controlled by its release of ammonia which de-gels the surrounding mucus allowing it to swim through a fluid pocket [107]. Martinez *et al.* (2014) have performed experiments on *E. coli* which exhibit non-Newtonian motility enhancement in native polyvinylpyrrolidone (PVP) solutions compared to dialyzed PVP solutions, suggesting that potential carbon-source impurities may lead to a metabolic speed increase in an otherwise Newtonian fluid [108]. Similar experiments by Patteson *et al.* (2015) have shown that the swimming trajectories of *E. coli* are drastically altered in two ways by viscoelastic solutions: the tumbling rates of the swimming bacteria are greatly reduced and the ballistic paths they follow are straighter [109]. They attribute the first effect to the increased viscosity of polymer solutions, claiming that greater viscosity results in a higher load on the bacterial flagellar motor, decreasing its tumble rate in line with previous experimental evidence [24]. The underlying mechanism for this kind of mechanosensing is biochemical in nature; the switching rate of the motor is controlled by binding of the Che-Y protein [110], and the rate at which it binds is modulated by torque acting on the motor. The straightening of the bacterial trajectories they ascribe to a hypothesis that elastic stresses stabilise the cell's tendency to wobble.

For completeness we note that much work has been done to try to understand the mechanics of flexible flagellar filaments [111–113] which add another source of elasticity to the problem and raise extra questions of mechanical stability, energy transfer, and propulsion speed. While studying elastic filaments is important for understanding certain types of motile cells such as sperm, we do not address the question of flagellar flexibility in this thesis so we will omit a full discussion here.

Broadly speaking, theoretical studies exploring swimming in viscoelastic media yield model- or parameter-dependent results [94, 102, 106]. Invariably, these studies concentrate on continuum models of viscoelasticity, and as such cannot provide a full insight into the specific microscopic mechanisms of interaction between single polymers and the flagella of the swimmers. While continuum theory might apply well to an organism such as *C. elegans* with a typical length of 1 mm, it is not so obvious that it applies equally well on the length scale of an *E. coli* flagellum which has a filament diameter of 20 nm.

Swimming dynamics may indeed be affected by individual polymer–cell interactions due to similar timescales of cells and biopolymeric material *in vivo*. From the experimental work that we have reviewed here, a number of such hypotheses are made, and cannot be tackled by continuum theory. One hypothesis, posed by Martinez *et al.* is that for an *E. coli* in a dilute polymer solution, a timescale separation between the fast rotation of the bacterial flagellum and slow relaxation of the polymers effectively depletes the flagellum's local environment of polymeric material as it clears its surrounding volume. Hence, the flagellum experiences an effective viscosity that can be markedly different from that perceived by the more slowly counter-rotating cell body [108]. However, the microscopic assumptions underlying this hypothesis require more concrete justification as it is not apparent that such a depletion might occur. Another hypothesis, claimed by Patteson *et al.*, posits that the curved streamlines that wind around the helical flagellum result in shear flow which may stretch out individual polymers [109]. The collective result of elongated polymers curving around the cell is an elastic stress which stabilises — hence speeding up — the cell's swimming. The authors recognise that their hypothesis *"is contingent on the expectation that swimming* E. coli *cells can actually generate flow fields strong enough to stretch polymer molecules"* and so this raises the question of how large biopolymers interact with actively actuated filaments such as flagella on the single-polymer level.

Additionally, there are separate phenomena in which the interactions between large polymers and active microorganisms are important but have yet to be studied on the microscopic level. For instance, various microbes have long been known to enhance filter-feeding by employing their flagella or cilia to generate feeding currents that carry detritus and nutrients toward the cell body [114]. While motile bacteria swim force-free [8, 115], these immobile microbes tether themselves in order to exert nonnegligible net forces on the surrounding medium [116, 117]. Aggregations of such cells can collectively produce millimeter-scale fluid flows to actively combat variations in the nutrient concentrations [118].

While the hydrodynamic attraction of small nutrients has been considered [119] the interaction of macromolecular polymers with immobile flagellates has yet to be explored in detail. A question that remains open is whether the filter-feeding of large polymers progresses similarly to small tracer particles or, as with swimming, whether the dynamics of individual polymers enhances or reduces a tethered cell's ability to draw in polymeric material towards it.

Over the next three chapters, we will explore how macromolecular biopolymers hydrodynamically interact with an active helical filament (either pinned or swimming) actuated by external torques and forces. The remainder of this chapter will be dedicated to developing our simulation model and demonstrating that it reproduces well established results for flagellar hydrodynamics.

4.2 Computational model

4.2.1 Equation of motion

We wish to study the stochastic dynamics of a polymer in the vicinity of a hydrodynamically active helical filament, a setup shown in Fig. 4.1. Stokesian dynamics (SD) is a natural technique to probe such a system that does not involve explicitly simulating a solvent or solving continuum hydrodynamic equations. In Sec. 1.4.2 we introduced a general stochastic differential equation for a system of particles with positions $\boldsymbol{r}$, acted on by deterministic forces $\boldsymbol{f}$, and Brownian noise increments $\mathbf{b}\ \mathrm{d}\boldsymbol{w}$:

$$\begin{aligned} \mathrm{d}\boldsymbol{r} &= \left[\boldsymbol{\mu}\boldsymbol{f} + \frac{1}{2}\mathbf{b}\nabla\cdot\mathbf{b}\right]\mathrm{d}t + \mathbf{b}\ \mathrm{d}\boldsymbol{w}, && (4.1)\\ \langle \mathbf{b}^T\mathbf{b}\rangle &= 2k_{\mathrm{B}}T\boldsymbol{\mu}\ \delta(t-t'). && (4.2) \end{aligned}$$

Complex objects can be constructed out of particles by specifying the forces $\boldsymbol{f}$ that keep them together. For instance, $\boldsymbol{f}$ can represent mutually attractive forces due to bonding potentials, repulsive forces due to effective exclusion potentials — i.e., 'soft-sphere' interactions — and generically prescribed external forces that actuate motion in the system. How polymers and helical filaments can be constructed in this way will be discussed in the next section.

Long-range hydrodynamic interactions may be taken into account through a correct treatment of the mobility tensor $\boldsymbol{\mu}$, which in general will depend on all the particle positions $\boldsymbol{r}(t)$, and will change with time. To understand how this works, consider two particles with positions $\boldsymbol{r}_a$, and $\boldsymbol{r}_b$. If a force $\boldsymbol{f}_a$ is applied to particle a, we know that this will create a flow field given by Eq. (1.7). In the absence of forces $\boldsymbol{f}_b$, particle b must be advected with this flow field. Therefore, considering the low-noise limit (in which also $\mathbf{b} \sim \sqrt{k_{\mathrm{B}}T} \to 0$), Eq. (4.1) must give to lowest order:

$$\frac{\mathrm{d}\boldsymbol{r}_b}{\mathrm{d}t} = \mathbf{G}(\boldsymbol{r}_b - \boldsymbol{r}_a)\boldsymbol{f}_a. \tag{4.3}$$

It is therefore tempting to use the Oseen tensor $\mathbf{G}$ [as defined in Eq. (1.8)] for the mobility $\boldsymbol{\mu}$. However this poses a problem for computing $\mathbf{b}$ as the Oseen

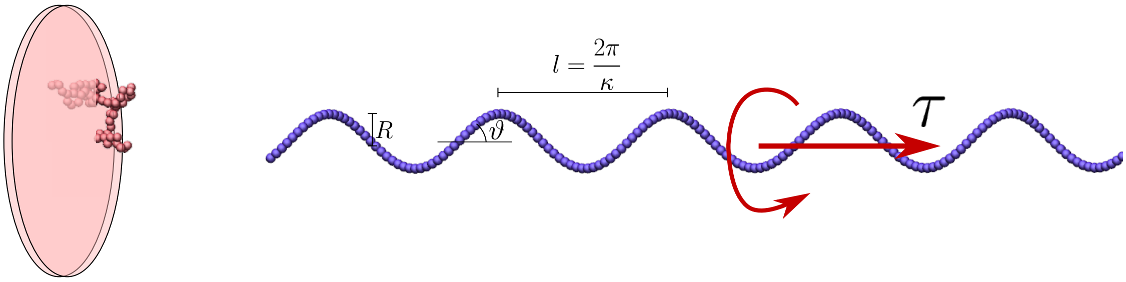

Figure 4.1: Our system of interest comprises a helical filament, and a nearby polymer. As an external torque acts on the helix, it rotates. We want to understand how its rotation hydrodynamically interacts with the polymer in two cases: (1) when the helix is pinned and pumps fluid along the direction shown, and (2) when the helix is free, and swims towards the polymer. To describe the geometry of the helix, we use the radius R and the pitch l which measures the 'wavelength' of the helix. Where it is more convenient to use the 'wavenumber' κ, or pitch angle ϑ, we do so interchangeably. Polymers are initialised in a random location on a disc some distance 'upstream' of the helix (not to scale in image).

tensor is not guaranteed to be positive-definite at short distances, and so factoring it into $\mathbf{G} = \mathbf{b}^T\mathbf{b}$ is not always possible if we insist that $\mathbf{b}$ must be real.[1] A solution to this was proposed by Rotne and Prager (1969), and independently by Yamakawa (1970). This involved regularising the Oseen tensor to account for finite-volume effects in the two-particle interaction [120, 121]. The result is the Rotne–Prager–Yamakawa (RPY) tensor:

$$\frac{\boldsymbol{\mu}_{ij}}{\mu_0} = \begin{cases} \frac{3a}{4r_{ij}}(\mathbf{I} + \hat{\boldsymbol{r}}_{ij}\hat{\boldsymbol{r}}_{ij}) + \frac{a^3}{2r_{ij}^3}(\mathbf{I} - 3\hat{\boldsymbol{r}}_{ij}\hat{\boldsymbol{r}}_{ij}), & \text{for } r_{ij} \geq 2a, \\ \left(1 - \frac{9r_{ij}}{32a}\right)\mathbf{I} + \frac{3}{32}\frac{r_{ij}}{a}\hat{\boldsymbol{r}}_{ij}\hat{\boldsymbol{r}}_{ij}, & \text{otherwise,} \end{cases} \tag{4.4}$$

where $\boldsymbol{r}_{ij} = \boldsymbol{r}_j - \boldsymbol{r}_i$, $|\boldsymbol{r}_{ij}| = r_{ij}$, and $\hat{\boldsymbol{r}}_{ij} = \boldsymbol{r}_{ij}/r_{ij}$. The particle radius is a, and $\mu_0 = 1/6\pi\eta a$ is the Stokes mobility of a sphere with radius a immersed in a fluid with viscosity η.

The RPY tensor has the property that $\boldsymbol{\nabla} \cdot \boldsymbol{\mu}_{ij} = \mathbf{0}$, which results in the drift term in Eq. (4.1) vanishing as $\boldsymbol{\nabla} \cdot (\boldsymbol{b}^T\boldsymbol{b}) \propto \mathbf{b}^T\boldsymbol{\nabla} \cdot \mathbf{b} = 0$. For a 3-dimensional system of N particles, Eqs. (4.1) can be rewritten as a matrix–vector difference equation involving timestep Δt:

$$\Delta\boldsymbol{r} = \boldsymbol{\mu}\boldsymbol{f}\Delta t + \mathbf{b}\Delta\boldsymbol{w}, \tag{4.5}$$

---

[1] Proof: If $\boldsymbol{x}^T\mathbf{G}\boldsymbol{x} < 0$ for some real $\boldsymbol{x}$, then $\boldsymbol{x}^T\mathbf{b}^T\mathbf{b}\boldsymbol{x} = (\mathbf{b}\boldsymbol{x})^2 < 0$ implies that $\mathbf{b}$ is complex $\square$.

where $\Delta\boldsymbol{w}$ is a random Gaussian vector with the properties $\langle\Delta\boldsymbol{w}\rangle = 0$ (unbiased), and $\langle\Delta\boldsymbol{w}\Delta\boldsymbol{w}\rangle = 2k_BT\mathbf{I}$ (uncorrelated), and $\mathbf{b}$ is any matrix which satisfies $\mathbf{b}^T\mathbf{b} = \boldsymbol{\mu}$. We find $\mathbf{b}$ by computing the Cholesky decomposition of $\boldsymbol{\mu}$ and note that Cholesky decomposition requires $\boldsymbol{\mu}$ to be positive-definite, which is ensured by the RPY tensor. Because the mobilities $\boldsymbol{\mu}_{ij}$ vary slowly with respect to the timestep that we use, $\Delta t = 10^{-5}$, we update $\boldsymbol{\mu}$ once every 100 timesteps.

4.2.2 Polymer model

We follow the standard approach of modelling a polymer as a linear chain of mutually repulsive beads, linked by pairwise bonding potentials [122]. To model the mutual repulsion experienced by all particles in the simulation, we use the Weeks–Chandler–Andersen (WCA) potential:

$$\mathcal{H}_{\text{wca}}(\boldsymbol{r}_{ij}) = \begin{cases} 4\epsilon\left[\left(\frac{\sigma}{r_{ij}}\right)^{12} - \left(\frac{\sigma}{r_{ij}}\right)^{6}\right] + \epsilon_{ij}, & \text{if } r_{ij} < 2^{1/6}\sigma, \\ 0, & \text{otherwise.} \end{cases} \tag{4.6}$$

This is a shifted and truncated Lennard–Jones potential which consists of a purely repulsive part that smoothly decays to zero as r_{ij} approaches $2^{1/6}\sigma$, where σ is the characteristic length-scale of the interaction.

Any attractive bonding potential can be used to link polymer particles to one another. The simplest of these is the harmonic potential $\mathcal{H} \propto r_{ij}^2$. However, rare fluctuations can drive spurious behaviour in particle separation, which can lead to strands of a polymer crossing through each other, as well as unphysical variations in polymer contour length. Therefore, we use a finitely-extensible nonlinear elastic (Fene) potential [122]:

$$\mathcal{H}_{\text{Fene}}(\boldsymbol{r}_{ij}) = -\frac{1}{2}k_{\text{Fene}}r_0^2 \ln\left[1 - \left(\frac{r_{ij}}{r_0}\right)^2\right]. \tag{4.7}$$

This potential sets the maximum bead-separation at $r_{ij} = r_0$, and the strength of the potential is given by k_{Fene}. We use Kremer–Grest parameters [123] $k_{\text{Fene}} = 30\epsilon/\sigma^2$ and $r_0 = 1.5\sigma$. We choose $\epsilon = k_{\text{B}}T$ for the characteristic strength of the potentials, σ for the spatial unit, and $\sigma^2/\mu_0 k_{\text{B}}T$ for the temporal unit. This allows us to set $k_{\text{B}}T = 1$, $\sigma = 1$, $\mu_0 = 1$ hereafter. In these units, the bead diameter is $2^{1/6}$, hence $a = 2^{-5/6}$.

The conservative Hamiltonians $\mathcal{H}_{\text{WCA}}$ and $\mathcal{H}_{\text{Fene}}$ give rise to pairwise forces, $\boldsymbol{f}_i = -\boldsymbol{f}_j = -\boldsymbol{\nabla}[\mathcal{H}_{\text{WCA}}(\boldsymbol{r}_{ij}) + \mathcal{H}_{\text{Fene}}(\boldsymbol{r}_{ij})]$, which are the equal and opposite forces acting on particles i and j, and the relative separation is $\boldsymbol{r}_{ij} = \boldsymbol{r}_i - \boldsymbol{r}_j$.

4.2.3 Helical flagellum model

The rotating helix comprises a set of particles whose individual positions are externally controlled by time-dependent forces that prescribe the shape, rotational frequency ω and translational velocity v of the helix. This is done by applying a rectifying force that opposes displacements of a constituent particle from its prescribed location via a strong harmonic potential,

$$\mathcal{H}_h(\boldsymbol{r}_i, t) = \frac{1}{2}k_h[\boldsymbol{r}_i - \boldsymbol{r}_i^0(t)]^2, \tag{4.8}$$

$$\boldsymbol{r}_i^0 = \begin{pmatrix} R_0\cos(\kappa z_i^0 - \omega t) \\ R_0\sin(\kappa z_i^0 - \omega t) \\ z_i^0 + vt \end{pmatrix}. \tag{4.9}$$

The prescribed positions $\{\boldsymbol{r}_i^0\}$ trace a helix along $\boldsymbol{z}$, with an imposed radius R_0, and pitch κ (illustrated in Fig. 4.1). For the helix potential strength we use $k_h = 70\epsilon$. By applying the constraint that the target positions must be separated by diameter $2a$ in space, the required spacing in z is approximated by $z_i^0 = 2a/\sqrt{1+\kappa^2R^2}$. We impose a constant angular rotation rate ω about the z-axis, and enforce stationarity by setting $v = 0$ along the z-axis to keep the helix pinned, so it acts as a pump. Achieving force-free swimming, on the other hand, will be discussed in Chapter 6.

This model is adequate for reproducing the hydrodynamics of a rigid helix. Alternatively, modelling the helix as a semi-flexible polymer would require solving bonding angle and dihedral angle potentials with large stiffnesses [124], in turn requiring Δt to be many orders of magnitude below the shortest timescale of interest which for our purposes is the Kuhn relaxation time $\tau_0 \sim a^2/\mu_0 k_{\text{B}}T$ of the beads [13]. As we are not interested in effects due to flagellar elasticity, it suits our purposes better to model the helix using the external potential $\mathcal{H}_h$ as this ensures that torques and forces are distributed evenly across the entire filament, as would be the case for a rigid helix.

The helix particles (labelled by subscript i) are initialised in their target positions at $t = 0$, and then the helix as a whole relaxes into a steady state after a short transient period. The steady state differs slightly from the target shape due to (1) a viscous, drag-induced phase lag behind their target position, causing a shrinkage in their radial coordinate which can be shown to be $R = R_0/\sqrt{1 + (\mu_0 \omega / k_h)^2}$ when no hydrodynamic interactions are present and (2) an additional collective displacement along $\hat{\boldsymbol{z}}$ due to chiral asymmetry in the hydrodynamic interactions $\sum_{j(\neq i)} \boldsymbol{\mu}_{ij} \boldsymbol{f}_j$ with the other helix particles. For $v = 0$, these displacements δz_i are counteracted by a net force on the helix $(-)\frac{\partial \mathcal{H}_h}{\partial z} = -N_h k_h \delta z$ which is imparted to the fluid in the z-direction.

With this control over ω and v, we can drag, rotate or apply some combination of translation and rotation to the helix. The imposed rotation and translation implies an external axial force and torque via the linear mobility relation [12],

$$\begin{bmatrix} v \\ \omega \end{bmatrix} = \begin{bmatrix} \mu^t & \mu^{tr} \\ \mu^{rt} & \mu^r \end{bmatrix} \begin{bmatrix} f_z \\ \tau_z \end{bmatrix}, \tag{4.10}$$

where the components μ^t, $\mu^{tr} = \mu^{rt}$, μ^r are mobility coefficients for the helix as a whole, and not to be confused with the RPY tensor $\boldsymbol{\mu}$. In general, the full mobility relation also includes off-axis force and torque components $f_{x,y}$ and $\tau_{x,y}$, however these are small compared to f_z and τ_z. Because the potential $\mathcal{H}_h$ keeps the helix centered and aligned along $\hat{\boldsymbol{z}}$, any off-axis contributions to the fluid flow are very small.

4.3 Verification of polymer dynamics

4.3.1 Polymers in solution

The first test of our SD model is to verify that it can reproduce the correct statistical physics of polymers in solution. Two of the most important statistical properties of polymers are the gyration radius, R_g, and relaxation time τ [13]. These are the characteristic length and time scales associated with a polymer, and both obey a respective power law scaling as a function of N. We will briefly review the theory behind these quantities before comparing them with the results of our simulations.

The gyration radius measures the characteristic spatial extent of a polymer in equilibrium, and is defined as the second moment of the set of monomer positions $\{\boldsymbol{r}_i\}$:

$$R_g^2 = \langle (\boldsymbol{r}_i - \bar{\boldsymbol{r}})^2 \rangle, \tag{4.11}$$

where $\bar{\boldsymbol{r}} = \langle \boldsymbol{r}_i \rangle$ is the centre-of-mass of the polymer.

One of the simplest models of a polymer is the Gaussian chain model [13], in which we imagine the polymer to be made up of beads that are connected together by harmonic potentials. In this case, the radius of gyration can be shown to be $R_g = \sqrt{\frac{N}{6}b^2}$, i.e., $R_g \propto N^{\frac{1}{2}}$. However this model fails to capture the self-exclusion that results from a polymer being composed of beads of a finite size. This means that in general, the gyration radius of real polymers obey $R_g \propto N^{\nu}$ with $\nu > 0.5$. Numerical studies of the monomer distribution function with volume exclusion give an estimation of the exponent ν as $\nu \approx 0.588(1)$ [125].

The gyration radius is an ensemble average, and therefore does not depend on hydrodynamic interactions. However, dynamic properties such as the relaxation time do depend on hydrodynamic interactions. Two models which describe a polymer with and without hydrodynamic interactions are the Zimm model and Rouse model respectively [13]. These two models have different dynamic scaling laws for relaxation time, and are given by $\tau_R \propto N^{1+2\nu}$, for the Rouse time and $\tau_Z \propto N^{3\nu}$ for the Zimm time. The Zimm model is mostly used for polymers in dilute suspensions, where hydrodynamic self-interactions alter their dynamics [126].

4.3.2 Single polymer simulations

With our Brownian dynamics scheme, we conducted simulations of polymers composed of different numbers of beads, $N \in [4, 70]$, and tracked the positions of each bead over long times. We conducted identical simulations both with and without hydrodynamic interactions. We measured the gyration radius of each polymer at each point in time via Eq. (4.11), and then averaged R_g over the entire simulation. The results are plotted in Fig. 4.2(a) and show that the large-N scaling of R_g is in good

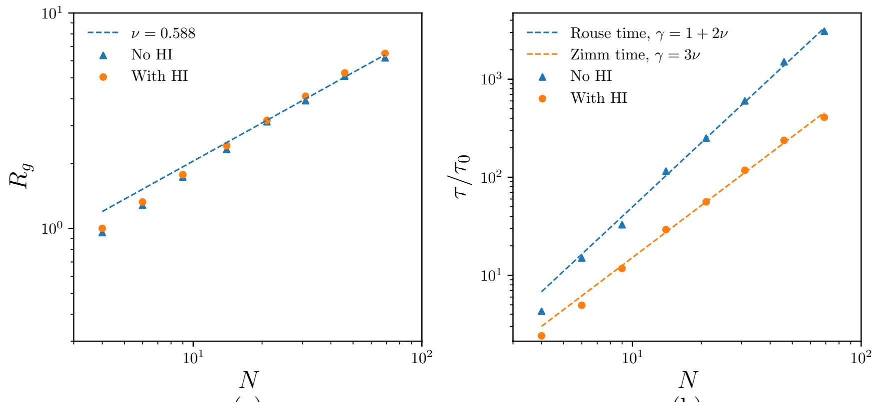

(a) (b)

Figure 4.2: (a) Scaling of gyration radius R_g as a function of polymer size N measured using SD simulations without hydrodynamic interactions (blue triangles), and with hydrodynamic interactions (orange circles). Superimposed (blue dotted line) is the theoretical scaling $R_g \propto N^\nu$ with $\nu = 0.588$. (b) The same simulations used to measure the scaling of the relaxation time τ, relative to the Kuhn time $\tau_0 = a^2/\mu_0 k_B T$, as a function of polymer size. The Rouse time $\tau_R \propto N^{1+2\nu}$ (blue dotted line), and Zimm time $\tau_Z \propto N^{3\nu}$ are shown for comparison.

agreement with the theoretical scaling $R_g \propto N^\eta$ with $\eta = 0.588$. Hydrodynamic interactions do not alter this scaling relationship, as expected. For very small polymers $N \leq 10$, we see a slight divergence from the theory which suggests that due to the finite size of the beads, very small polymers are more rod-like.

Using the gyration radius, we estimate the relaxation time as the time taken for the centre of mass of the polymer to diffuse a distance equal to the gyration radius [126]. The results of this calculation are shown in Fig. 4.2(b). We see that the simulations with and without hydrodynamic interactions obey the Zimm and Rouse relaxation time scaling laws respectively, as expected.

4.4 Hydrodynamics of a pinned helix

4.4.1 Instantaneous and time-averaged flow fields

In this section we describe the flow field generated by a pinned, rotating helix. In this case, $v = 0$ and $\omega \neq 0$ are both held constant. Eq. (4.10) implies that a nonzero net force $f_z = -\frac{\mu^{tr}}{\mu^t}\tau_z$ must be imparted on the helix, where τ_z is the torque required to maintain constant angular rotation. This system is similar to

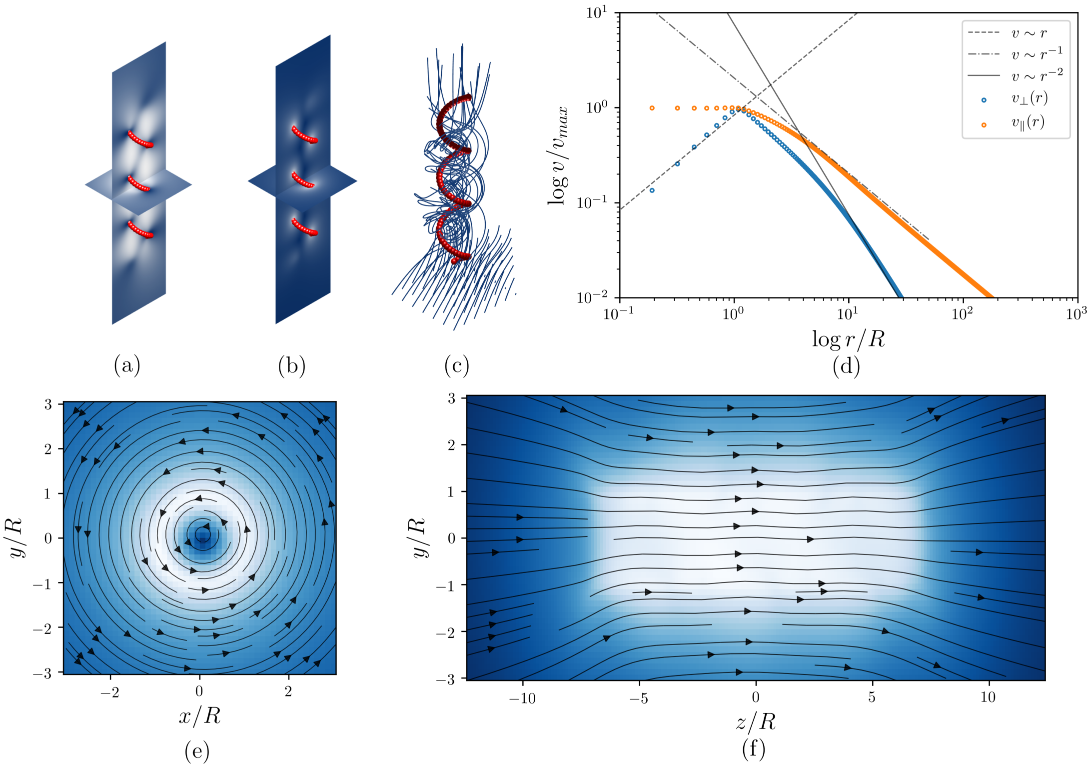

Figure 4.3: (a-b) Cross sections of the instantaneous flow field generated by a rotating helix, decomposed into components $v_z(\boldsymbol{r}, t)$ and $v_\perp(\boldsymbol{r}, t)$ respectively; (c) Streamlines of the full flow field $\boldsymbol{v}(\boldsymbol{r}, t)$ shows both the net flow along $\hat{\boldsymbol{z}}$ and the chiral winding caused by the rotation of the helix; (d) Time-averaged fields as a function of radial distance from helix center-line, $\bar{v}_z(r, t)$ and $\bar{v}_\perp(r, t)$. Within the volume enclosed by the helical filament ($r < R$), the fluid rotates like a rigid body, $v_\perp \propto r$, and flows axially at a constant rate $v_r = \text{const}$; (e) Slice in the xy-plane of the mean rotational flow; (f) Slice in the xz-plane of the mean axial flow.

microscopic experiments on tethered bacteria [109, 127, 128] as well as macroscopic experiments of wall-attached flagella-like filaments [112, 129–132].

In the SD simulations it is possible to evaluate the instantaneous flow field at any point $\boldsymbol{r}$ in space by summing the contributions that each particle in the simulation makes: $\boldsymbol{v}(\boldsymbol{r}) = \sum_i \boldsymbol{\mu}(\boldsymbol{r} - \boldsymbol{r}_i)\boldsymbol{f}_i$, where $\boldsymbol{\mu}(\boldsymbol{r})$ is the RPY tensor Eq. (4.4). This is the virtual displacement that a point-like SD particle would experience if placed at that location in the fluid with no other external forces acting on it, in other words, a tracer particle.

In Fig. 4.3(a), the axial component of the velocity, v_z, shows that the fluid is most strongly pumped in the interstitial volume of the helix, similar to the instantaneous axial flow field measured in experiments on a tethered rotating helix [132]. As the axial velocities of the helix beads are 0, v_z must vanish at the helix surface. Conversely, the transverse flow $v_\perp$ is maximal at the helix surface, as can be seen in Fig. 4.3(b), as it must match the transverse velocity of the beads which themselves are undergoing circular (i.e., purely transverse) motion.

Fig. 4.3(c) demonstrates an instantaneous snapshot of the flow: streamlines originating from a square grid at the ‘upstream’ end of the helix, are drawn chaotically inward and spiral into the helix core. Note that the streamlines originate from the bottom of the figure with a net direction in the xy-plane. This is because, in general, a full helix mobility tensor (including couplings to forces and torques in x and y in addition to the ones in z that we consider in Eq. 4.10) couples off-axis translations and rotations to axial forces and torques. Because we specify $\boldsymbol{v} = \mathbf{0}$ and $\boldsymbol{\omega} = (0, 0, \omega)$, we force the helix to remain centred on, and aligned with, the z-axis. Therefore, there must be small off-axis forces and torques which are set up in order to maintain this alignment. In other words, turning the helix and forcing it to remain aligned will in turn impart an off-axis torque on the fluid. This is manifested as an off-axis flow field which rotates with the helix.

These instantaneous flows can be averaged over time to understand what the far-field scaling of the flow looks like. We take a time average over a complete revolution, $\bar{\boldsymbol{v}}(x, y, z)$, and, decomposing this into transverse and axial components, $\bar{v}_\perp$, and $\bar{v}_z$, we plot how these scale as a function of radial distance from the centre of the helix in Fig. 4.3(d). Far away from the helix, we observe $\bar{v}_z \sim 1/r$, which is the characteristic scaling of a stokeslet. This is as expected since we must apply a force f_z on the helix to ensure that the rotating helix remains pinned. Therefore, at large distances away from the helix, the fluid response is that of a stokeslet.

The transverse velocity characteristically scales like a rotlet, $\bar{v}_\perp \sim 1/r^2$, which we expect to dominate the far-field flow created by an external torque rotating a body immersed in the fluid. However, in the intermediate region ($R < r < 10R$), the transverse forces on the beads on the near-side of the helix dominate over the

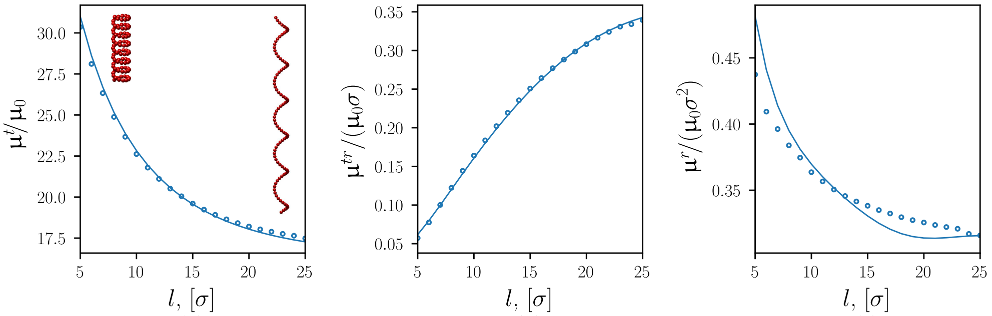

(a) (b) (c)

Figure 4.4: The three components of the helix friction tensor as a function of pitch length $l = 2\pi/\kappa$. The data (black dots) are determined by measuring f_z, and τ_z separately as functions of v and ω for different κ in order to determine the matrix components μ^t, μ^{tr} and μ^r. The solid lines are calculated using analytical results from slender body theory (Eqs. (44) from Ref. [8]). Increasing the pitch length decreases the isotropic components of the friction tensor, while increasing the coupling between rotation and translation. Inset: The helix shapes for the extremal choices of pitch.

oppositely directed forces on the far side, and therefore a stokeslet-like scaling $\bar{v}_\perp \sim 1/r$ is seen.

Within the interior of the helix, we see interesting scaling properties $\bar{v}_z \sim \text{const}$, and $\bar{v}_\perp \sim r$, which shows that on average the fluid inside the helix rotates about $\hat{\boldsymbol{z}}$ and translates along $\hat{\boldsymbol{z}}$ as a rigid body, although the instantaneous dynamics are more complicated.

Figures 4.3(e-f) show the time averaged flow fields. The transverse flow field is strongest in the annular region occupied by the helical filament itself, while the axial flow field is uniformly strong across the whole volume.

4.4.2 Friction tensor of helical filament in SD simulations

In order to measure the helix mobility, we conducted SD simulations of a helix (with no polymer present) while linearly ramping up either the velocity or angular velocity — while keeping the other zero. In the first instance $v = v_0 t/\mathcal{T}$, and $\omega = 0$ were imposed and in the second instance $v = 0$, and $\omega = \omega_0 t/\mathcal{T}$ were imposed. The constants v_0 and ω_0 were the target final velocities and the length of the simulation, $\mathcal{T}$, was sufficiently long to ensure that the system remained in a quasi–steady-state. In both cases, we measured (f_z, τ_z) in order to solve the linear system Eq. (4.10). We conducted this for a range of $\kappa \in [\frac{2\pi}{25}, \frac{2\pi}{5}]$ to measure how the friction components changed as a function of helix shape. The functional dependence of these coefficients on κ can be derived analytically using slender body theory [133, 134]. The result may be written more easily in terms of the pitch angle $\vartheta = \tan^{-1}(\kappa R)$ [see Fig. 4.1], and helical phase $\varphi = \kappa z$ [8]:

$$\mu^t = \frac{1}{4\pi\eta}\left(\sin^2\vartheta + \frac{1}{\sin\vartheta}\int_{\varphi_0}^{\varphi_L}\left(\frac{1}{\Phi} + \frac{\varphi^2\cot^2\vartheta}{\Phi^3}\right)\mathrm{d}\varphi\right), \tag{4.12}$$

$$\mu^{tr} = \frac{1}{4\pi\eta R}\left(-\frac{1}{2}\sin 2\vartheta + \frac{1}{\sin\vartheta}\int_{\varphi_0}^{\varphi_L}\frac{\varphi\sin\varphi\cot\vartheta}{\Phi^3}\mathrm{d}\varphi\right), \tag{4.13}$$

$$\mu^r = \frac{1}{4\pi\eta R^2}\left(\cos^2\vartheta + \frac{1}{\sin\vartheta}\int_{\varphi_0}^{\varphi_L}\left(\frac{\cos\varphi}{\Phi} + \frac{\sin^2\varphi}{\Phi^3}\right)\mathrm{d}\varphi\right). \tag{4.14}$$

The limits of the integrals are $\varphi_0 = \kappa\delta\cos\vartheta$, and $\varphi_L = \kappa L\cos\vartheta$, where $L = Na$ is the contour length of the helix, δ is a cutoff parameter, and the terms that appears in the integrands contain $\Phi = \sqrt{4\sin^2(\varphi/2) + \varphi^2\cot^2\vartheta}$. The only free parameter in these equations is the cutoff length δ.

Once we measured the friction tensor components from the SD simulation, we fitted Eqs. (4.12) and found good agreement using $\delta \approx 0.8a$. The results are shown in Fig. 4.4.

We observe that as the pitch length increases, μ^t and μ^r decrease and μ^{tr} increases. This tells us that the coupling between axial force and rotation (or conversely between applied torque and resulting translational speed) increases as the pitch length is increased over the range shown. This behaviour can be understood intuitively by considering the limiting case of small pitch length $2\pi/\kappa \to \sigma$, in which the filament resembles a cylinder, which by symmetry must have a totally decoupled mobility relation.

The data for μ^t and μ^{tr} fit very well to the slender body prediction. However, while μ^r qualitatively displays a similar dependence on pitch length to the analytic prediction, it appears to systematically deviate from the theory. As previously discussed, the steady state shape of the helix realised in a simulation deviates slightly from its target shape [defined by Eq. (4.8)]. This effect of this is generally small, but it appears that μ^r is the more sensitive to this dynamic remodelling than the other components of the mobility matrix. However, in the remainder of this study, we will only conduct simulations in which the helix parameters remain constant and so this discrepancy in μ^r as a function of κ does not affect our findings.

4.5 Conclusions

In this chapter we have provided the motivation for studying cell locomotion through viscoelastic fluids, and outlined the need to understand such physics on the mesoscopic polymer–flagellum level.

Introducing our model system of an externally actuated rotating helix near a passive polymer, we have developed a Brownian dynamics scheme to understand via simulation how the two elements of our model interact. We have also taken care to verify that our simulation model produces results that agree with both the well-known statistical physics of polymers, and separately, the hydrodynamics of helical flagella.

In the following two chapters, we provide evidence that our model system has biological veracity and report on simulations conducted on both pinned and swimming helices.

5

Polymer driven by a pinned helix

In this chapter, we will use our Stokesian dynamics model of a helical flagellum to study the hydrodynamic interactions between a polymer and a pinned rotating helix. This pinning requires a net force to be applied to arrest any translational motion; the net force is in turn applied by the helix to the fluid, resulting in the helix acting like a pump.

In the first part of the chapter, we argue that this minimal model bears close resemblance to the biologically relevant situation of a tethered cell, and present evidence for this by comparing the near-field flows to a more geometrically faithful simulation. This kind of tethered cell system might occur *in vivo* when cells accumulate at surfaces, or in an *in vitro* assay when they are made to chemically adhere to a microscope slide [30, 127, 128].

We then present our main result, that as a stationary rotating helix pumps fluid along its long axis, polymers migrate radially inwards while becoming elongated. We observe that the actuation of the helix tends to *increase* the probability of finding polymeric material within its pervaded volume — in other words polymers become ‘captured’. We also show that this accumulation of polymers within the vicinity of the helix is stronger for longer polymers.

In the final part of the chapter, we demonstrate that it is possible to measure the excess work that the helical flagellum must do on a polymer. We show that it is positive on average, and discuss the relationship between the extra power that the helix must output and the energy stored in the polymer when its nonequilibrium stretched state is maintained.

5.1 Biological scope of our model

Because our model helix remains in a fixed location along $\hat{\boldsymbol{z}}$, it is neither force-free nor torque-free, hence its flow field will differ to that generated by a swimming cell in the far-field. Artificial swimming magnetic ribbons [26, 27] are arguably the most similar experimental realisation of our system due to the net torque they impart, but unless they are stalled by an external force, they remain force-free too. Hence, the force and torque nature of our model is more akin to systems in which flagellated cells are in some way stalled or tethered: e.g., by hydrodynamic accumulation at boundaries [30], immobilisation on microscope slides [127, 128], or as part of their biological function [116, 117]. However in these cases, hydrodynamic interactions with the boundaries and cell bodies are a potential source of discrepancy between the results of our model and these experimental and biological systems.

To quantify this difference and determine whether our system is a sufficiently good model for studying the near-flagellum dynamics, we compared the flow fields measured from the SD simulations to multiparticle collision dynamics (MPCD) simulations of a more experimentally realistic geometry with a cell body and neighbouring wall. These simulations were performed by Dr. Andreas Zöttl and are outlined by Zöttl & Yeomans (2017) and Balin et al. (2017) [135, 136]. In Fig. 5.1, we compared the time averaged flow fields $\bar{v}^M$ and $\bar{v}^S$ generated by the MPCD and SD simulations respectively. Both quantities were normalised by dividing by the mean velocity inside the volume occupied by the helix. By visual inspection, we observe that the coarse structure of the axial and transverse flows are qualitatively similar in both simulations.

To quantitatively compare the two fields, we analysed the absolute differences $|\bar{v}^M_{z,\perp} - \bar{v}^S_{z,\perp}|$ to see how they decay relative to one another. In Fig. 5.1(c) we can see that $|\bar{v}^M_\perp - \bar{v}^S_\perp|$ appears to have a noisy structure. A Kolmogorov–Smirnov test on

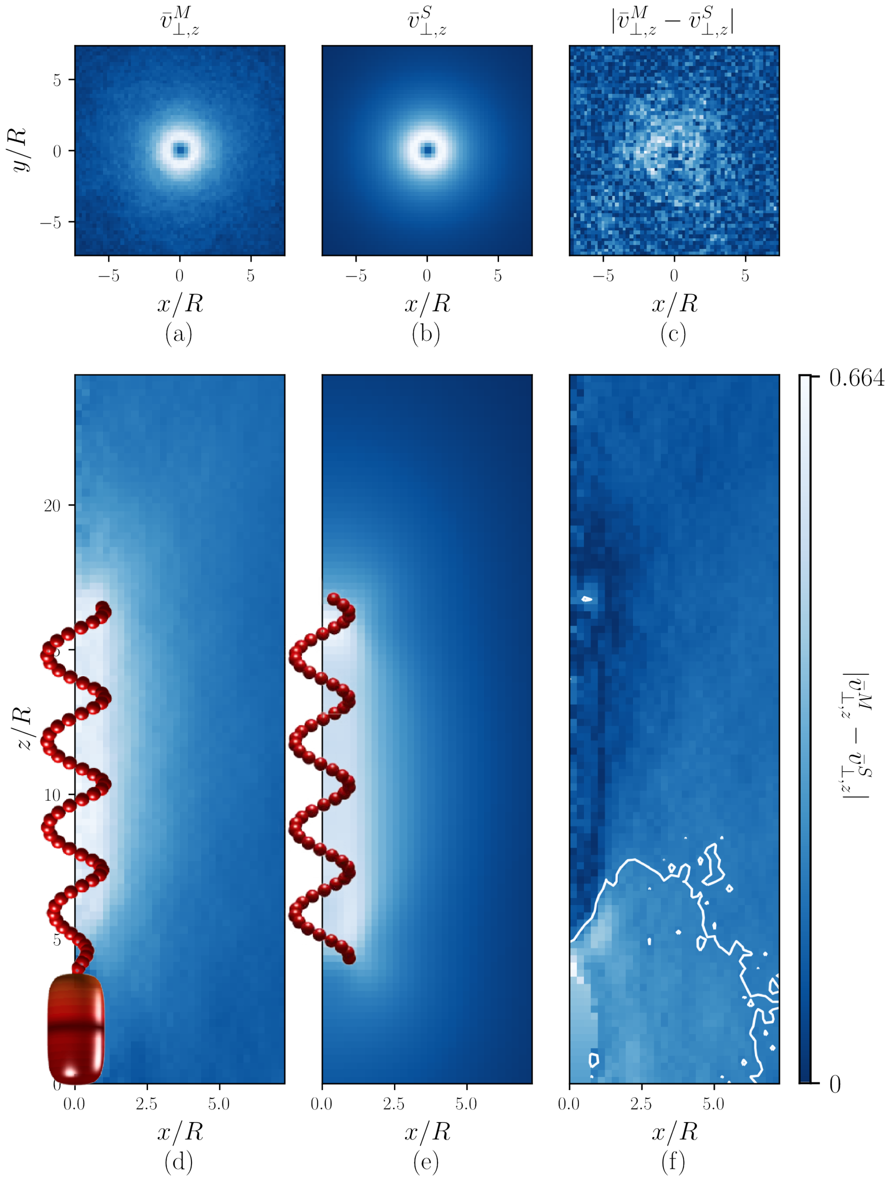

Figure 5.1: (a-c) Comparison of the time-averaged flow fields generated by (a) MCPD fluid simulations of a cell attached to a wall versus (b) SD simulations of a helix rotating in a bulk fluid computed in the xy-plane. These two measured fields differ only by Gaussian fluctuations inherent in the MPCD simulation as shown in (c). (d-f) Same as (a-c) except in xz-plane. (f) shows that there are systematic differences in the flow fields in this plane, mainly due to the presence of the wall. The contour-enclosed region in the lower quarter of the image represents where the flow field differs by $|\bar{v}_z^{MPCD} - \bar{v}_z^{SD}| > 0.3$. Everywhere else, the fields behave similarly.

the data did not yield evidence for a non-Gaussian distribution, and so we conclude that $\bar{v}^M_\perp$ differs from $\bar{v}^S_\perp$ by the Gaussian noise present in the MPCD simulation only.

However, there are more significant differences in the radial flow fields due to the presence of the cell body and the wall in the MPCD simulations. The difference $|\bar{v}_z^M - \bar{v}_z^S|$, plotted in Fig. 5.1(f), reveals a systematic variation across the whole region that is roughly one order of magnitude greater than the noise in Fig. 5.1(c). The contour-enclosed area connected to the wall (at $z = 0$) shows the region in which the flow fields differ by $|\bar{v}_z^M - \bar{v}_z^S| > 0.3$. Evidently, the cell body and wall have some significant influence on the flow in this region but not in the immediate vicinity of the model flagellum.

The fact that the radial fields are in better agreement than the axial fields can be understood by noting that $\bar{v}_\perp \sim 1/r^2$ decays over shorter distances than $\bar{v}_z \sim 1/r$, and hence the wall-effects play a much larger role for the axial fields.

Since our main focus in this paper is the near-flagellum dynamics of polymers and helices interacting across length scales similar to and less than their own spatial dimensions, we take these MPCD results as evidence that far-field effects (such as those generated by counter-rotating cell bodies, solid boundaries, and indeed other nearby swimmers or filaments) do not contribute appreciably to the dynamics of polymers sufficiently close to the helical filament. In this region, we expect the chiral, high-shear and geometry-specific flow of the helix to characterise the behaviour of a nearby polymer, and far-field effects due to boundaries or other bodies to be secondary.

5.2 Polymer capture

The central result of this chapter is that a rotating helix transports a polymer along with the fluid it pumps, but in such a way that a polymer initially on the outside of the helix is drawn inwards and ‘captured’ by the helix. This is accompanied by an initial stretching out of the polymer as it migrates towards the helix, moving into a region of greater shear and greater flow as seen in Fig. 5.2. As it is transported along the interior of the helix, it occasionally wraps around the helical filament and rotates along with it. An instance of such wrapping is observed in Fig. 5.2. The polymer is deposited at the end of the helix, where a decaying axial current keeps moving it at a diminishing rate, while the lower shear results in the polymer collapsing back into its unstretched ground state.

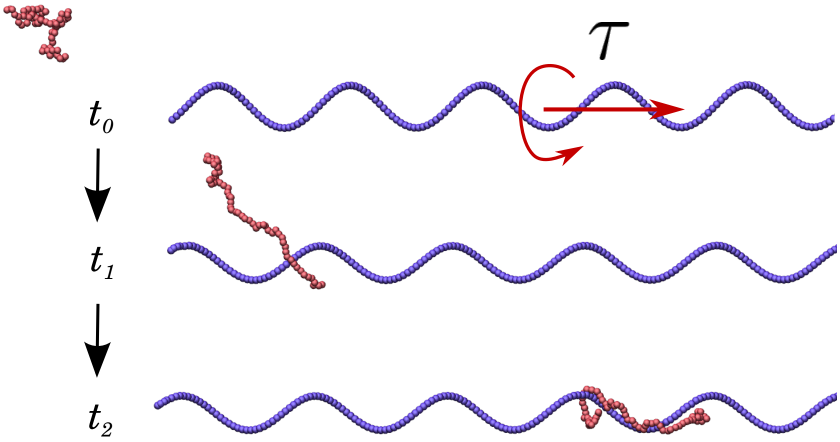

Figure 5.2: Snapshots from a single simulation of a rotating helix and an advected polymer taken at times $t_0 < t_1 < t_2$. A torque $\boldsymbol{\tau}$ is distributed uniformly on the helix and, as it rotates, it generates a pumping flow. The polymer is drawn in radially and axially towards the helix, stretching in the process due to the induced shear flow. Once captured it winds around the helix and is pumped axially in the direction of the average flow.

The polymer capture and transport is a stochastic, nonequilibrium transient process; however, by performing a large number of 'scattering' simulations and averaging over these, we are able to quantify the typical nature of the interaction as a function of polymer size. We present batches of simulations for degrees of polymerisation (number of beads) $N = \{1, 10, 30, 50\}$, where a polymer of contour length 1 is simply a spherical monomer. In each of these simulations, we use helices with the same parameters: $N_h = 200$ beads, $\kappa = 2\pi/15\sigma$, $R = 4\sigma$. The helix is centered along the z-axis, with its two ends located at (z_0, z_{N_h-1}). In each simulation, one polymer is initialised by placing its first monomer randomly on a disc of radius 16σ [demonstrated schematically in Fig. 4.1], located at $(z_0 - 30\sigma)$, then performing a self-avoiding random walk to build the polymer bead by bead.

To illustrate how the ensembles of polymers evolve in time, we plot the average monomer distribution in cylindrical coordinates (r, z) taken over all simulations and at all times. These are plotted for polymers of differing size in Fig. 5.3(a-d). These images represent time- and ensemble-averaged 2D histograms of the snapshots shown in Fig. 5.2. At the left edge of each of the images is the initial distribution of polymeric material which in each case is smeared rightward in time. The structure of this distribution gives a graphical indication that larger polymers [such as in Fig. 5.3(c-d)] are much more strongly attracted to the helix than smaller polymers and are highly concentrated in the region $r < 2R$. On the other hand, in Fig. 5.3(a) this effect is barely observed for $N = 1$ monomers, which are simply advected along the streamlines shown in Fig. 4.3(f) like tracer particles that cannot cross streamlines; polymers, on the other hand are able to cross streamlines in shear flow [137], and in this case do so strongly in a non-trivial manner.

Particularly for the larger polymers, we observe hotspots in the distributions located at the downstream end of the helix. These indicate the accumulation of polymers in this location when they are deposited at the end of the helix and collapse back into their equilibrium conformation. Though they continue moving along the z-axis, they do so at a lower rate than when inside the helix. This is because the magnitude of the axial flow, $|\boldsymbol{v}_z|$, quickly decreases outside of the helix [as can be seen in Fig. 4.3(f)].

In Fig. 5.3(e-h) we segment each simulation into four equal and contiguous intervals in time, and separately plot the marginal distributions over r only (i.e., with the z-component integrated out) for each time. The shaded region represents the interval $t_0 = [0, \mathcal{T}/4]$, which is the first quarter of each simulation and closely approximates the initial distribution. These figures show how the initial distribution evolves with time for polymers of different size. For $N = 30$ and $N = 50$, the tendency to concentrate in and around the helix is markedly stronger than for shorter polymers. This ensemble behaviour shows that the actuation of the helix is responsible for a large density fluctuation in the surrounding polymeric material that concentrates — rather than depletes — the polymers in the immediately surrounding region.

This implies that the free energy of the polymers must be actively driven away from what we would expect in equilibrium. We obtain an intuitive sense that this is occurring by considering the snapshots in Fig. 5.2. Initially, the polymer is far away and its configuration is that of a self-avoiding random walk. However at intermediate times, the polymer is stretched out of equilibrium by the shear flow

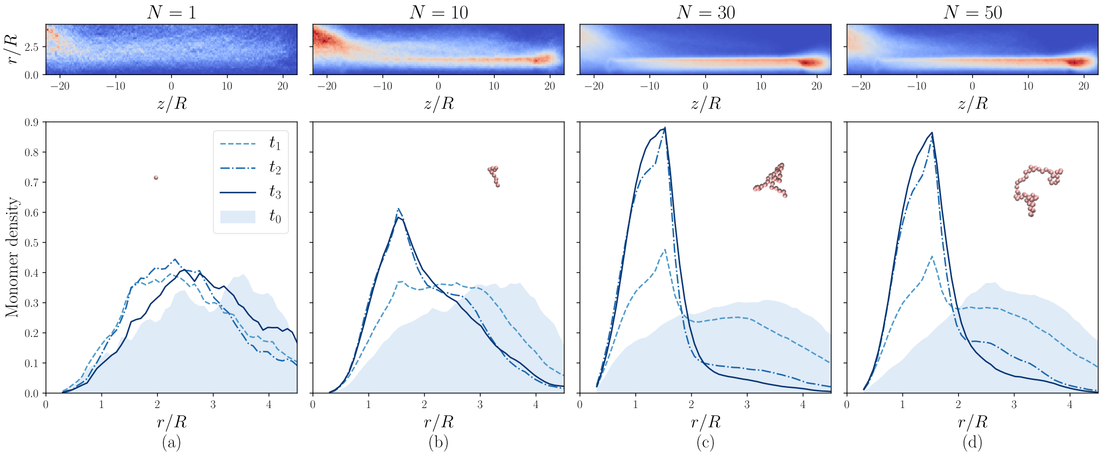

Figure 5.3: Polymer distributions due to pinned helix averaged over 200 simulations for polymers of size (a) $N = 1$ (monomers), (b) $N = 10$, (c) $N = 30$ and (d) $N = 50$. Upper images show 2-dimensional histograms of all polymeric particle (r, z)-positions in cylindrical co-ordinates relative to the helix centre-of-mass, integrated over all time. Lower graphs show 1-dimensional histograms of radial positions r, averaged over four contiguous quarters of each simulation —i.e., total period, $\mathcal{T} = t_0 \cup t_1 \cup t_2 \cup t_3$. First-quarter distributions (including the initial distributions) are highlighted by the shaded region.

and is transported radially inwards as well as along z until it strongly interacts with the helix, wrapping around it and continuing to move along z. In the vicinity of the helix, polymers lose their equilibrium conformation, and we observe features in their dynamics similar to those previously reported for polymers in shear flow due to a rotating microwire [138]. To gain further insight into the energetic interplay within our system, we then analysed the stochastic fluctuations in work performed by the helix on the polymer.

5.3 Fluctuating work and dissipation

Polymers tend to become stretched when immersed in a shear flow [106], and this agrees with the SD simulations presented here. However, because the shear flow in this case is generated by external forces acting on the helix, we expect these forces to be dependent on the proximity of a polymer in the surrounding medium. The hydrodynamic origin of this is due to the effect of the polymer on the helix particles: hydrodynamic interactions displace the helix particles from their steady state positions resulting in a change in the forces acting on them due to Eq. (4.8). While these displacements are too small to give rise to a perceptible change in helix shape, they should in general manifest themselves as a change in work that the helix must do to maintain steady rotation.

The work applied to the helix by the external forces, $w[t, \boldsymbol{r}(t)]$, is a fluctuating quantity which is a unique function for each realisation of a stochastic dynamical process. Work is performed either by the application of a nonconservative force, or by a time-varying potential $\mathcal{H}(\boldsymbol{r}, \lambda(t))$ with an external control parameter $\lambda(t)$. For the latter case, the work applied by a time t is defined by [139]:

$$w[t, \boldsymbol{r}(t)] = \int_0^t \mathrm{d}t' \dot{\lambda} \frac{\partial \mathcal{H}}{\partial \lambda}. \tag{5.1}$$

The nonstochastic forces in our simulation are due to the potentials $\mathcal{H}_{\mathrm{WCA}}$, $\mathcal{H}_{\mathrm{Fene}}$ and $\mathcal{H}_h$ in Eqs. (4.6,4.7,4.8). Of these, only the forces acting on the helix due to $\mathcal{H}_h$ depend explicitly on time and it is these that are entirely responsible for the work done on the system.

For each simulation, we calculate the incremental work performed by the helix at each timestep by,

$$\Delta w = \sum_i \boldsymbol{f}_i^h \cdot \Delta \boldsymbol{r}_i^0, \tag{5.2}$$

where $\boldsymbol{f}_i^h = -\boldsymbol{\nabla} \mathcal{H}_h(\boldsymbol{r}_i, t)$ is time-varying force applied to particle i. Note the increment $\Delta \boldsymbol{r}_i^0$ is the displacement of the bead target position, not the displacement of the bead itself. From these increments Δw we build up an accumulated work trajectory $w(t) = \sum_t \Delta w$.

We expect there to be two contributions to the work: $w(t) = w_0(t) + w_{ex}(t)$. The dominant contribution $w_0(t)$ is the deterministic work done by the rigid helix on the fluid, which is viscously dissipated. The second contribution is $w_{ex}(t)$, which is the stochastic excess work done on the polymer. By conducting simulations without a polymer, we can measure the dominant viscous contribution, $w_0(t)$, and use this to calculate the excess contribution in simulations that do contain a polymer: $w_{ex}(t) = w(t) - w_0(t)$.

In Fig. 5.4 we plot three ensembles of trajectories $w_{ex}(t)$ for the work done by a helix on three sizes of polymer: $N = (10, 20, 40)$. In each simulation, the polymer is initialised by a self-avoiding random walk starting at $\boldsymbol{r}_0 = (0, 15\sigma, (z_0 - 15)\sigma)$, where z_0 is the z-position of the negative-most particle of the helix, which pumps fluid in the positive-z direction. We measure $w_{ex}(t)$ for the entirety of each simulation over a time interval of 80 full rotations. For all simulations this is enough time to allow for the polymer to relax back to its equilibrium conformation after it has exited the positive-z end of the helix.

These sets of trajectories offer another way to look at the stretching effect: a set of stochastic work trajectories $\{w_i[t, \boldsymbol{r}(t)]\}$ drive the polymer to a higher free energy state though in each instance requiring a different amount of work. The colour of each curve denotes the radial point of closest approach of the center-of-mass position of the polymer — i.e., the minimum of $r_{\text{cm}}(t)/R$ over all t — from which we can see that more work was done on polymers which migrated further in. This indicates that more work must be done on maintaining the stretched-out conformation which polymers adopt in the high-shear region of the helix core.

The trajectories are nonmonotonic, and some trajectories temporarily deviate into the negative work region, which is a hallmark of the thermodynamics of stochastic systems [139]. We further notice that once the polymer has exited the helix, $w_{ex}(t)$ flattens dramatically. This corresponds to the observation that when the polymer is deposited at the rear end of the helix, it quickly collapses to its equilibrium configuration and highlights that the rotation of the helix principally impacts polymers in its immediate vicinity. Furthermore, the fact that $w_{ex}(t)$ does not overshoot its final value tells us that the helix does not regain any of the work it has supplied to the polymer when the polymer relaxes. This is in contrast to the observed enhancement of swimming due to the energetics of noiseless elastic surroundings [140, 141]. In such systems, elastic networks or tubes which a swimmer swims through store elastic energy and transfer this energy back to during relaxation. However, in our system, the heat bath to which the polymer is attached robs the helix of any such energy 'storage' mechanism.

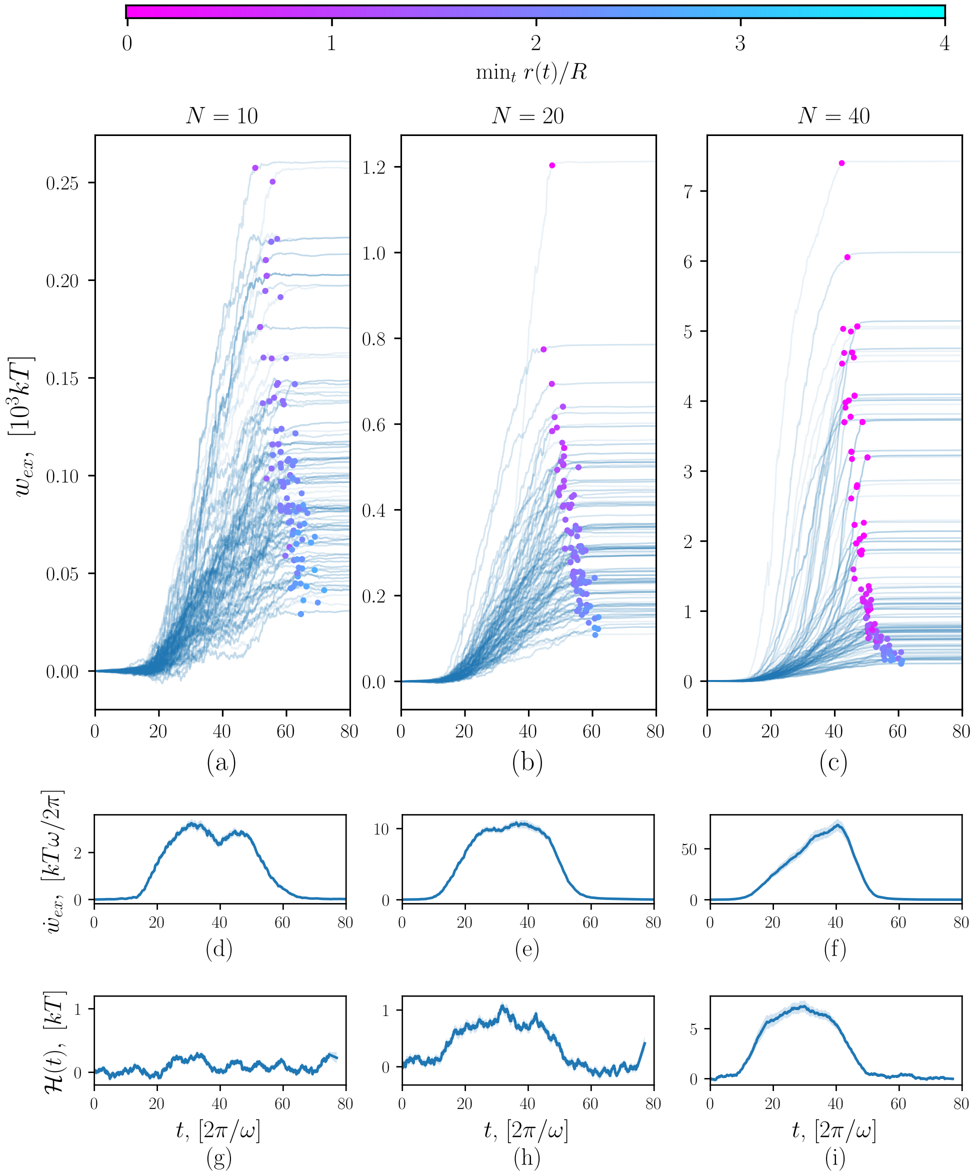

Figure 5.4: (a-c) Stochastic excess work performed by a rotating helix in transporting polymers of size $N = (10, 20, 40)$ respectively in 200 experiments performed for each case. The markers correspond to the point at which the centre-of-mass of the polymer exits the negative end of the helix. Once this occurs, the polymers collapse and advect with the fluid; no more work is performed on them. The markers are colour coded by the point of closest approach to the central long axis of the helix for the polymer in that experiment, $\min_t(r)$. More work on average was performed to transport polymers that migrated nearer (magenta) the central axis than on polymers which failed to become captured (cyan). (d-f) Mean excess power per revolution, averaged over 200 simulations. For each time-step, Δw_{ex} was calculated and smoothed with a window size of $\sim 1/4$ revolution. The shaded region corresponds to the standard error on the mean. (g-i) Mean increase in polymer energy calculated using the potentials $\mathcal{H}_{\text{WCA1}}$ and $\mathcal{H}_{\text{Fene}}$ with the same smoothing and averaging procedure employed in (d-f).

To gain further insight, we measured the change energy stored in the polymers by computing $\mathcal{H}(t) = \mathcal{H}_{\mathrm{Fene}}(t) + \mathcal{H}_{\mathrm{WCA}}(t)$ and subtracting away the minimum attainable energy. After smoothing these traces using a Savitzky–Golay filter with a window size of $\sim 1/4$ helix revolutions, and then averaging over all simulations, we obtain an indication of how the energy stored in the polymer increases on average. We also applied the same smoothing and averaging procedure to the work increments $\Delta w_{ex}(t)$ to compare how the mean energy stored in the polymers was related to the work rate of the helix. These results are plotted in Fig. 5.4(d-i). We see no measurable increase in stored energy for the $N = 10$ polymer, but statistically significant increases for the $N = 20$ and $N = 40$ polymers. These increases in energy are due to the elongation the larger polymers suffer when they are captured by the helix — a phenomenon which we have shown varies with polymer size. While the energy stored in the $N = 10$ polymer does not significantly increase, the helix still performs a significant amount of work in transporting it. For the $N = 20$ and $N = 50$ polymers, we can see that the helix performs roughly $10k_{\mathrm{B}}T$ of work per revolution for every $1k_{\mathrm{B}}T$ energy maintained in the polymer. Because for the $N = 10$ polymer, the power is on the order of $1k_{\mathrm{B}}T$ per revolution, this predicts the mean stored energy to be much less than the its fluctuations, and hence negligible.

In general, the work excess term is typically smaller than the viscous term by ~ 4 orders of magnitude. However, this is for a solitary polymer in the vicinity of the helix. In a suspension of polymers, we hypothesise that the excess work takes the form of a sum over the work performed on each polymer and so will be proportional to the local density of the solution at least in the dilute limit where polymer–polymer interactions can be ignored. As we have shown separately, the effect of the helix is to increase the local density of polymeric material so we expect this, combined with the work done on stretching the polymers, to give rise to strongly nonlinear viscoelastic effects. This offers some contrast to the hypothesis that bacterial flagella on their own deplete their local environment of biopolymeric material and hence experience only the background Newtonian solvent [108].

5.4 Conclusions

We have showed that a rotating helical filament can accurately model the near-field fluid flow of a flagellated cell tethered to a wall, and studied the effects of this flow field on nearby polymers of various size. We have shown that long polymers are strongly attracted to the flagellum, and undergo a nonequilibrium stretching process as they are pulled towards it, and pumped along it. This implies that a dilute suspension of polymers tend to become locally concentrated in and around the flagellum rather than depleted.

We have also shown that with this increase in polymer concentration around the helix comes a requirement for the helix to expend work at a greater rate on average in order to maintain the stretched state of the polymer.

6

Polymer driven by a swimming helix

We have seen that a pinned helix has a strong influence on surrounding polymers and tends to draw them inward. In doing so, it requires extra work to be done on the system by the external forces responsible for actuation. In this chapter we will develop this model further, by allowing the helix to 'swim'.

The main physical difference between this system and the one considered previously is that a swimmer is *force-free* and therefore creates a very different flow field. It no longer pumps the fluid unidirectionally, nor is its hydrodynamic influence as long-range. Although force-free, our swimmer is nevertheless externally driven and so imparts a net torque on the fluid — unlike self-propelled cells which are both force- *and* torque-free. Our swimmer is therefore reminiscent of many recent bioinspired artificial swimmers that have been reported in the literature [26]. These include nano- and micro-scale magnetic ribbons [27, 142], as well as a millimetric model of a cell with a body and helical flagellum [143].

We will begin by showing how the helix we constructed previously can be made to swim, and we will present an analysis of its swimming speed and flow field. We will then proceed as before, focusing on the dynamics of a polymer, and the energetic interplay between the helix and the polymer.

6.1 Swimming helix

6.1.1 Force-free swimming in SD model

As we saw in Sec. 4.2.3, the velocity v, and angular velocity ω of the helix are linear functions of the total axial force f_z, and torque τ_z acting upon it externally:

$$\begin{bmatrix} v \\ \omega \end{bmatrix} = \begin{bmatrix} \mu^t & \mu^{tr} \\ \mu^{rt} & \mu^r \end{bmatrix} \begin{bmatrix} f_z \\ \tau_z \end{bmatrix} . \tag{6.1}$$

According to the model we developed in Sec. 4.2, ω and v are control parameters used for the external potential $\mathcal{H}_h(\boldsymbol{r}_i, t; v, \omega)$ that actuates the helix [Eq. (4.8)], and therefore are defined from the outset. Then, by Eq. (6.1), the total pumping force f_z, and torque τ_z take on whichever values are required to satisfy the v and ω that are demanded by this external control. For our swimmer to be force-free at a given ω we must set v to the value required to produce $f_z = 0$.

By inverting Eq. (6.1), we get:

$$\begin{bmatrix} f_z \\ \tau_z \end{bmatrix} = \frac{1}{\mu^r \mu^t - (\mu^{tr})^2} \begin{bmatrix} \mu^r & -\mu^{tr} \\ -\mu^{rt} & \mu^t \end{bmatrix} \begin{bmatrix} v \\ \omega \end{bmatrix} , \tag{6.2}$$

and from this it is easy to verify that if we were to measure μ^{tr} and μ^r, and then set $v = (\mu^{tr}/\mu^r)\omega$ from the outset, then this should yield $f_z = 0$. However, there are a number of problems with this method. Firstly, while it is possible to measure the mobility tensor coefficients (as we did in Sec. 4.4.2), the procedure is laborious and costly, and it must be done whenever we wish to change the helix parameters, such as pitch, contour length or radius. Secondly, as we have mentioned previously, the mobility relation Eq. (6.1) is a reduced relation concerning only the axial quantities; in general, off-axis forces and torques could result in this method being error prone. Thirdly — and most importantly — hydrodynamic interactions with the polymer will in general deform the helix. While these deformations are small, they will alter the helix mobility tensor, and so $v = (\mu^{tr}/\mu^r)\omega$ will not be guaranteed to remain true, especially as μ^r appears in the denominator, which from Fig. 4.4 we concluded to be very sensitive to shape deformations. It is definitely undesirable for the helix to break the force-free condition precisely when polymer–helix interactions are strongest, and so we have developed another method.

At each timestep, we calculate the axial displacement δz that needs to be applied to each particle of the helix, to ensure that axial forces on that particle due to $\mathcal{H}_h$ sum to zero. Because the external potential is harmonic, from Eq. (4.8) we can see that the axial force acting on particle i is

$$f_{z,i} = -k_h(z_i - z_i^0), \tag{6.3}$$

where z_i is the z-coordinate of particle i, and z_i^0 is its target position. This means that the total axial force on the entire helix is

$$f_z = -k_h \sum_i (z_i - z_i^0). \tag{6.4}$$

If we apply the shift $z_i^0 \to z_i^0 + \delta z$ to each helix particle, then $f_z = 0$ is guaranteed if

$$\delta z = \frac{1}{N_h} \sum_i (z_i - z_i^0). \tag{6.5}$$

In other words, while we rotate the target positions of the beads about $\hat{\boldsymbol{z}}$, we also slide them along $\hat{\boldsymbol{z}}$ in a manner that ensures $f_z = 0$ is explicitly maintained at all times, solving all three problems discussed above.

This method means that we have set ω and f_z at the outset: quantities that appear on opposite sides of the mobility relation Eq. (6.1). As a result, v and τ_z take on whatever values are required to ensure the mobility relation holds true, and these may fluctuate due to interactions with the polymer. As a bonus, this gives us the opportunity to measure how the swimming speed v may change due to these interactions.

6.1.2 Polymer-free Swimming speed

To test our model, we ran a series of simulations to measure the steady state swimming speed of the helix as a function of its geometry. Keeping the radius fixed at $R = 2\sigma$, we first varied the number of helix particles in the range $N \in [1, 200]$ at five different pitch lengths $l = 2\pi/\kappa \in \{2, 5, 8, 11, 14\}$. We also measured the swimming speed as a function of pitch length over the interval $l \in [2, 60]$ at three different contour lengths $N \in \{50, 100, 150\}$.

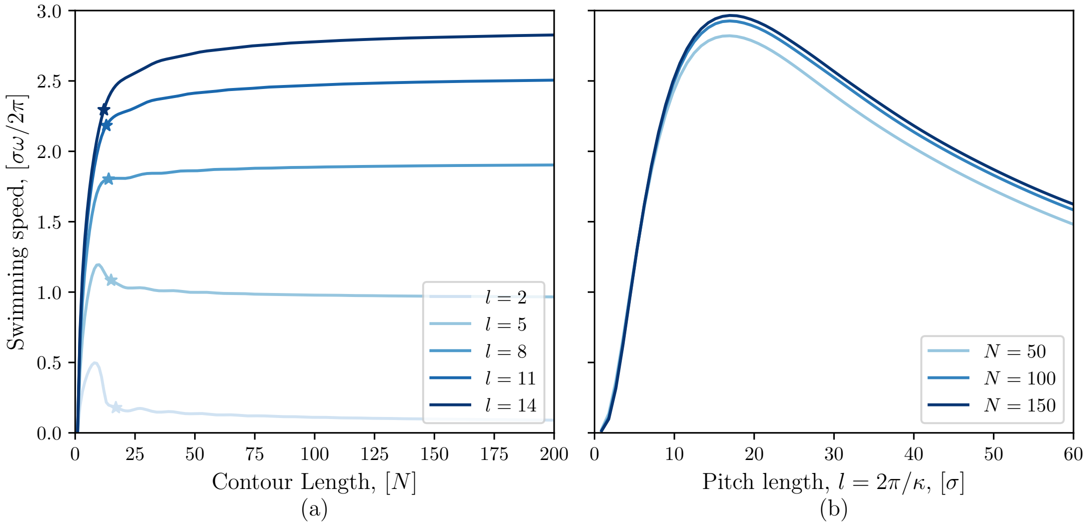

(a) (b)

Figure 6.1: Force-free swimming speed of the helix as a function of (a) the total contour length of the helix (measured in number of particles N) for different pitch lengths $l = 2\pi\sigma/\kappa$ and as a function of (b) pitch length for different contour lengths. In (a), stars ($\star$) represent the number of helix particles required to complete a turn: $N^*\sigma = \sqrt{l^2 + 4\pi^2 R^2}$. For small helices ($N < N^*$), velocities appear spurious. But as N is increased, the asymptotic swimming speed for infinitely long helices is reached reasonably quickly. In (b), we can see swimming speed is maximal at a finite pitch length $l \sim 17\sigma$, which corresponds to a pitch angle of $\vartheta = \tan^{-1}\left(\frac{2\pi R}{l}\right) \approx 36°$.

The results are presented in Fig. 6.1, where the swimming speed is shown in units of particle size σ, per period of revolution. We see in Fig. 6.1(a) that, as a function of N, the swimming speed quickly approaches an asymptotic value for each helix of different pitch length. The stars represent the the number of particles required to complete a single turn of the helix; this quantity is denoted by N^* and as a function of pitch length is given by: $N^*(l)\sigma = \sqrt{l^2 + 4\pi^2 R^2}$. We can see from the curves that for $N < N^*$, the swimming speed is strongly dependent on N. For this reason, we will concentrate mainly on much larger helices for which particle number does not influence speed appreciably.

In Fig. 6.1(b) we can see the dependence of the swimming speed on the pitch length. At low pitch length, the helix is tightly coiled, and in this limit, its geometry becomes similar to that of a cylinder, in which case we would expect motility to vanish. Indeed, as $l \to 0$, this limit is observed.

In the opposite limit, $l \to \infty$, the helix locally resembles a wire that ‘stirs’ the fluid with almost entirely perpendicular motion, and we would expect $v \to 0$ as well. This expectation is also confirmed by our measurements. We therefore observe that there is a maximum in $v(l)$ at around $l \approx 17\sigma$, which corresponds to a pitch angle of $\vartheta = \tan^{-1}\left(\frac{2\pi R}{l}\right) \approx 36°$. This agrees very well with a result by Wada & Netz (2009) who reported maximum swimming speed for a helical filament at a pitch angle of 35° [144].

6.1.3 Flow field

In Sec. 4.4.1 we saw it was possible to measure the flow field at some location $\boldsymbol{r}$ in the SD simulation by evaluating the contributions from all particles with positions $\boldsymbol{r}_i$, experiencing forces $\boldsymbol{f}_i$ through the sum: $\boldsymbol{v}(\boldsymbol{r}) = \sum_i \boldsymbol{\mu}(\boldsymbol{r} - \boldsymbol{r}_i)\boldsymbol{f}_i$, where $\boldsymbol{\mu}$ is the RPY tensor given in Eq. (4.4). In the case of a pinned helix, we could simply evaluate $\boldsymbol{v}(\boldsymbol{r})$ on a grid at each point in time in order to average over a complete revolution. However, in the case of a swimming helix, we must use a grid relative to the coordinate system of the helix.

We performed a simulation on a helix with the parameters $(R = 4, l = 15, N = 80)$, and averaged averaged over 5 complete revolutions. We decompose the flowfield into radial, axial and azimuthal components: $\boldsymbol{v} = (v_r, v_z, v_\phi)$. The axial flow v_z is the component of the flow aligned with the z-axis; the radial component v_r is the amount of flow directed into or away from the z-axis while the azimuthal flow v_ϕ is the rotational component. We measured v_ϕ in a slice of the xy-plane, and (v_z, v_r) in the zy-plane. The results are shown in Fig. 6.2, and are markedly different from the flow fields presented in Fig. 4.3 for the pinned helix.

The most striking difference between the swimming and pinned flow fields is that the lowest order contribution to the non-rotational part in the swimming case is quadrupolar (versus a stokeslet in the pinned case), and is composed of an oppositely charged pair of dipoles located at either end of the helix. The structure of (v_z, v_r) is shown in Fig. 6.2(a). The swimming direction in this image is towards the left: as the helix swims it pushes the fluid in front of it and drags the fluid behind it. This is in stark contrast with self-propelled swimmers, which being

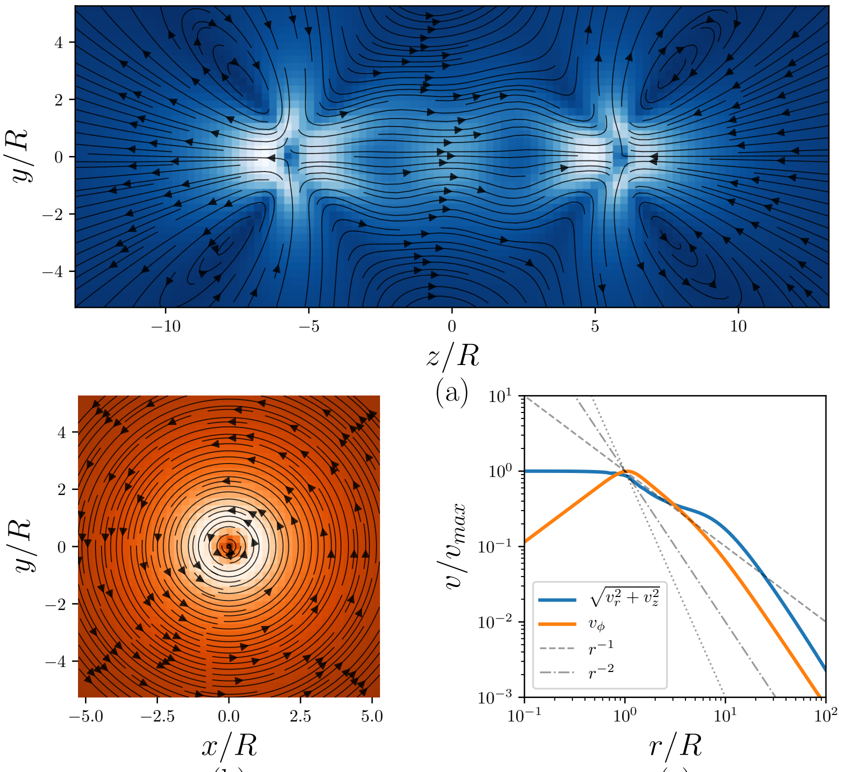

(a)

(b)

(c)

Figure 6.2: Time averaged flow fields may be decomposed into radial, azimuthal and axial flows (v_z, v_r, v_ϕ). (a) Flow field (a.u.) in the zy-plane shows axial and radial components, (v_z, v_r) while (b) flow field (a.u.) in the xy-plane shows the azimuthal component v_ϕ. Averaging was calculated by evaluating the flow field at each point of a grid centred on the helix centre-of-mass position as it swam. In (a), the swimming direction is from right to left. In both, the slices are taken through the midpoint of the helix. The azimuthal flows are due to a *rotlet*, while the axial and radial flows together give rise to a *force-quadrupole*. (c) Scaling of v_ϕ (orange) and $\sqrt{v_r^2+v_z^2}$ (blue) as a function of radial distance from the centre-of-mass location of the helix.

both force- *and* torque-free create strong dipolar fields, either 'pushing' or 'pulling' fluid in both directions as explained in Sec. 1.2.2. Additionally, there are strong radial inward flows at the front end of the helix, and outward flows at the rear. By comparison with Fig. 1.1(d) we see that the flow field is very similar in structure to the quadrupolar field generated by the pair of dipoles ($\leftarrow\!\rightarrow\ \rightarrow\!\leftarrow$).

The azimuthal flow shown in Fig. 6.2(b) is purely rotational, and strongest on a ring in xy-space corresponding to the helix radius.

To see how the fields decay in space, we measured the velocity at a series of points: $\boldsymbol{r}_i = (x_i \in [0, 100R], y = 0, z = 0)$ (i.e., a radial line originating

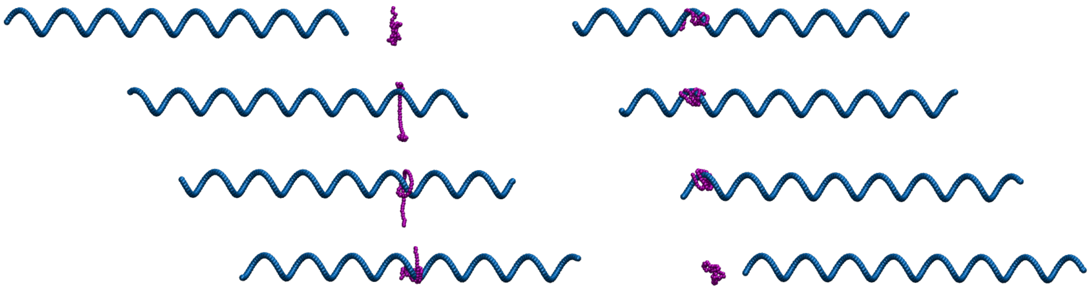

Figure 6.3: Snapshots in time of a single simulation of a helix swimming past a polymer of size $N = 50$ demonstrating polymer capture by spooling.

at the center of the helix and extending outward 100 helix radii away). These velocities are plotted in Fig. 6.2(c).

Within the helix itself ($r < R$), we observe the same qualitative flow as in the case of the pinned helix [Fig. 4.3(d)]: the axial flow is uniform, and the azimuthal flow displays rigid rotation ($v_\phi \propto r$). Near the helix on its exterior ($R < r \lesssim 3R$), both velocities scale as $1/r$, characteristic of a stokeslet. As before, this is due to the fact that the forces acting on the nearest elements of the helix dominate over those acting on the opposite side.

At larger distances, both fields decay as $1/r^2$. This is expected for v_ϕ, as the helix imparts a net torque on the fluid, thereby creating a rotlet. However this is anomalous for the quadrupolar axial–radial field, and implies that the apparently opposite charged dipoles are not of the same magnitude and so do not cancel out entirely, imparting a net dipolar flow with a $1/r^2$ scaling. Such asymmetric pairs of dipoles can occur due to asymmetries in shape; for instance, the body–flagellum asymmetry of swimming cells gives rise to two offset dipoles of differing magnitude [30].

6.2 Polymer capture

We conducted the same simulations as described in Sec. 5.2 but with the modification to our model that allows the helix to swim. In each simulation we initialised a polymer at a random location on a disc ‘in front’ the helix, allowing a gap of approximately $\sim 15\sigma$ and computed for approximately 40 full rotations of the helix, which in all cases was enough time for the helix to swim completely past the polymer. We conducted 200 simulations for each size of polymer $N \in \{1, 10, 30, 50\}$ and tracked the positions of all particles, allowing us to build up a statistical picture of the polymer–helix interaction.

Snapshots in time of a single capturing process are shown in Fig. 6.3. Remarkably, the polymer capture process that we described for the pinned helix is observed to also occur for the swimming helix. The qualitative behaviour we observe is very similar: long polymers will become stretched out, and orbit around the helix as it swims past, often becoming captured in a similar manner as before. The helix then spools the polymer which winds around the helix. The primary difference that we observe in this case, however, is that this progresses in the absence of any net pumping, i.e., the polymer is not appreciably transported along $\hat{\boldsymbol{z}}$. We notice that when large polymers become captured by a swimming helix, they often coil tightly around the helix as shown in Fig. 6.3 which contrasts with the more elongated, and looser coiling observed for the case of a pinned helix (e.g., Fig. 5.2). We attribute this to the fact that the polymers are not being pumped or dragged through the fluid and therefore are able to tightly wind around the helix.

From Fig. 6.4, it is apparent that the statistical nature of this process is somewhat different to the pinned case in the previous chapter. Firstly, the effect is less pronounced than that reported in the previous chapter (Fig. 5.3); for $N = 30$ and $N = 50$ polymers, smaller fractions are captured than by the pinned helix, while for $N = 10$ we observe the swimming helix to have little effect on the polymer density as it swims past.

Secondly, for the tracer particles ($N = 1$), we observe a moderate tendency for the density to go down in the $r < R$ region. We can also see that this depletion occurs in the first quarter of the simulation time, therefore the outward radial flows at the rear end of the helix cannot be responsible for it. Tracer particles in our simulation experience only thermal forces and the helix flow field. In a purely rotational flow, uniformly distributed thermal forces will result in a greater

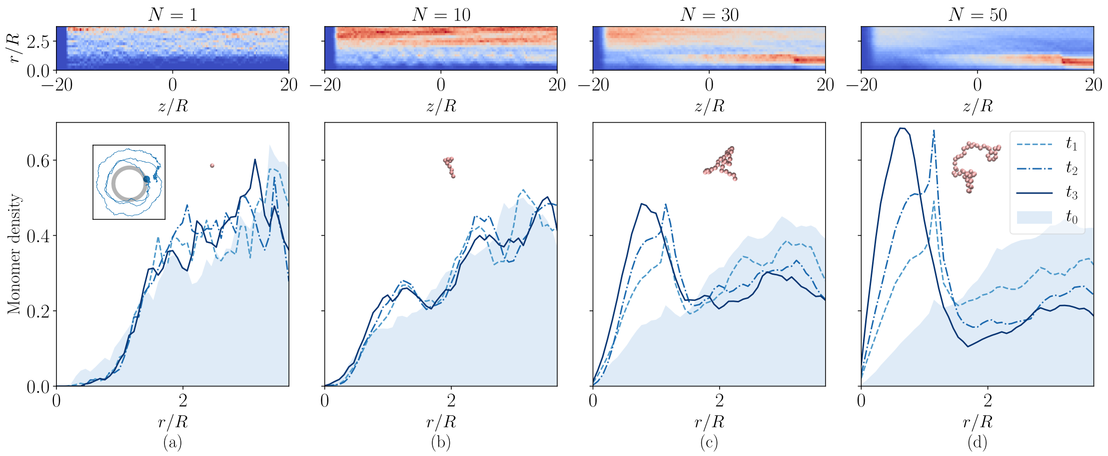

(a) (b) (c) (d)

Figure 6.4: Polymer distributions due to swimming helix averaged over 200 simulations for polymers of size (a) $N = 1$ (monomers), (b) $N = 10$, (c) $N = 30$ and (d) $N = 50$. Upper images show 2-dimensional histograms of all polymeric particle (r, z)-positions in cylindrical co-ordinates relative to the helix centre-of-mass, integrated over all time. Lower graphs show 1-dimensional histograms of radial positions r, averaged over four contiguous quarters of each simulation —i.e., total period, $\mathcal{T} = t_0 \cup t_1 \cup t_2 \cup t_3$. First-quarter distributions (including the initial distributions) are highlighted by the shaded region. (a) Inset: a single monomer ($N = 1$) trajectory in the xy-plane starting from the blue marker shows clockwise orbiting around the helix (shaded region) with a net radial drift.

number of Brownian displacements taking the particle to a larger radial distance, than to a shorter one. While the flow in this case is not purely rotational, the dominant contribution is rotational (due to the rotlet created by the net torque on the helix), and so we observe tracer particles initially placed near the z-axis spiralling outwards as the helix swims past. An example of such a trajectory is shown in the inset of Fig. 6.4(a).

6.3 Fluctuating work

In the simulations presented in Chapter 5, we also measured the cumulative work performed by the helix, $w(t)$, using Eq. (5.2), and the potential energy stored in the polymer, $\mathcal{H}(t)$; here we compare similar results for the swimming helix. As before, we measure the work expended by a helix in the absence of a polymer, $w_0(t)$, and subtract this from the work measured in the presence of a polymer to obtain the *excess* work: $w_{\text{ex}}(t) = w(t) - w_0(t)$. Similarly, to measure the change in polymer energy, we calculate $\mathcal{H}_{\mathrm{WCA}} + \mathcal{H}_{\mathrm{Fene}}$ and subtract the initial 'ground state' energy at $t = 0$.

Figure 6.5(a-c) shows each of the $w_{\mathrm{ex}}(t)$ trajectories obtained in the presence of polymers of size $N \in \{10, 30, 50\}$. There are a number of qualitative differences between the curves obtained for a swimming helix, and the curves plotted in Fig. 5.4(a-c) for the pinned helix. Firstly, for the pinned helix, the terminal values $w_{\mathrm{ex}}(\mathcal{T})$ were always strictly positive: the helix always did a net positive amount of excess work on a polymer. However, in Fig. 6.5(a-c), the $w_{\mathrm{ex}}(\mathcal{T})$ are distributed across both positive and negative values, meaning that there were simulations in which the helix had to do *less work* than it would have had to do without the polymer present.

Secondly, the structure of the excess work trajectories in the $N = 10$ case are also different. For a swimming helix, there are a few trajectories in which a large amount of work is done on these smaller polymers at the very beginning of their interaction. After these jumps in w_{ex}, the work plateaus out noisily, and sometimes declines.

The mean excess power $\dot{w}_{\mathrm{ex}}(t)$ is computed by smoothing the difference vector $\Delta w_{\mathrm{ex}}(t) = w_{\mathrm{ex}}(t + \Delta t) - w_{\mathrm{ex}}(t)$ using a Savitzky–Golay filter with a window size of $\sim 1/4$ helix revolutions, and then averaging over all simulations. The same smoothing and averaging procedure was used on the polymer energies $\mathcal{H}$. These are plotted in Figs. 6.5(d-f).

There are again a number of differences between these quantities and their equivalents for the pinned helix case. For the $N = 10$ polymer, our observation of large jumps in w_{ex} is borne out by a prominent peak in $\mathcal{H}$ at early times. On average, these small polymers become more stretched near the beginning of their interaction with the helix, before relaxing to a lower energy for the remainder of the interaction. This corresponds to a sharp peak in $\dot{w}_{\mathrm{ex}}$ at $t \approx 5(2\pi/\omega)$. For the $N = 30$ polymer, we observe a similar initial-interaction peak in $\mathcal{H}$, which gradually decays, and this is accompanied by a sharp peak in $\dot{w}_{\mathrm{ex}}$ similar to that observed for the $N = 10$ polymer. For the largest polymer, however, $\mathcal{H}$ is much smoother and does not exhibit a peak at early times. However, a sharp peak is observed in

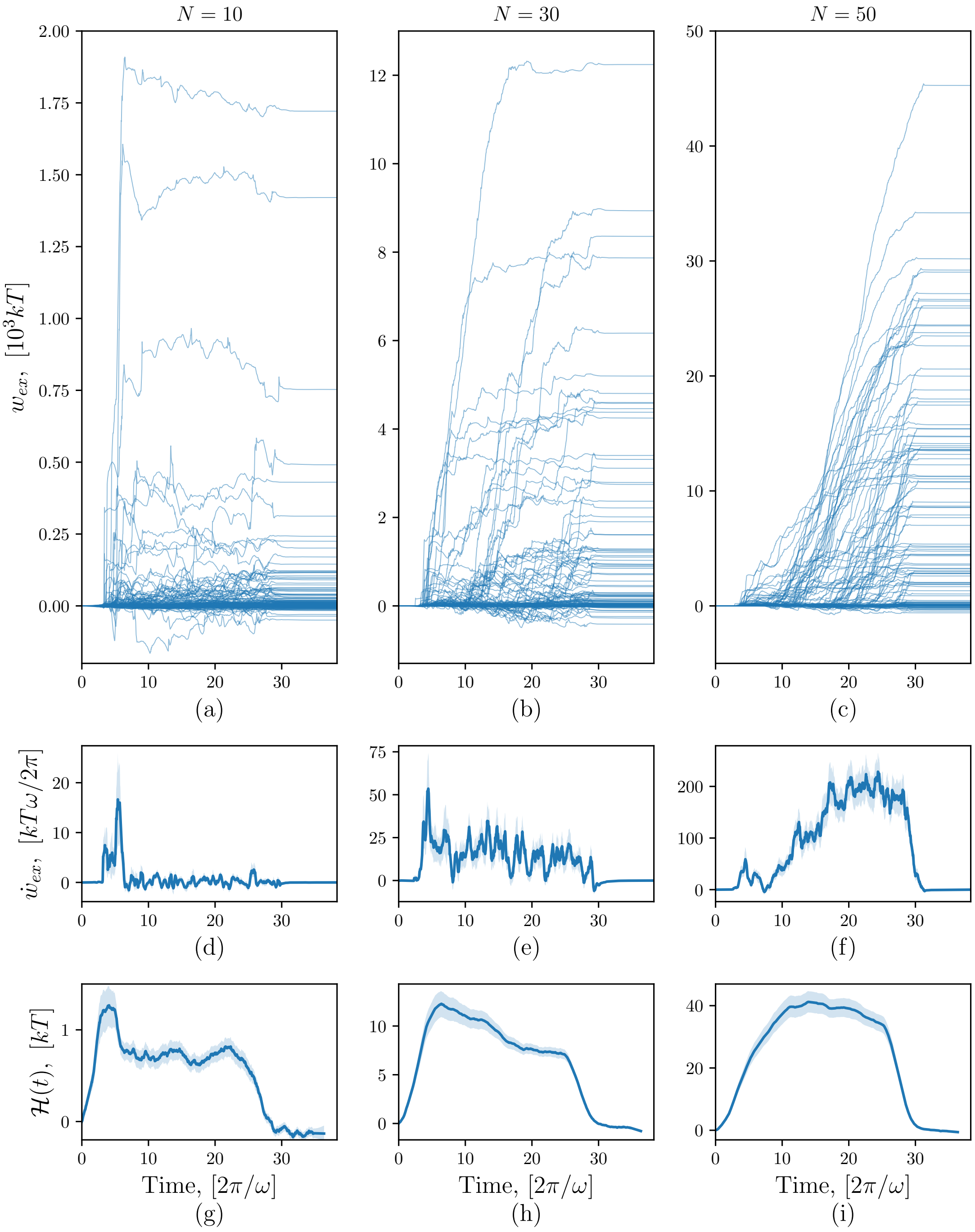

Figure 6.5: (a-c) Stochastic excess work performed by a swimming helix in the presence of polymers of size $N = (10, 30, 50)$. 200 simulations were performed for each case. (d-f) Mean excess power per revolution, averaged over 200 simulations. For each timestep, $\mathrm{d}w_{ex}$ was calculated and smoothed with a window size $\sim 1/4$ revolution. The shaded region corresponds to the standard error on the mean. (g-i) Mean increase in polymer energy calculated using the potentials $\mathcal{H}_{\text{repel}}$ and $\mathcal{H}_{\text{bond}}$ with the same smoothing and averaging procedure employed in (d-f).

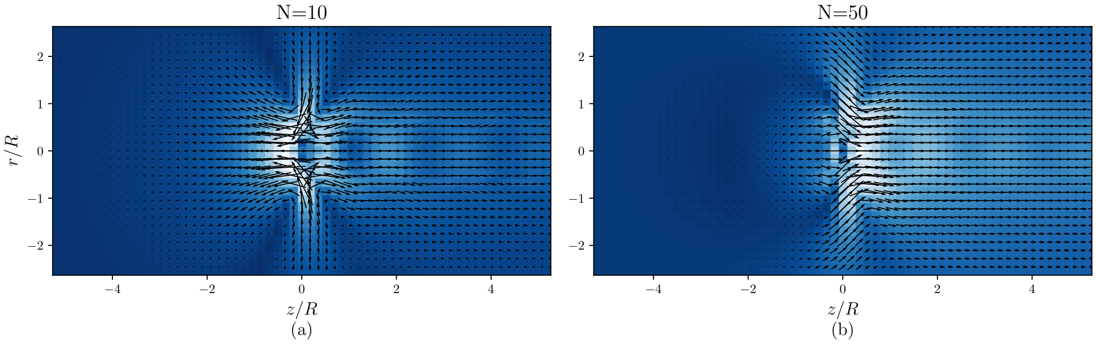

(a) (b)

Figure 6.6: Flow field at the point of collision of a swimming helix with polymers of size (a) $N = 10$, and (b) $N = 50$. For the smaller polymers, the flow field resembles the unperturbed field shown in Fig. 6.2(a) with a strong extensile dipole at the front of the helix. However, the larger polymers provide screening which smooths out the dipole. The helix swims to the left in both cases.

the helix power at around $5(2\pi/\omega)$ which has a very similar shape and magnitude as the sharp peak in power for the other $N = 10$ and $N = 30$ polymers.

For the pinned helix, we observed the approximate relationship $|\dot{w}_{\text{ex}}| \sim 10|\mathcal{H}|$. However, for the swimming helix we observe this relationship to be different: $|\dot{w}_{\text{ex}}| \sim 5|\mathcal{H}|$. This can be explained by noting that the swimming helix transports the polymer across a larger distance in $\hat{\boldsymbol{z}}$. The viscous drag acting on the polymer is an extra source of dissipation that the pinned helix must overcome by performing more work.

All three data sets contain trajectories where the power output sharply jumps at approximately $t = 5$ helix-rotations. These correspond to simulations in which the polymers' initial locations are directly in front of the helix, and the jump in power occurs when the front of the helix and the polymer begin to interact. However, only the smallest polymer displays a discrete jump in its internal energy (hence exhibits strong stretching) at the early stage of interaction. This can be explained by considering the flow field directly in front of the helix, shown in Fig. 6.2(a), which is characterised by strongly extensile dipolar flows. As this region reaches the polymer, there will be a sharp stretching in the polymer localised at the point of inflection of the flow field, and we hypothesise that this stretching causes the jump in power output required from the helix.

This mirrors the argument proposed by Shen and Arratia that the swimming of *C. elegans* is hindered by polymer stretching at highly localised points of strong extensile flow [98]. However, it raises the question of why this occurs only for the smallest polymer, rather than the larger ones. Our explanation for this is due to the self-screening effect that the larger polymers provide to fluid within their influence. To test this hypothesis we measured the flow field due to both the forces on the helix particles as well as those on the polymer particles at the point where the polymers 'enter' the helix (i.e., the point in time where the polymers' centres-of-mass pass through the dipolar region of the free flow in Fig. 6.2(a)). These fields are shown in Fig. 6.6. In the coordinates of these figures, $z = 0$ corresponds to the location of both the centre-of-mass of the polymers, and the front-most bead of the helix; the helix is swimming towards the left in both cases.

By way of comparison to the polymer-free flow fields, we observe that in (a) the flow field is unperturbed in comparison, and still bears the strongly extensile dipolar flow which passes through the polymer. However, in (b), the presence of the polymer provides hydrodynamic screening which smooths out the dipole. This provides evidence towards our hypothesis that it is the extensile dipolar field which noticeably stretches the small polymers as they pass through it.

6.4 Swimming speed

As our model allows the helix velocity to fluctuate in response to changes in the helix mobility that might occur due to the polymer, our next goal is to check this hypothesis by seeing if there is a dip in the swimming speed as a result of the polymer stretching effect.

6.4.1 Varying polymer size

We define the helix swimming speed at each timestep as the z-displacement of the centre-of-mass of the helix particles: $v(t) = \frac{1}{N\Delta t}\sum_i \Delta z_i(t)$. This is a highly fluctuating quantity, which we plot for each simulation in Fig. 6.7 together with the mean computed across all simulations for each value of N.

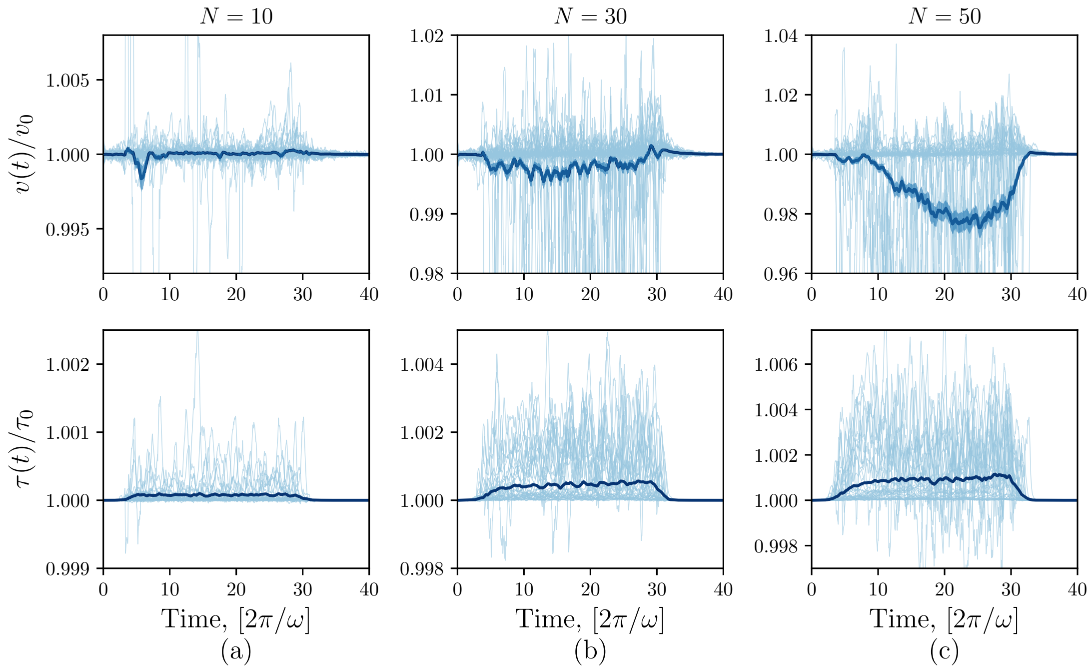

Figure 6.7: Speed change relative to free swimming speed, $v(t)/v_0$ (Top), and torque change relative to free steady state torque $\tau(t)/\tau_0$ (Bottom) for helices swimming in the presence of polymers of size (a) $N = 10$, (b) $N = 30$, (c) $N = 50$. Decrease in swimming velocity and increase in torque implies changes the helix mobility tensor due to interactions with polymers. For better clarity only 1-in-5 trajectories are plotted.

The result is that the mean velocity of the helix *decreases* in the presence of a polymer. There appear to be two noticeable types of retardation. The first manifests as a sustained drop in swimming speed observed in the presence of the two larger lengths of polymer. This mean speed decrease is on the order of 2% for the $N = 50$ polymer, and around 0.5% for the next largest $N = 30$ polymer. The second type of retardation appears as the brief drop of around 0.02% in swimming speed observed for the $N = 10$ polymer around $t = 5$ helix-rotations. We do not observe a sustained drop in velocity in this case. This second type of hindrance provides evidence for the hypothesis of Shen and Arratia that polymers in local regions of strong extensile flow are able to cause a noticeable slow-down in the swimming of the cell which creates that flow [98]. However, we do not observe this so clearly for the larger polymers because the sustained retardation they cause dominates over this effect.

In Fig. 6.7(c), one apparent feature of the mean velocity is the gradual nature of its decline, reaching a minimum around 25 helix-rotations. This time corresponds roughly to the top right image in Fig. 6.3, after which the polymer has become tightly wound around the helix. We draw from this the conclusion that the mechanism for retardation is the increase in drag on the helix that occurs as the polymer is gradually wound around it.

In addition to the helix velocity, we also measured the axial component of the torque acting on the helix by computing $\tau_z = \sum_i (x_i f_{y,i} - y_i f_{x,i})$ at each point in time, normalising this by dividing through by the polymer-free, steady-state torque τ_0. The trajectories $\tau_z(t)/\tau_0$ were smoothed and averaged using the same procedure as before, and the results are plotted in Fig. 6.7(d-f). In each case, the torque increase due to the presence of the polymer is positive and sustained for the entire time the polymer is passing the helix. However, the percentage changes for each N are much smaller than the changes in speed: ranging from 0.1% for the largest to 0.01% for the smallest polymers. Additionally, the functional forms of the torque curves do not appear to correlate with those of the speed changes.

To consider why this is the case, we must return to the mobility relation Eq. (6.1). As in these simulations, $f_z = 0$ is maintained by construction, the mobility relations become

$$v = \mu^{tr} \tau_z, \tag{6.6}$$

$$\omega = \mu^{r} \tau_z. \tag{6.7}$$

The quantities which are fundamentally changing as a function of the systems configuration are the mobility tensor coefficients, μ^{tr} and μ^{t}. This is because these coefficients result from hydrodynamic interactions with the environment; for example, other obstacles like nearby spheres or walls would also change the mobility tensor of the helix. Therefore, as ω is kept constant and $f_z = 0$, the observed quantities τ_z and v must be changing due to changes in the helix mobility.

In particular, constant ω implies $\tau_z \sim 1/\mu^r$. This in turn implies that $v \sim \mu^{tr}/\mu^r$. This means that while the mobility coefficients might both go down in the presence of polymers, the swimming speed of a helix might still go up, depending on the relative scaling of the mobility coefficients.

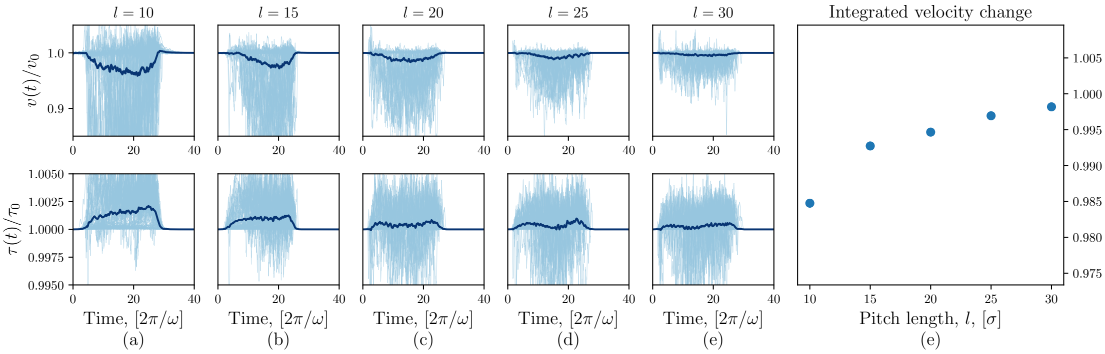

Figure 6.8: (a-e) Speed change relative to free swimming speed, $v(t)/v_0$ (Top), and torque change relative to free steady state torque $\tau(t)/\tau_0$ (Bottom) for helices of varying pitch length (a) $l = 10$, (b) $l = 15$, (c) $l = 20$, (d) $l = 25$ and (e) $l = 30$. (f) Integrated mean velocity change $\int v(t)/v(0)\mathrm{d}t$, i.e., the mean displacement over a complete simulation relative to an unhindered helix.

In the particular case of the helix we have studied in this chapter, we have observed that v decreases, which implies that for this helix geometry at least, μ^{tr} decreases faster than μ^{r}. It is not obvious, however, that this must be the case for any helical swimmer. Changing the helix parameters such as κ, and R might result in an *increase* in μ^{tr}/μ^{r}. Similarly, the quantity μ^{tr}/μ^{r} in the presence of a polymer might change as a function of ω as a competition between helix rotation period, and polymer relaxation time alter the Deborah number of the system.

6.4.2 The effect of helix geometry

To test whether or not helix pitch length has a qualitative effect on the scaling of quantity μ^{tr}/μ^{r} with and without a polymer, we conducted similar experiments as above, varying only the pitch length. The results for speed change, and torque change are plotted in Fig. 6.8(a-e) for pitch lengths in the range $l \in [10, 30]$.

We observe that the helix slows down on average for all pitch lengths. We calculated the integrated velocity change $\int(v_0 - v(t))\mathrm{d}t$ and plot this quantity as a function of pitch length in Fig. 6.8(e). We can see that helices with smaller pitch lengths are affected more by a *single* polymer and hypothesise that this is because that as l increases, the hydrodynamic influence the polymer has on the helix decreases as the helix gets longer.

6.5 Conclusions

We constructed a Stokesian dynamics model of a force-free swimming helix and measured its time-averaged flow field. We simulated its interaction with polymers of different size, showing that large nearby polymers are captured by it as it swims past. We observe a spooling process whereby one end of a polymer becomes entrained by the rotating flow field, and wraps around the helical filament. As the helix continues to swim, it winds in the polymer around it until it is tightly coiled around the helix. We also showed that the opposite is true for traces: diffusion in a rotlet field leads to a net radial drift away from the axis of the helix.

Analysing the work done by the helix, we found that similarly to the previous chapter, the helix tends to do a positive amount of extra work in the presence of a polymer, though some instances of negative work were observed. As in the previous chapter this extra work is done in order to maintain the nonequilibrium state of the polymer which we have also shown to remain stretched as the helix swims past.

We also observed the novel effect of a spike in the energy stored by small polymers as they pass through the front of the helix, which wasn't observed for larger polymers. We hypothesised that this was due to localised stretching in the polymer as it passes through the region of high extensile flow created by the front of the helix; in our hypothesis, self-screening of the flow field by larger polymers meant they do not experience this extensile flow. By averaging over the flow fields from many simulations we showed that this is indeed the case.

7

Passive colloids inducing active flow

In the preceding chapters we have studied externally activated particles immersed in passive fluids. In this chapter we will turn the tables and ask how a confined active fluid responds to the inclusion of a passive particle. The system we study is a 3-dimensional square channel in which a weakly active fluid may be induced to transition into a global state of coherent, directed flow by the presence of a spherical colloid. We show that when no colloid is present and activity is low, defects will be absorbed at the walls and the fluid will decay to a stable quiescent state; if a colloid is present it acts as a motile defect that cannot be removed but instead imparts its motion on the fluid generating flows which spread globally across the system. The resulting flow advects the colloid with it, transporting it along the channel in a robust and time-stationary manner. The fact that the flow is induced by the colloid itself is highly novel and hints at the possibility for selective transport mechanisms for passive colloidal payloads in active biological fluids.

7.1 Background

The unifying feature of active matter is the microscopic generation of energy by the constituent particles within the bulk of the system. Under the right conditions, active systems are capable of demonstrating complex feats of self-organisation such as the well-studied phenomena of flocking and ordering. However, the exact nature of these 'right conditions' is currently the focus of intense study as many biological processes, such as cell motility [8], tissue growth [145], development [146], and collective behaviour [9], are thought to be described by the fundamental physics of active matter. Additionally, understanding how chemical energy may be harnessed and put to mechanical work would prove to be a tremendous advance in the field of microfluidics and nanomachine design [147, 148].

Biological active fluids often comprise rod-like particles such as bacteria, actomyosin proteins or microtubules; their pairwise interactions can give rise to large-scale nematic alignment in dense solutions [9]. However, unlike passive nematics such as liquid crystals, their intrinsic activity causes an instability in global ordering, leading to large-scale turbulent flows [149]. Understanding the nature of these flows can be a challenge due to their highly nonlinear and nonequilibrium dynamics.

It has been shown that geometrical confinement can tame the turbulent nature of an active fluid, leading instead to the spontaneous formation of coherent, unidirectional flow in a channel, or the suppression of flow altogether. Voituriez *et al.* (2005) were the first to show that a weakly active nematic gel in a 2-dimensional channel displays a transition from a quiescent state to a coherent flow state [150]. They found that anchoring of the nematic director at the wall was required for this effect to be observed, and that the critical activity or channel height depends on the nature of these boundary conditions. Their analytical results were confirmed numerically by Marenduzzo *et al.* (2007) using a lattice Boltzmann approach to solve the nematohydrodynamic equations of motion which we presented in Sec. 1.3 [151, 152]. Marenduzzo *et al.* (2008) also studied the role of wall anchoring and found that a passive–active transition occurs at a critical activity $\zeta_c > 0$ when both walls have normal anchoring, while contrasting planar–normal anchoring on the walls led to spontaneous flow at any activity (i.e. $\zeta_c = 0$) [153]. Edwards & Yeomans (2009) mapped the full phase space for this system [154]. Theillard *et al.* (2017) further explored the idea of geometric confinement controlling the phase of active fluids by showing numerically that an active fluid in a 2-dimensional circular domain transitions from a quiescent state to a stable vortex, and then to turbulent behaviour [155].

These effects have also been seen experimentally. Woodhouse & Goldstein (2012), and later Wioland *et al.* (2013), demonstrated that when bacteria are confined to a circular domain, they spontaneously form a rotating vortex [156, 157]. Bricard *et al.* (2013) showed that motile colloids could similarly be made to self-organise into a collective flock that would undergo unidirectional flow around a circuit-like channel [43]. Most recently, Wu *et al.* (2017) have reported observing a transition from turbulent to coherent flow in a confined solution of microtubules and kinesin molecular motors [158]. It is striking that these results appear for as diverse a range of particles as bacteria, artificial colloids, and molecular-scale microtubules, giving evidence for the universal nature of the underlying physics. Interestingly, the experiment on the microtubule fluid demonstrated that the transition between turbulent and coherent flow was governed by the length-scales of the confining geometry, rather than any intrinsic length-scale of the fluid itself. In addition to turbulence and coherent flow, other phases that have been observed include ones characterised by the periodic ordering of topological defects in a vortex lattice, and oscillatory flows [159–161].

As active fluids are able to internally generate flow, a pertinent question to ask is how activity may be harnessed to generate mechanical work on the microscopic level: for instance by the actuation of a small rotor or transport of a passive colloid. It has already been shown that in the unconfined turbulent phase, the chaotic motion of an *E. coli* suspension can be rectified into uniform rotation by asymmetric ‘ratchet’ rotors [162, 163], or into the undirectional transport of similarly asymmetric wedge-shaped particles [164, 165]. However, these systems are often noisy and transport of the payload progresses at a much slower rate than the swimming speed of the active particles.

By contrast, in the coherent flow phase, an active fluid flows at a rate comparable to the ballistic speed of its constituents. Additionally, the experiments of Wu *et al.* demonstrated that coherent flow can be achieved in ‘race track’ channels of arbitrary length and shape [158]. These two observations coupled together offer a glimpse of the possibility of fast and directed colloid transport through complex microfluidic geometries, and this motivates us to study the effects of placing a colloid in a confined active nematic fluid.

In this chapter, we show that in a 3-dimensional channel, the presence of a colloid is able to induce a global active flow state in a weakly active, extensile fluid which would otherwise settle into a quiescent state. The resulting flow advects the colloid along with it, transporting it along the channel in a robust and time-stationary manner.

7.2 Methods

Hybdird lattice-Boltzmann

In Sec. 1.3 we showed how the dynamics of an active nematic fluid could be modelled by a set of continuum equations which describe the evolution of the flow field, $\boldsymbol{v}$, and nematic tensor order parameter, $\mathbf{Q}$. Solving these equations is a challenging task, and while analytic progress may be made in simple cases [150], solving 3-dimensional flows in arbitrary geometries usually requires numerical solution [166].

We adopt a hybrid lattice Boltzmann method first developed by Marenduzzo *et al.* [152] and incorporated into a multipurpose parallel lattice Boltzmann solver which we use for the simulations in this chapter [167]. In this hybrid method, the hydrodynamic equations are solved via standard lattice Boltzmann methods, while the dynamics of the order parameter is calculated using a finite difference scheme.

Boundary conditions

Our channel consists of four solid walls of length L, arranged to form a channel with a square cross-section of side-length d. Periodic boundary conditions are imposed at the ends of the channel giving the system an annular topology. No-slip boundary conditions for $\boldsymbol{v}$ are imposed on the channel walls and colloid surface. Boundary conditions for $\mathbf{Q}$ are more complicated: a term added to the free energy can favour tangential or normal alignment of the director field on the colloid surface, and these

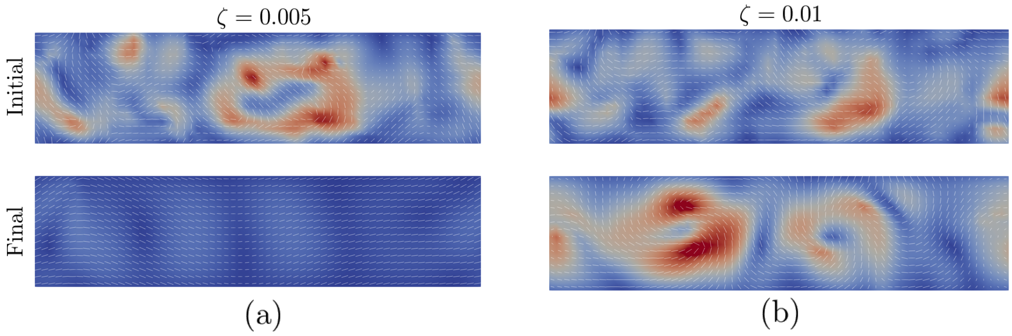

(a) (b)

Figure 7.1: Profiles of channel containing an extensile active fluid with no colloid present. (a) At low activity an initial perturbed state decays into a quiescent final state after a transient period, and (b) at high activity, the system is unstable to the formation of active turbulence characterised by spontaneous flows which continually arise and dissipate. Heatmaps: magnitude of velocity ranging from $|\boldsymbol{v}| = 0$ (dark blue) to $|\boldsymbol{v}| \sim \mathcal{O}(10^{-3})$ (red) in simulation units. Lines: director field $\hat{\boldsymbol{n}}$.

are termed planar and normal anchoring respectively. We apply free-boundary conditions on the channel walls (no anchoring), but explore the effects of all three anchoring conditions (planar, normal, and none) on the colloid. The strength of the anchoring is given by the parameter w.

In all simulations, we initialise the fields $(\boldsymbol{v}, \mathbf{Q})$ in a random, agitated state and allow the system to evolve naturally.

7.3 Results

Before describing our main result for a colloid in an active fluid, we first study the case where no colloid is present, and the case of a colloid present in a passive liquid crystal.

7.3.1 Active fluid with no colloid

We first consider the case of an active fluid confined to a 3-dimensional channel of length $L = 64$ with a square profile of width $d = 16$. We initialise the fluid in a perturbed state with a randomised director and velocity fields. From this perturbed state, the system evolves to a final steady state which we characterise using two different order parameters. First, to measure the characteristic strength of the flow in the system, we consider the root-mean-square velocity normalised

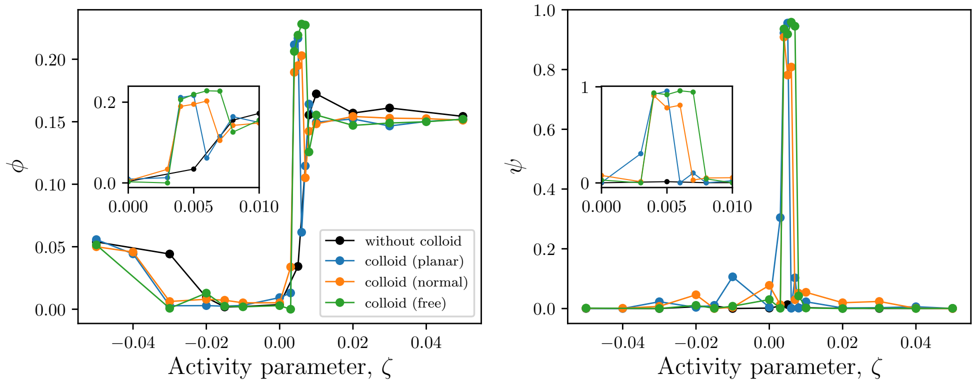

(a) (b)

Figure 7.2: Characterising the phase behaviour of an active fluid with and without a colloid in the channel as a function of activity. (a) Flow strength order parameter, $\phi = \sqrt{\langle \boldsymbol{u} \cdot \boldsymbol{u} \rangle}/(|\zeta| + \varepsilon)$, measures the characteristic strength of active flows present in the final steady state. (b) Flow coherence order parameter, $\psi = \left\langle \frac{v_x}{|\boldsymbol{v}|^2} \right\rangle$, measures the degree of flow along the long-axis of the channel. These two figures together determine that only a transition between quiescence and turbulence is observed. At no activity is spontaneous coherent flow observed.

by activity with a regularisation parameter $\varepsilon = 0.001$:

$$\phi = \frac{\sqrt{\langle \boldsymbol{v} \cdot \boldsymbol{v} \rangle}}{|\zeta| + \varepsilon}. \tag{7.1}$$

This order parameter should be 0 for a quiescent fluid, and finite otherwise. In the turbulent phase we should observe $\phi(\zeta) \sim$ *const.* as the root-mean-square velocity in this phase should be proportional to activity, as shown by Thampi *et al.* (2013) [168]. To differentiate between turbulent and coherent flow, we require another order parameter that measures the degree of flow along the axis of the channel,

$$\psi = \left\langle \frac{v_x}{|\boldsymbol{v}|^2} \right\rangle, \tag{7.2}$$

which will be close to 1 in the coherent flow phase, and 0 otherwise. This is the same as the order parameter used by Wu *et al.* (2017) to measure the coherence of the flow they observe in their channel [158].

We consider a fluid in the nematic phase, with $\gamma = 3.2$ (which is greater than the isotropic–nematic transition point $\gamma_T = 3.0$), and in the flow-aligning regime ($\xi = 0.7$).

Scanning through a range of activities $\zeta \in [-0.05, 0.05]$, we observe that only two phases are realised by the fluid: either the system relaxes to a quiescent low-$|\zeta|$ phase characterised by $\phi \to 0$, or a turbulent phase characterised by a finite ϕ and $\psi = 0$. For an extensile fluid, we observe that this transition occurs at $\zeta = 0.008$, and for a contractile fluid it occurs between $-0.03 < \zeta < 0.02$. These two phases can be seen in Fig. 7.1 which shows the initial and final states plotted for an extensile fluid with activities above and below the transition point. The full results for (ϕ, ψ) of the colloid-free fluid are shown by the black lines in Fig. 7.2 across the full range of activities. In Fig. 7.2(a), there is a crossover from quiescence to turbulence in the range $\zeta \in [0.005, 0.01]$, in which $\phi(\zeta)$ grows linearly. In Fig. 7.2(b), we see that the direction of the flow remains disordered across as $\psi(\zeta) = 0$ across the whole range tested.

7.3.2 Colloid in a passive liquid crystal

In a passive liquid crystal, a system in an initially perturbed state will have a nonzero molecular field $\mathbf{H}$, and by Eqs. (1.13) it will relax towards an equilibrium state that minimises the free energy, $\mathcal{F}$, given by Eq. (1.16). The elastic term in the free energy, $\kappa \mathrm{Tr}\,[(\nabla \mathbf{Q})^2]$, penalises gradients in $\mathbf{Q}$. However, as mentioned in Sec.1.3, the inclusion of a spherical colloid with either parallel or normal boundary conditions frustrates the nematic, as it does not allow the liquid crystal to reach a state of global alignment in which gradients vanish. We would like to understand what the equilibrium state is in this case.

We ran simulations of a passive liquid crystal ($\zeta = 0$) with the same properties as before, in a channel (dimensions $16 \times 16 \times 64$) with a colloid of radius $R = 4$ initialised in the centre $(8, 8, 32)$. We studied three different colloids: one with enforced planar anchoring on its surface ($w = 0.04$), one with normal anchoring ($w = 0.04$), and a 'free' colloid with no boundary condition on its surface. As before, no anchoring condition was imposed on the walls of the channel. Cross-sectional slices of the channel centred on the colloid in its final state are shown in Fig. 7.3.

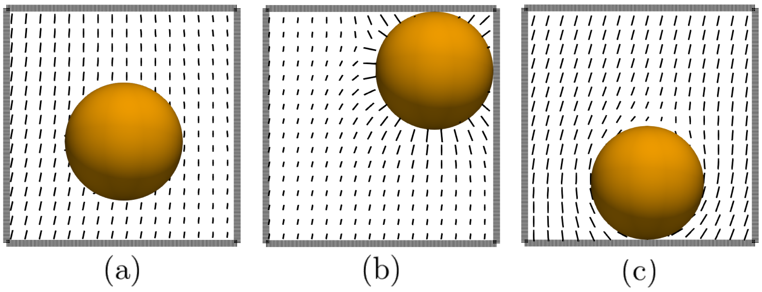

Figure 7.3: Cross-sectional view of a colloid in a passive liquid crystal in a channel with free boundary conditions at the walls (no anchoring). The final equilibrium states depend on the anchoring conditions on the colloid: (a) no anchoring, (b), normal anchoring, or (c) planar anchoring.

We observe three possible cases. When no anchoring condition is imposed on the colloid surface, it is essentially decoupled from $\mathbf{Q}$ as it imposes no gradients in its immediate vicinity. When boundary conditions are applied, however, the system minimises its free energy by attracting the colloid towards the walls of the channel. In the case of normal anchoring, the colloid is attracted to the corner, while with parallel anchoring it is attracted to just one wall.

The wall attraction occurs because no boundary condition is imposed at the wall itself. High gradients are necessarily imposed in the volume surrounding the colloid, therefore the free energy can be reduced by ensuring that some of this volume lies outside the liquid domain, which happens when the colloid is flush with the wall. Normal anchoring imposes high gradients in $\mathbf{Q}$ isotropically, and so the colloid is attracted to walls in all directions, eventually finding its energy minimum in a corner. Parallel anchoring, by contrast, imposes strong gradients around antipodal points that line up along the far-field director. Hence the elastic forces felt by such a colloid are mainly felt along this axis, so it is attracted to one wall only.

7.3.3 Colloid in active liquid crystal

As described in Sec. 7.3.1 we observed the extensile active fluid to transition from a quiescent state to a turbulent state at $\zeta \approx 0.08$. Placing a colloid in the fluid changes this picture dramatically. As before, we studied colloids with three different anchoring conditions: planar, normal (both with anchoring strength $w = 0.04$), and

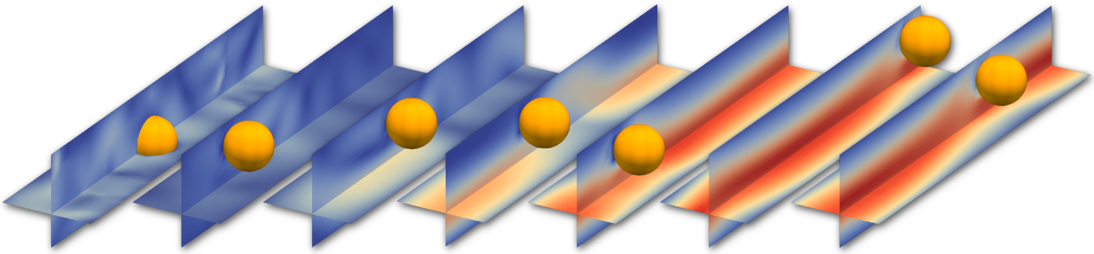

Figure 7.4: Onset of coherent flow shown through a sequence of slices through the centre-line of the channel. Each panel is separated by roughly 2×10^4 simulation steps. Between the first two panels, the colloid is attracted to the corner in the upper-right quadrant of the channel. Between panels 3 and 4, the onset of coherent flow is triggered by a system-spanning transient flow. Between panels 5 and 6, the colloid crosses the periodic boundary of the domain.

free anchoring ($w = 0$). In each case the qualitative behaviour is the same: between the high-ζ turbulent and low-ζ quiescent phase, a coherent flow phase emerges after a transient period. During this period, the colloid is attracted to the walls of the channel and generates transient fluctuating large-scale flows. The onset of coherence occurs when one of these transient flows spans the entire system. When this happens, the system achieves a steady state in which the colloid is transported along with the fluid; this steady state is robust and persists for arbitrarily long simulations.

Figures 7.2(a-b) (insets) show this behaviour clearly in the parameters ϕ and ψ. In the colloid-stabilised state, the normalised root-mean-squared velocity, ϕ, is distinctly higher than its asymptotic value in the turbulent phase, and the flow order parameter ψ, approaches unity as almost all the flow in the system is directed along the axis of the channel. We also notice that the free colloid displays the largest region of coherent flow. This suggests that any kind of anchoring condition on the colloid works against the mechanism that gives rise to the coherent flow. For this reason we will focus most of our attention on the no-anchoring case.

Figure 7.4 shows the onset of coherent flow in a sequence of snapshots taken from a simulation. Two important facts are clear from this: (1) At the very beginning the colloid is attracted to the corner of the channel (upper-right quadrant) where it remains for the remainder of the simulation; (2) The onset of flow occurs between

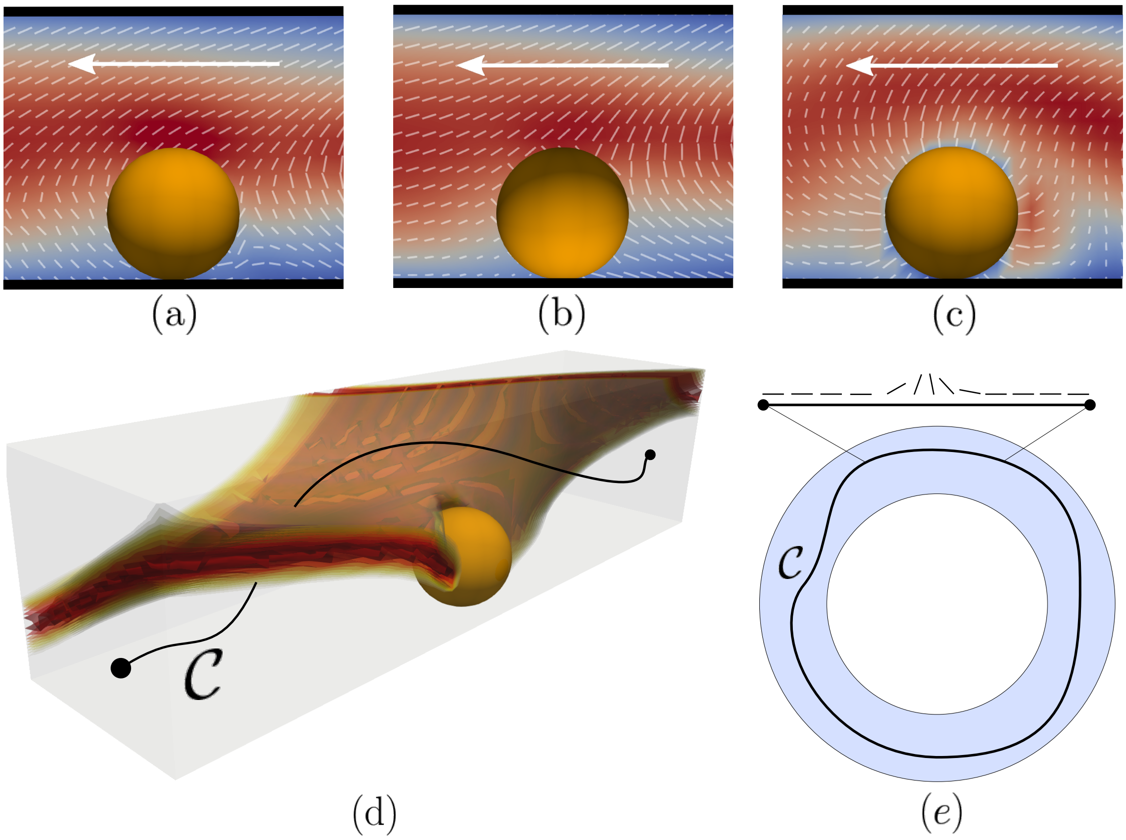

(a) (b) (c)

(d) (e)

Figure 7.5: Defect structure around colloids for (a) planar, (b) free, and (c) normal boundary conditions. (d) Isosurface plots for $|n_\perp| = \sqrt{n_y^2 + n_z^2}$ showing the wall separating regions where $|\boldsymbol{n}| \approx n_\parallel = n_x$. This wall has a Möbius-strip topology, and any closed loop through the channel such as the one shown ($\mathcal{C}$) must pass through the wall an odd number of times, and each time the director suffers a flip $\boldsymbol{n}_\parallel \to -\boldsymbol{n}_\parallel$ resulting in $\boldsymbol{n}$ being topologically nonorientable. (e) Schematic of channel topology showing a segment of $\mathcal{C}$ which passes through the wall, and the associated flip in director field.

panels 3-5, in which it can be seen that the flow begins to span the entire system. We also notice that colloids with planar anchoring end up in the corner of the channel, while colloids with normal anchoring end up touching a single wall; this is opposite to the behaviour observed in a passive fluid, Fig. 7.3. The colloid with no anchoring behaves similarly to the colloid with planar anchoring, and hence is also attracted to the corner of the channel. Thampi *et al.* (2015) showed that activity in a nematic liquid crystal gives rise to an intrinsic free energy not accounted for by the Landau–de Gennes and elastic free energy given in Eq. (1.16) [169], and we hypothesise that this is the cause for this discrepancy.

In Fig. 7.5 the structure of the director field in the immediate vicinity of the colloid is shown for three different anchoring conditions. We see that free anchoring produces a very similar director field to the planar anchoring case. This is caused by the fact that activity results in an effective planar ordering of an extensile fluid at a surface, termed 'active anchoring' [170], and can be understood in terms of the tendency for elongated swimmers to align with solid boundaries [171]. The effective anchoring on the free colloid explains its attraction to the wall, contrary to our observations in the $\zeta = 0$ case.

We note that de Magistris *et al.* (2014) have observed the spontaneous motility of a passive droplet in a quiescent active fluid [172], although their results are different to what we report. In their simulations, the gradients in the director field create small flows which enable the drop to 'creep' steadily through the channel; in our simulations, the colloid 'activates' the entire fluid globally, setting the entire system into a state of flow.

7.4 Discussion & future work

7.4.1 Mechanism

The central result of this chapter is the observation that the inclusion of a passive colloid in a channel-confined active nematic induces a global state of unidirectional, coherent flow in an otherwise quiescent fluid. In particular this occurs for a channel with no imposed boundary conditions, and independent of the boundary conditions on the colloid.

Despite our results providing a demonstration of the robustness of this phenomenon, a clear understanding of the underlying mechanism remains elusive and is the subject of ongoing work. Here we discuss some factors which we believe might play an important role in the mechanism, and suggest ways to test them.

We hypothesise that the mechanism relies on the fact that the inclusion of colloids results in flows generated by the distortion of the nematic director at their surface. As the system is periodic, when these flows span the whole system they move the colloid along with it. Thus the system reaches a steady state where the flow of the active matter, and motion of the colloid are tightly coupled to one another. This hypothesis relies on three ingredients: (1) defects in active fluids are motile; (2) below the transition to turbulence, the activity is too low to spontaneously generate pairs of defects within the bulk; and (3) the presence of a colloid always results in irremovable defects in the fluid.

Motility of active defects

As mentioned in Sec. 1.3, $+1/2$ defects in active nematic liquid crystals are motile [50, 51]. In Fig. 1.2(a) we can see the motion of such a defect in one of our simulations in the turbulent phase ($\zeta = 0.01$). As this fluid is extensile, it moves in such a way as to extend the defect line that connects it to the stationary $-1/2$ defect. The mechanism for this motility is the gradients in $\hat{\boldsymbol{n}}$ that give rise to the elastic and active stresses that enter the Navier–Stokes equations, Eqs. (1.13). In contractile fluids, this is reversed and $+1/2$ defects tend to retreat back along defect lines.

Bulk disappearance of defects

It is also well understood that active turbulence occurs because the homogeneous state of global alignment is unstable to the formation of local nematic domains separated by ‘walls’ of high bending energy [173]. These walls then decay to form pairs of $\pm 1/2$ defects whose motility ensures the continued generation of chaotic flows.

In Fig. 7.1(a) we can see that the initial turbulent state contains defects in the nematic tensor. However when the system relaxes, all the defects have disappeared from the system and the nematic tensor is homogeneous. The simplest defects in a nematic liquid crystal come in one of two charges: $+1/2$ and $-1/2$, both of which cost energy. Because they are topological in nature they may only be created or annihilated in the bulk in pairs, or by disappearing at a boundary. Therefore, at low activity, all the defects will eventually leave the system, allowing the liquid crystal to reach its ground state.

This requires the walls of the system to have free anchoring conditions, otherwise point defects would be repelled from walls and hence remain in the bulk.

Colloid-induced defects

We have already seen in Sec. 1.3, and Fig. 7.3, that the inclusion of spherical colloids results in distortions in the nematic tensor within their vicinity. At sufficient activity (though below the activity required for turbulence), these colloid-induced distortions are enough to create transient flows which push the colloid towards the wall as shown in the first few panels of Fig. 7.4.

7.4.2 Topology of coherent flow state

In the coherent flow phase, the steady-state director field in all cases exhibits an interesting topological property that can be understood by first decomposing the director into components parallel and perpendicular to the channel: $\hat{\boldsymbol{n}} = \boldsymbol{n}_{\parallel} + \boldsymbol{n}_{\perp}$. In all cases, the director tends to align along the channel, $n_{\parallel} > n_{\perp}$. However, in the coherent flow regime, a region of high bending is observed where $n_{\perp} \gg n_{\parallel}$. Interestingly, this region forms a surface which spans the entire system, but includes a half-twist. The surface corresponding to $n_{\perp} = 1$ (and hence $n_{\parallel} = 0$) thus has the topology of a Möbius strip, as can be seen in Fig. 7.5(d). This implies that the director $\hat{\boldsymbol{n}}$ is nonorientable: Along the closed contour $\mathcal{C}$ — topologically similar to the one shown in Fig. 7.5(d) — the director $\hat{\boldsymbol{n}}(\mathcal{C})$ undergoes a flip $\hat{\boldsymbol{n}} \to -\hat{\boldsymbol{n}}$, and so cannot be sensibly defined.[1] This flip is shown schematically in Fig. 7.5(e).

At the Möbius wall, the flow field $\boldsymbol{v}$ is also at its greatest, suggesting that this topological feature of the flow might be an important factor in the mechanism.

7.4.3 Future work

Channel length and colloid size

To obtain a more complete picture of this phenomenon, a number of further tests should be done, exploring the effect of varying the length-scales of the system. First of all, investigating the effect of the channel length might help elucidate the mechanism. Our hypothesis relied on the assumption that transient flows generated by the colloid-induced distortions were able to span the entire system.

---

[1] However, the nematic tensor $\mathbf{Q}$ does remain validly defined.

Thus, a long-distance self-interaction exists for the colloid which must be broken at large channel lengths.

Secondly, we do not yet know if the behaviour we observe has any dependence on the size of the colloid. As our hypothesis for the mechanism was independent of colloid size, so observing such a dependence might provide a key insight.

Fixed colloids

We hypothesised that the colloid's motion is tightly coupled with the flow in the coherent phase. This may be tested by simulating a colloid with a fixed position. Under our hypothesis, a fixed colloid would still generate transient flows due to the distortions near its surface. However, being stationary, it would also act as a source of resistance resulting in flows ultimately dissipating.

We conducted preliminary simulations at $\zeta = 0.005$, which, from Fig. 7.2(b), should result in coherent flow for all types of colloid anchoring conditions tested. In each case we fixed the colloid to be in contact with one wall. We found that with planar or normal anchoring on the colloid surface, transient flows were generated but ultimately dissipated, leaving the system in the quiescent state. However, for a colloid with no anchoring condition, the system evolved into a state of coherent flow just as it did for a moving colloid.

In order to understand the apparent discrepancy between these results, a full survey of the order parameters ϕ, and ψ is required in each case.

7.4.4 Conclusions

In this chapter we have conducted simulations showing the onset of active coherent flow in a channel induced by the inclusion of a passive colloid. We have shown that this effect occurs whether or not anchoring boundary conditions exist on the colloid, though free boundary conditions are required on the channel walls. The anchoring conditions on the colloid affect the range of ζ for which we observe this phase, with largest range being observed for a colloid with free anchoring conditions. This suggests that how the colloid couples to the fluid is important to the mechanism for this phenomenon.

We suggest that this occurs due gradients in the director field in the vicinity of the colloid, which spontaneously generate transient active flows. Steady-state flow is reached when one of these transient flows spans the entire system, setting the colloid in motion with it and thus sustaining unidirectional, constant flow.

We have suggested a number of further tests that can be done in order to gain more information about the system, and these tests constitute our ongoing work.

Our results suggest a novel mechanism that could be utilised by microfluidic devices for the selective transport of passive payloads through channels containing otherwise quiescent active fluids.

8

Discussion and outlook

Chapter 2

We studied the statistical behaviour of a ferromagnetic rod's orientation at equilibrium. Treating it in the canonical ensemble we derived its probability distribution function (pdf) from its Hamiltonian, which provided good agreement with the experimentally obtained data. This pdf displays an effective barrier separating two stable orientational states when the rod is subject to a magnetic field. By analysing the slope of the log-pdf we showed that it is equal to:

$$-\partial_t \ln p(\theta) = \boldsymbol{f}_{\mathrm{gr}}(\theta) + \langle \boldsymbol{f}_{\mathrm{mag}}(\theta, \phi, \gamma) \rangle_{\phi,\gamma|\theta}. \tag{8.1}$$

This equation has the form of a balance between 'pure' Hamiltonian forces due to gravity, and 'entropic' forces due to the cost of thermal fluctuations in the degrees of freedom (ϕ, γ) that were integrated out of the marginal distribution $p(\theta)$.

We explored the idea of obtaining entropic forces from a consideration of the coupling between two interacting subsystems, $\{\boldsymbol{x}\}$ and $\{\boldsymbol{y}\}$. In this treatment, entropic forces on $\boldsymbol{x}$ naturally arise due to ensemble-averaged interaction forces $\boldsymbol{f}_{xy}(\boldsymbol{x}, \boldsymbol{y})$. How this theory could be extended to encompass microcanonical systems — such as the classic example of the entropic elasticity of a polymer — is yet to be fully understood and should be the subject of future research.

Chapter 3

Experiments on ferromagnetic rods driven out of equilibrium by a rotating magnetic field were analysed. First, we outlined a simplified mechanical theory which qualitatively predicts the phase of the rod as a function of driving frequency: I. horizontal–synchronous rotation at low-frequencies, II. vertical–synchronous rotation at intermediate frequencies, and III. horizontal–asynchronous rotation at high-frequencies.

This theory was unable to predict transition frequencies $\tilde{f}_1$ and $\tilde{f}_2$ that fit the experimental data, so we constructed a Brownian dynamics (BD) simulation in order to test the effects of noise. We showed that thermal fluctuations shifted the transition frequency $\tilde{f}_1$ to lower values, and turned the mechanically predicted sharp transition into a smooth crossover. Both of these factors matched experimental observations, suggesting that thermal effects are important in this low-frequency region. We propose that in the low-f_B regime, the equilibrium effects observed in Chapter 2 are still prominent, and drive the periodic hopping between horizontal and vertical states as seen in the timeseries of $L(t)$.

However, the presence of thermal fluctuations does not alter the upper critical frequency $\tilde{f}_2$. This is likely due to the fact that at higher frequencies, the rod is further away from equilibrium, and the strength of the driving torque is much greater than thermal fluctuations: $\mu B \sin\alpha \approx \mu B \approx \mathcal{O}(100)\ k_{\mathrm{B}}T$. Instead, we propose that hydrodynamic interactions are the cause for the discrepancy between the mechanical model and the experimental data. Future work can focus on this either by a correct analytical treatment of the mechanics of a driven rod near a wall, or by BD simulations that incorporate the full rod–wall mobility tensor.

Chapters 4-6

We turned to a current problem in biophysics that concerns the swimming of cells through viscoelastic media. We constructed a Stokesian dynamics (SD) model of a bead–spring polymer interacting with a helical flagellum. By placing polymers in front of the helix, and allowing the helix to either swim towards the polymer, or pump the polymer towards it, we studied the dynamics of the polymer and the energetics of the whole system.

We showed that in both the pinned case and the swimming case, large polymers that were sufficiently close to the helix became hydrodynamically entrained in the rotational flow field and stretched out. By ensemble averaging the distribution of polymeric material across many simulations, we showed that the mean tendency for large polymers was to concentrate in and around the helix itself, contrary to hypotheses made by Martinez *et al.* [108]. For the case of the swimming helix, this capture process is characterised by the spooling of the polymer around the helical filament and the subsequent tight coiling.

This large-polymer–helix interaction results in an increased work rate for the helix to maintain constant angular velocity. In the case of the swimming helix, this is associated with a statistically measurable slow-down in swimming speed. Future work should concentrate on how this may be understood with regard to theoretical and experimental observations of cells speeding up in viscoelastic media. Recently, multiparticle collision dynamics simulations of a constant-torque cell swimming through a solution of bead–spring polymers has shown the opposite effect: polymers are depleted in the immediate vicinity of the flagellum and the cell speeds up [135]. A possible question to investigate in the future is the role of the counter-rotating body which changes the hydrodynamics as well as the steric interactions between polymers and the cell.

We also observed an effect strikingly similar to a hypothesis posed by Shen and Arratia that localised stretching of polymers in highly extensile regions of flow created by a swimmer lead to its retardation [98]. In our simulation of a swimming helix, as small polymers passed through a region of high extensile flow, they were observed to become significantly stretched out. Concomitant to this, the helix suffered a brief, but observable retardation. We showed that this did not happen for larger polymers due to the self-screening effect they have on flow.

Chapter 7

In the final chapter, we looked at active matter confined to a channel using lattice-Boltzmann simulations of the nematohydrodynamic equations that describe the evolution of a nematic liquid crystal. We discovered that a passive spherical colloid could induce its own active transport in an otherwise quiescent fluid. Many open questions on this topic persist, and a full understanding of the mechanism behind this process remains elusive.

Our hypothesis is that the inclusion of the colloid distorts the surrounding fluid, generating flows that span the entire system. The system then finds a steady state in which the colloid's motion is tightly coupled to the coherent, unidirectional flow that is set up.

We also observed an interesting topological property of the coherent flow state in which a region of high-bending energy formed a Möbius strip in the channel. As these regions of bending are associated with spontaneous flow, this suggests a tight correspondence between the global topological state of the system, and the mechanical state of flow. However in order to better characterise this correspondence, more study is required.

Appendices

A
Marginal probability distribution

In Sec. 2.4.2 we showed how entropic forces arise naturally by considering a marginal pdf of a subsystem. Here we will provide this derivation in more detail.

A.1 Linear system

We started by considering a system in which the state variables $\boldsymbol{X} = (X_1, X_2, ...X_n)$ were linearly coupled as if by harmonic springs, with a coupling matrix $\mathbf{K}$ such that the Hamiltonian of the system in quadratic form is given by $\mathcal{H}(\boldsymbol{X}) = \frac{1}{2}\boldsymbol{X}^T\mathbf{K}\boldsymbol{X}$. When we split the system into two interacting subsystems $\boldsymbol{X} = (\boldsymbol{x}, \boldsymbol{y})$ we can decompose this Hamiltonian as in Eq. (2.13):

$$\mathcal{H}(\boldsymbol{x}, \boldsymbol{y}) = \frac{1}{2}\boldsymbol{x}^T\mathbf{K}_{xx}\boldsymbol{x} + \frac{1}{2}\boldsymbol{y}^T\mathbf{K}_{yy}\boldsymbol{y} + \boldsymbol{x}^T\mathbf{K}_{xy}\boldsymbol{y}. \tag{A.1}$$

The *joint* pdf of this system over $(\boldsymbol{x}, \boldsymbol{y})$ is the Boltzmann distribution,

$$p(\boldsymbol{x}, \boldsymbol{y}) = \frac{1}{Z}\exp\left[-\frac{1}{2}\boldsymbol{x}^T\mathbf{K}_{xx}\boldsymbol{x} - \frac{1}{2}\boldsymbol{y}^T\mathbf{K}_{yy}\boldsymbol{y} - \boldsymbol{x}^T\mathbf{K}_{xy}\boldsymbol{y}\right], \tag{A.2}$$

where Z is the normalisation constant:

$$\begin{aligned} Z &= \int \mathrm{d}\boldsymbol{x}\ \mathrm{d}\boldsymbol{y} \exp\left[-\frac{1}{2}\boldsymbol{x}^T\mathbf{K}_{xx}\boldsymbol{x} - \frac{1}{2}\boldsymbol{y}^T\mathbf{K}_{yy}\boldsymbol{y} - \boldsymbol{x}^T\mathbf{K}_{xy}\boldsymbol{y}\right], && \text{(A.3)} \\ &= \int \mathrm{d}\boldsymbol{X} \exp\left[-\frac{1}{2}\boldsymbol{X}^T\mathbf{K}\boldsymbol{X}\right] && \text{(A.4)} \end{aligned}$$

This is a multivariate Gaussian integral which has the solution [174]:

$$\int \mathrm{d}\boldsymbol{X} \exp\left[-\frac{1}{2}\boldsymbol{X}^T\mathbf{K}\boldsymbol{X}\right] = \sqrt{\det 2\pi\mathbf{K}^{-1}}. \tag{A.5}$$

To obtain the *marginal* pdf, $p(\boldsymbol{x}) := \int p(\boldsymbol{x},\boldsymbol{y})\mathrm{d}\boldsymbol{y}$, we need to integrate over $\boldsymbol{y}$

$$p(\boldsymbol{x}) \;=\; \frac{\mathrm{e}^{-\frac{1}{2}\boldsymbol{x}^T\mathbf{K}_{xx}\boldsymbol{x}}}{\sqrt{\det 2\pi\mathbf{K}^{-1}}}\int \mathrm{d}\boldsymbol{y}\;\exp\left[-\frac{1}{2}\boldsymbol{y}^T\mathbf{K}_{yy}\boldsymbol{y} - \boldsymbol{x}^T\mathbf{K}_{xy}\boldsymbol{y}\right]. \tag{A.6}$$

To perform this integral we need to turn the integrand into a Gaussian function. This can be done using the following identity:

$$-\frac{1}{2}\boldsymbol{y}^T\mathbf{A}\boldsymbol{y} + \boldsymbol{b}^T\boldsymbol{y} = -\frac{1}{2}(\boldsymbol{y}-\mathbf{A}^{-1}\boldsymbol{b})^T\mathbf{A}(\boldsymbol{y}-\mathbf{A}^{-1}\boldsymbol{b}) + \frac{1}{2}\boldsymbol{b}^T\mathbf{A}^{-1}\boldsymbol{b}. \tag{A.7}$$

Note that this is the multivariate equivalent of completing the square: $\frac{1}{2}ax^2 - bx = \frac{1}{2}a\left(x-\frac{b}{a}\right)^2 - \frac{b^2}{2a}$. If we compare Eq. (A.7) with the integrand in Eq. (A.6) and set $\boldsymbol{b}^T = -\boldsymbol{x}^T\mathbf{K}_{xy}$, and $\mathbf{A} = \mathbf{K}_{yy}$, we get:

$$\begin{aligned} p(\boldsymbol{x}) \;&=\; \frac{\exp\left[-\frac{1}{2}\boldsymbol{x}^T\mathbf{K}_{xx}\boldsymbol{x} + \frac{1}{2}\boldsymbol{x}^T\mathbf{K}_{xy}\mathbf{K}_{yy}^{-1}\mathbf{K}_{xy}^T\boldsymbol{x}\right]}{\sqrt{\det 2\pi\mathbf{K}^{-1}}} && \text{(A.8)} \\ &\times \int \mathrm{d}\boldsymbol{y}\;\exp\left[-\frac{1}{2}(\boldsymbol{y}+\mathbf{K}_{yy}^{-1}\mathbf{K}_{xy}^T\boldsymbol{x})^T\mathbf{K}_{yy}(\boldsymbol{y}+\mathbf{K}_{yy}^{-1}\mathbf{K}_{xy}^T\boldsymbol{x})\right]. && \text{(A.9)} \end{aligned}$$

The integral in this equation is a Gaussian integral similar to Eq. (A.5) and has the solution $\sqrt{\det 2\pi\mathbf{K}_{yy}^{-1}}$. This yields the solution for the marginal distribution:

$$p(\boldsymbol{x}) = \frac{\sqrt{\det 2\pi\mathbf{K}_{yy}^{-1}}}{\sqrt{\det 2\pi\mathbf{K}^{-1}}}\exp\left[-\frac{1}{2}\boldsymbol{x}^T\mathbf{K}_{xx}\boldsymbol{x} + \frac{1}{2}\boldsymbol{x}^T\mathbf{K}_{xy}\mathbf{K}_{yy}^{-1}\mathbf{K}_{xy}^T\boldsymbol{x}\right]. \tag{A.10}$$

We next want to compute $\langle\boldsymbol{x}^T\mathbf{K}_{xy}\boldsymbol{y}\rangle_{y|x}$ which is the expectation of the interaction potential $\mathcal{H}_{xy}$ conditioned on $\boldsymbol{x}$, defined by:

$$\langle\boldsymbol{x}^T\mathbf{K}_{xy}\boldsymbol{y}\rangle_{y|x} = \int\left(\boldsymbol{x}^T\mathbf{K}_{xy}\boldsymbol{y}\right)p(\boldsymbol{y}|\boldsymbol{x})\mathrm{d}y = \int \boldsymbol{x}^T\mathbf{K}_{xy}\boldsymbol{y}\frac{p(\boldsymbol{x},\boldsymbol{y})}{p(\boldsymbol{x})}\mathrm{d}y. \tag{A.11}$$

First, we consider the ratio $p(\boldsymbol{x},\boldsymbol{y})/p(\boldsymbol{x})$ and see that a number of terms cancel, leaving:

$$\begin{aligned} \frac{p(\boldsymbol{x},\boldsymbol{y})}{p(\boldsymbol{x})} \;&=\; \frac{\mathrm{e}^{-\frac{1}{2}\boldsymbol{y}^T\mathbf{K}_{yy}\boldsymbol{y}-\boldsymbol{x}^T\mathbf{K}_{xy}\boldsymbol{y}}}{\sqrt{\det 2\pi\mathbf{K}_{yy}^{-1}}\,\mathrm{e}^{\frac{1}{2}\boldsymbol{x}^T\mathbf{K}_{xy}\mathbf{K}_{yy}^{-1}\mathbf{K}_{xy}^T\boldsymbol{x}}} && \text{(A.12)} \\ &=\; \frac{\mathrm{e}^{-\frac{1}{2}\boldsymbol{y}^T\mathbf{K}_{yy}\boldsymbol{y}-\boldsymbol{x}^T\mathbf{K}_{xy}\boldsymbol{y}-\frac{1}{2}\boldsymbol{x}^T\mathbf{K}_{xy}\mathbf{K}_{yy}^{-1}\mathbf{K}_{xy}^T\boldsymbol{x}}}{\sqrt{\det 2\pi\mathbf{K}_{yy}^{-1}}} && \text{(A.13)} \\ &=\; \frac{\exp\left[-\frac{1}{2}(\boldsymbol{y}-\mathbf{K}_{yy}^{-1}\mathbf{K}_{xy}^T\boldsymbol{x})^T\mathbf{K}_{yy}(\boldsymbol{y}-\mathbf{K}_{yy}^{-1}\mathbf{K}_{xy}^T\boldsymbol{x})\right]}{\sqrt{\det 2\pi\mathbf{K}_{yy}^{-1}}} && \text{(A.14)} \end{aligned}$$

This is the pdf for a normalised multivariate Gaussian with mean $\boldsymbol{\mu} = \mathbf{K}_{yy}^{-1}\mathbf{K}_{xy}^{T}\boldsymbol{x}$, and variance–covariance matrix $\boldsymbol{\Sigma} = \mathbf{K}_{yy}^{-1}$, which we denote as $g(\boldsymbol{\mu}, \boldsymbol{\Sigma})$. The conditional expectation may now be computed directly:

$$\begin{aligned}
\langle \boldsymbol{x}^T \mathbf{K}_{xy} \boldsymbol{y} \rangle_{y|x} &= \int \mathrm{d}\boldsymbol{y}\; \boldsymbol{x}^T \mathbf{K}_{xy} \boldsymbol{y} g(\boldsymbol{\mu}, \boldsymbol{\Sigma}), && \text{(A.15)} \\
&= \boldsymbol{x}^T \mathbf{K}_{xy} \int \mathrm{d}\boldsymbol{y}\; \boldsymbol{y} g(\boldsymbol{\mu}, \boldsymbol{\Sigma}), && \text{(A.16)} \\
&= \boldsymbol{x}^T \mathbf{K}_{xy} \boldsymbol{\mu}, && \text{(A.17)} \\
&= \boldsymbol{x}^T \mathbf{K}_{xy} \mathbf{K}_{yy}^{-1} \mathbf{K}_{xy}^T \boldsymbol{x}. && \text{(A.18)}
\end{aligned}$$

B

Rotating rod dynamics

B.1 Rotational friction coefficients

Ellipsoids

Kim & Karilla (1991) exactly derive the friction coefficients for spheroids whose surfaces are described by $(x/a)^2 + (y/b)^2 + (z/c)^2 = 1$ [12]. In the case of an ellipsoid, $a > b = c$, their results are:

$$\zeta_{\parallel} = 8\pi\eta a^3 \frac{4e^3(1-e^2)}{3[2e-(1-e^2)\chi(e)]}, \tag{B.1}$$

$$\zeta_{\perp} = 8\pi\eta a^3 \frac{4e^3(2-e^2)}{3[-2e+(1+e^2)\chi(e)]}, \tag{B.2}$$

with

$$\chi(e) = \ln\frac{1+e}{1-e}, \quad e = \frac{\sqrt{a^2-c^2}}{a}. \tag{B.3}$$

Cylinders

No exact solution exists for 3-dimensional flow around a finite sphere, but approximations for the friction coefficients have been found by Brenner (1974) [175]. Here we present the form given in Ref. [82]:

$$\zeta_{\parallel} = 8\pi\eta a^3 \frac{1+C^{\parallel}}{0.96(a/c)^2}, \tag{B.4}$$

$$\zeta_{\perp} = 8\pi\eta a^3 \frac{1}{3(\ln(a/c)+C^{\perp})}, \tag{B.5}$$

where

$$C^{\parallel} = \frac{0.677}{a/c} - \frac{0.183}{(a/c)^2}, \quad C^{\perp} = -0.662 + \frac{0.917}{a/c} - \frac{0.05}{(a/c)^2}. \tag{B.6}$$

Calculation

We use the above equations to calculate $\zeta_{\parallel,\perp}$ for a rod with length $2a = 3.7$, and diameter $2d = 0.65$. To compute errors, we repeated this calculation $N = 10000$ times with Gaussian noise added to a and c to account for the errors in experimental measurement.

B.2 Integration of Brownian dynamics

We follow the prescription of Delong et al. (2015) who derive a set of difference equations which approximate the integration of the SDEs for the orientation quaternion [Eq. (3.5)] and position vector [Eq. (3.7)] of an elongated particle. They rewrite the two SDEs as a single SDE in a split Stratonovich–Itô form,

$$\frac{d\boldsymbol{X}}{dt} = -(\boldsymbol{\Xi}\boldsymbol{\mu}\boldsymbol{\Xi}^T)\boldsymbol{\nabla}_{\boldsymbol{X}}\mathcal{H}(\boldsymbol{X}) + \sqrt{2k_{\mathrm{B}}T}\boldsymbol{\Xi}\boldsymbol{\mu} \circ \mathbf{b}\boldsymbol{W}, \tag{B.7}$$

where $\boldsymbol{X} = (\boldsymbol{r}, \boldsymbol{\theta})$ is the full state of the system, and

$$\boldsymbol{\Xi} = \begin{bmatrix} \boldsymbol{I} & \mathbf{0} \\ \mathbf{0} & \boldsymbol{\Psi} \end{bmatrix}, \quad \boldsymbol{\mu} = \begin{bmatrix} \boldsymbol{\mu}^{\mathrm{t}} & \boldsymbol{\mu}^{\mathrm{tr}} \\ (\boldsymbol{\mu}^{\mathrm{tr}})^T & \boldsymbol{\mu}^{\mathrm{r}} \end{bmatrix}, \quad \mathbf{b}\mathbf{b}^T = \boldsymbol{\mu}. \tag{B.8}$$

In our simulations, because we do not account for hydrodynamic interactions with the substrate, the translational–rotational mobilities vanish: $\boldsymbol{\mu}^{\mathrm{tr}} = 0$. In the mixed Stratonovich–Itô form, terms after $\circ$ are evaluated at the beginning of each time step, and those before are evaluated at the midpoint between time steps. To do this, we use Fixman's midpoint scheme in the integration of Eq. (B.7) which gives the following predictor–corrector algorithm:

$$\dot{\boldsymbol{X}}_0 = \begin{bmatrix}\boldsymbol{v}\\ \boldsymbol{\omega}\end{bmatrix}_0 = \boldsymbol{\mu}_0 \begin{bmatrix}\boldsymbol{f}\\ \boldsymbol{\tau}\end{bmatrix}_0 + \sqrt{\frac{2k_{\mathrm{B}}T}{\Delta t/2}}\mathbf{b}_0\boldsymbol{W}_0, \tag{B.9}$$

$$\boldsymbol{r}_{\frac{1}{2}} = \boldsymbol{r}_0 + \frac{\Delta t}{2}\boldsymbol{v}_0, \tag{B.10}$$

$$\boldsymbol{\theta}_{\frac{1}{2}} = \mathrm{Rotate}\left(\boldsymbol{\theta}_0, \frac{\Delta t}{2}\boldsymbol{\omega}_0\right), \tag{B.11}$$

$$\dot{\boldsymbol{X}}_{\frac{1}{2}} = \begin{bmatrix}\boldsymbol{v}\\ \boldsymbol{\omega}\end{bmatrix}_{\frac{1}{2}} = \boldsymbol{\mu}_{\frac{1}{2}} \begin{bmatrix}\boldsymbol{f}\\ \boldsymbol{\tau}\end{bmatrix}_{\frac{1}{2}} + \sqrt{\frac{k_{\mathrm{B}}T}{\Delta t/}}\boldsymbol{\mu}_{\frac{1}{2}}\mathbf{b}_0^{-1}(\boldsymbol{W}_0 + \boldsymbol{W}_{\frac{1}{2}}), \tag{B.12}$$

$$\boldsymbol{r}_1 = \boldsymbol{r}_0 + \Delta t\boldsymbol{v}_{\frac{1}{2}}, \tag{B.13}$$

$$\boldsymbol{\theta}_1 = \mathrm{Rotate}(\boldsymbol{\theta}_0, \Delta t\boldsymbol{\omega}_{\frac{1}{2}}). \tag{B.14}$$

The subscript $k \in \left\{0, \frac{1}{2}, 1\right\}$ denotes a quantity evaluated at $t_n + k\Delta t$ for the nth time step. The force and torque are $(\boldsymbol{f}, \boldsymbol{\tau})^T = -\boldsymbol{\nabla}\mathcal{H}$.

References

[1] J. Bardeen and W. H. Brattain. Transistor, a semiconductor triode, *Physical Review*, **74**, 230 (1948).

[2] K. S. Novoselov et al. Electric Field Effect in Atomically Thin Carbon Films, *Science*, **666**, 2004 (2004).

[3] D. Weaire and R. Phelan. The physics of foam, *Journal of Physics: Condensed Matter*, **8**, 9519 (1996).

[4] I. A. Martínez et al. Colloidal heat engines: a review, *Soft Matter*, **13**, 22 (2017).

[5] J. M. Berg, J. L. Tymoczko, and L. Stryer. *Biochemistry.* 7th Ed. New York: W.H. Freeman, 2002.

[6] E. Shakhnovich. Protein folding thermodynamics and dynamics: Where physics, chemistry, and biology meet, *Chemical Reviews*, **106**, 1559-1588 (2006).

[7] O. M. Elrad and M. F. Hagan. Encapsulation of a polymer by an icosahedral virus, *Physical Biology*, **7**, 045003 (2010).

[8] J. Elgeti, R. G. Winkler, and G. Gompper. Physics of microswimmers–single particle motion and collective behavior: a review. *Reports on Progress in Physics*, **78**, 056601 (2015).

[9] M. C. Marchetti et al. Hydrodynamics of soft active matter, *Reviews of Modern Physics*, **85**, 3 (2013).

[10] P.-G. de Gennes. Soft matter, *Reviews of Modern Physics*, **64**, 645-648 (1992).

[11] S. Ramaswamy. Active matter, *Journal of Statistical Mechanics: Theory and Experiment*, Special Issue (2017).

[12] S. Kim and S. J. Karilla. *Microhydrodynamics: Principles and Selected Applications.* 2nd Ed. New York: Dover, 1991.

[13] M. Doi and S. F. Edwards. *The Theory of Polymer Dynamics.* Oxford: Oxford University Press, 1988.

[14] D. J. Tritton. *Physical Fluid Dynamics.* 2nd Ed. Oxford: Oxford University Press, 1988.

[15] M. Lisicki. Four approaches to hydrodynamic Green's functions – the Oseen tensors, (2013). arXiv: `1312.6231`.

[16] S. Suarez and A. Pacey. Sperm transport in the female reproductive tract. *Human reproduction update*, **12**, 1 (2006).

[17] H. C. Ho and S. S. Suarez. Hyperactivation of mammalian spermatozoa: Function and regulation, *Reproduction*, **122**, 519-526 (2001).

[18] K. M. Ottemann and J. F. Miller. Roles for motility in bacterial – host interactions. *Molecular Microbiology*, **24**, 6 (1997).

[19] C. Josenhans and S. Suerbaum. The role of motility as a virulence factor in bacteria. *International Journal of Medical Microbiology*, **291**, 605-614 (2002).

[20] J. Celli et al. Helicobacter pylori moves through mucus by reducing mucin viscoelasticity, *Proceedings of the National Academy of Sciences*, **106**, 34 (2009).

[21] A. Houry et al. Bacterial swimmers that infiltrate and take over the biofilm matrix, *Proceedings of the National Academy of Sciences*, **109**, 32 (2012).

[22] J. B. Kaper, J. P. Nataro, and H. L. T. Mobley. Pathogenic Escherichia coli, *Nature Reviews Microbiology*, **2**, 123-140 (Feb. 2004).

[23] H. C. Berg. The Rotary Motor of Bacterial Flagella, *Annual Review of Biochemistry*, **72**, 19-54 (2003).

[24] J. Yuan, K. A. Fahrner, and H. C. Berg. Switching of the Bacterial Flagellar Motor Near Zero Load, *Journal of Molecular Biology*, **390**, 3 (2009).

[25] M. E. Cates and J. Tailleur. When are active Brownian particles and run-and-tumble particles equivalent? Consequences for motility-induced phase separation, *EPL (Europhysics Letters)*, **101**, 20010 (2013).

[26] K. E. Peyer, L. Zhang, and B. J. Nelson. Bio-inspired magnetic swimming microrobots for biomedical applications. *Nanoscale*, **5**, 1259 (Feb. 2013).

[27] W. Gao et al. Bioinspired helical microswimmers based on vascular plants, *Nano Letters*, **14**, 305-310 (2014).

[28] W. F. Paxton et al. Catalytic nanomotors: Autonomous movement of striped nanorods, *Journal of the American Chemical Society*, **126**, 13424-13431 (2004).

[29] E. Purcell. Life at low Reynolds number, *American Journal of Physics*, **45**, 1 (1977).

[30] S. E. Spagnolie and E. Lauga. Hydrodynamics of self-propulsion near a boundary: predictions and accuracy of far-field approximations, *Journal of Fluid Mechanics*, **700**, 105-147 (2012).

[31] A. J. Mathijssen et al. Upstream Swimming in Microbiological Flows, *Physical Review Letters*, **116**, 2 (2016).

[32] N. Uchida and R. Golestanian. Synchronization and collective dynamics in a carpet of microfluidic rotors, *Physical Review Letters*, **104**, 178103 (2010).

[33] R. R. Bennett and R. Golestanian. Phase-dependent forcing and synchronization in the three-sphere model of Chlamydomonas, *New Journal of Physics*, **15**, 075028 (2013).

[34] I. H. Riedel, K. Kruse, and J. Howard. A self-organized vortex array of hydrodynamically entrained sperm cells. *Science*, **309**, 300 (2005).

[35] Y. Yang, J. Elgeti, and G. Gompper. Cooperation of sperm in two dimensions: Synchronization, attraction, and aggregation through hydrodynamic interactions, *Physical Review E*, **78**, 061903 (2008).

[36] M. Ballerini et al. Empirical investigation of starling flocks: a benchmark study in collective animal behaviour, *Animal Behaviour*, **76**, 201-215 (2008).

[37] T. Vicsek et al. *Novel type of phase transition in a system of self-riven particles.* 1995.

[38] J. Toner, Y. Tu, and S. Ramaswamy. *Hydrodynamics and phases of flocks.* 2005.

[39] P. Bunyard-Wild. *Gretna Green Starling Murmurations.* 2013. url: `https://www.youtube.com/watch?v=M1Q-EbX6dso` (visited on 09/08/2017).

[40] C. K. Hemelrijk, L. van Zuidam, and H. Hildenbrandt. What underlies waves of agitation in starling flocks, *Behavioral Ecology and Sociobiology*, **69**, 755-764 (2015).

[41] Y. Sumino et al. Large-scale vortex lattice emerging from collectively moving microtubules, *Nature*, **483**, 448-452 (2012).

[42] C. Dombrowski et al. Self-concentration and large-scale coherence in bacterial dynamics, *Physical Review Letters*, **93**, 098103 (2004).

[43] A. Bricard et al. Emergence of macroscopic directed motion in populations of motile colloids. *Nature*, **503**, 95-8 (2013).

[44] S. D. Ryan et al. Correlation properties of collective motion in bacterial suspensions, *New Journal of Physics*, **15**, 105021 (2013).

[45] A. N. Beris and B. J. Edwards. *Thermodynamics of flowing systems: with internal microstructure.* Oxford: Oxford University Press, 1994.

[46] T. Machon and G. P. Alexander. Knots and nonorientable surfaces in chiral nematics, *Proceedings of the National Academy of Sciences*, **110**, 35 (2013).

[47] M. Eisenberg and R. Guy. A Proof of the Hairy Ball Theorem, *The American Mathematical Monthly*, **86**, 571-574 (1979).

[48] C. P. Lapointe, T. G. Mason, and I. I. Smalyukh. Shape-Controlled Colloidal Interactions in Nematic Liquid Crystals, *Science*, **326**, 1083-1086 (2009).

[49] L. Giomi et al. Defect annihilation and proliferation in active Nematics, *Physical Review Letters*, **110**, 228101 (2013).

[50] F. C. Keber et al. Topology and dynamics of active nematic vesicles, *Science*, **345**, 1135-1139 (2014).

[51] S. J. DeCamp et al. Orientational order of motile defects in active nematics, *Nature Materials*, **14**, 1110-1115 (2015).

[52] S. J. Blundell and K. M. Blundell. *Concepts in Thermal Physics.* Oxford: Oxford University Press, 2012.

[53] U. M. B. Marconi et al. Fluctuation-dissipation: Response theory in statistical physics, *Physics Reports*, **461**, 111-195 (2008).

[54] B. Oksendal. *Stochastic Differential Equations.* 6th Ed. New York: Springer, 2010.

[55] J. M. Sancho. Brownian colloidal particles: Ito, Stratonovich, or a different stochastic interpretation, *Physical Review E*, **84**, 062102 (2011).

[56] G. Pesce et al. Stratonovich-to-Itô transition in noisy systems with multiplicative feedback. *Nature communications*, **4**, 2733 (2013).

[57] R. M. Neumann. The entropy of a single Gaussian macromolecule in a noninteracting solvent, *The Journal of Chemical Physics*, **66**, 870 (1977).

[58] S. Smith, L. Finzi, and C. Bustamante. Direct mechanical measurements of the elasticity of single DNA molecules by using magnetic beads, *Science*, **258**, 1122 (1992).

[59] C. Bustamante et al. Entropic elasticity of lambda-phage DNA, *Science*, **265**, 5178 (1994).

[60] M. S. Kellermayer. Folding-Unfolding Transitions in Single Titin Molecules Characterized with Laser Tweezers, *Science*, **276**, 1112-1116 (1997).

[61] V. Vogel and M. Sheetz. Local force and geometry sensing regulate cell functions, *Nature Reviews Molecular Cell Biology*, **7**, 265-275 (2006).

[62] V. V. Palyulin, T. Ala-Nissila, and R. Metzler. Polymer translocation: the first two decades and the recent diversification, *Soft Matter*, **10**, 9016 (2014).

[63] W. Sung and P. J. Park. Polymer Translocation througha Pore in a Membrane, *Physical Review Letters*, **77**, 4 (1996).

[64] M. Muthukumar. Theory of capture rate in polymer translocation, *Journal of Chemical Physics*, **132**, 10371 (2010).

[65] I. Ali, D. Marenduzzo, and J. M. Yeomans. Polymer packaging and ejection in viral capsids: Shape matters, *Physical Review Letters*, **96**, 208102 (2006).

[66] Z. Zhang, H. Chen, and Z. Hou. Entropic stochastic resonance of a flexible polymer chain in a confined system, *The Journal of Chemical Physics*, **137**, 044904 (2012).

[67] L. Ruiz, S. Keten, and M. L. Klein. Directing the self-assembly of supra-biomolecular nanotubes using entropic forces, *Soft Matter*, **10**, 851 (2014).

[68] H. Mostafavi et al. Entropic forces drive self-organization and membrane fusion by SNARE proteins, *Proceedings of the National Academy of Sciences*, **114**, 21 (2017).

[69] T. Chou and D. Lohse. Entropy-driven pumping in zeolites and biological channels, *Physical Review Letters*, **82**, 3552 (1999).

[70] R. Zwanzig. Diffusion past an entropy barrier, *The Journal of Physical Chemistry*, **96**, 3926-3930 (1992).

[71] H. Ding, H. Jiang, and Z. Hou. Entropic stochastic resonance without external force in oscillatory confined space, *The Journal of Chemical Physics*, **142**, 194109 (2015).

[72] A. Dinsmore, A. Yodh, and D. Pine. Entropic control of particle motion using passive surface microstructures, *Nature*, **383**, 239-242 (1996).

[73] L. Helden et al. Direct Measurement of Entropic Forces Induced by Rigid Rods, *Physical Review Letters*, **90**, 048301 (2003).

[74] R. M. Neumann. Entropic approach to Brownian movement, *American Journal of Physics*, **48**, 354 (1980).

[75] N. Roos. Entropic forces in Brownian motion, *American Journal of Physics*, **82**, 1161 (2014).

[76] E. Verlinde. On the origin of gravity and the laws of Newton, *JHEP 04*, **029** (2011).

[77] A. D. Wissner-Gross and C. E. Freer. Causal Entropic Forces, *Physical Review Letters*, **110**, 168702 (Apr. 2013).

[78] Y. Gao et al. Thermal Analog of Gimbal Lock in a Colloidal Ferromagnetic Janus Rod, *Physical Review Letters*, **115**, 248301 (2015).

[79] A. Kuijk, A. V. Blaaderen, and A. Imhof. Synthesis of monodisperse, rodlike silica colloids with tunable aspect ratio, *Journal of the American Chemical Society*, **133**, 2346-2349 (2011).

[80] P. Dhar et al. Orientations of Overdamped Magnetic Nanorod-Gyroscopes, *Nano letters*, **7**, 1010-1012 (2007).

[81] H. Kurokawa. A Geometric Study of Single Gimbal Control Moment Gyros A Geometric Study of Single Gimbal Control Moment Gyros, *Report of Mechanical Engineering Laboratory*, 175 (1998).

[82] A. Ghosh et al. Analytical theory and stability analysis of an elongated nanoscale object under external torque. *Physical Chemistry Chemical Physics*, **15**, 10817 (2013).

[83] P. Tierno et al. Controlled swimming in confined fluids of magnetically actuated colloidal rotors, *Physical Review Letters*, **101**, 21 (2008).

[84] P. Tierno et al. Overdamped dynamics of paramagnetic ellipsoids in a precessing magnetic field, *Physical Review E*, **79**, 021501 (2009).

[85] F. Martinez-Pedrero et al. Emergent Hydrodynamic Bound States Between Magnetically Powered Micropropellers, (2017). arXiv: `1709.0422v1`.

[86] S. Broersma. Rotational Diffusion Constant of a Cylindrical Particle, *Journal of Chemical Physics*, **32**, 1626-1631 (1960).

[87] S. Delong, F. Balboa Usabiaga, and A. Donev. Brownian dynamics of confined rigid bodies, *Journal of Chemical Physics*, **143**, 144107 (2015).

[88] M. Fixman. Simulation of polymer dynamics. I. General theory, *The Journal of Chemical Physics*, **69**, 1527-1537 (1978).

[89] M. De Corato et al. Hydrodynamics and Brownian motions of a spheroid near a rigid wall, *Journal of Chemical Physics*, **142**, 19 (2015).

[90] M. Lisicki, B. Cichocki, and E. Wajnryb. Near-wall diffusion tensor of an axisymmetric colloidal particle, *Journal of Chemical Physics*, **145**, 034904 (2016).

[91] J. Sznitman and P. Arratia. "Locomotion in Complex Fluids: Experiments", *Complex Fluids in Biological Systems*. Ed. by S. Spagnolie. New York: Springer, 2015.

[92] S. Spagnolie. *Complex Fluids in Biological Systems: Experiment, Theory, and Computation*. Ed. by S. E. Spagnolie. Biological and Medical Physics, Biomedical Engineering. New York: Springer, 2014.

[93] E. Lauga. Locomotion in complex fluids: Integral theorems, *Physics of Fluids*, **26**, 081902 (2014).

[94] E. Riley and E. Lauga. Enhanced active swimming in viscoelastic fluids, *EPL (Europhysics Letters)*, **108**, 34003 (2014).

[95] H. Fu, T. Powers, and C. Wolgemuth. Theory of Swimming Filaments in Viscoelastic Media, *Physical Review Letters*, **99**, 258101 (2007).

[96] L. Zhu et al. Self-propulsion in viscoelastic fluids: Pushers vs. pullers, *Physics of Fluids*, **24**, 051902 (2012).

[97] B. Qin et al. Flagellar kinematics and swimming of algal cells in viscoelastic fluids. *Scientific Reports*, **5**, 9190 (2015).

[98] X. Shen and P. Arratia. Undulatory Swimming in Viscoelastic Fluids, *Physical Review Letters*, **106**, 208101 (2011).

[99] D. Gagnon, X. Shen, and P. Arratia. Undulatory swimming in fluids with polymer networks, *Europhysics Letters (EPL)*, **104**, 14004 (2013).

[100] E. Lauga. Propulsion in a viscoelastic fluid, *Physics of Fluids*, **19**, 083104 (2007).

[101] J. Teran, L. Fauci, and M. Shelley. Viscoelastic Fluid Response Can Increase the Speed and Efficiency of a Free Swimmer, *Physical Review Letters*, **104**, 038101 (Jan. 2010).

[102] B. Thomases and R. D. Guy. Mechanisms of elastic enhancement and hindrance for finite-length undulatory swimmers in viscoelastic fluids, *Physical Review Letters*, **113**, 098102 (2014).

[103] G. E. Kaiser and R. N. Doetsch. Letter: Enhanced translational motion of Leptospira in viscous environments, *Nature*, **255**, 656-657 (1975).

[104] H. C. Berg and L. Turner. Movement of microorganisms in viscous environments. *Nature*, **278**, 349-351 (1979).

[105] B. Liu, T. R. Powers, and K. S. Breuer. Force-free swimming of a model helical flagellum in viscoelastic fluids, *Proceedings of the National Academy of Sciences*, **108**, 49 (2011).

[106] S. E. Spagnolie, B. Liu, and T. R. Powers. Locomotion of Helical Bodies in Viscoelastic Fluids: Enhanced Swimming at Large Helical Amplitudes, *Physical Review Letters*, **111**, 068101 (2013).

[107] S. A. Mirbagheri and H. C. Fu. Helicobacter pylori Couples Motility and Diffusion to Actively Create a Heterogeneous Complex Medium in Gastric Mucus, *Physical Review Letters*, **116**, 198101 (2016).

[108] V. A. Martinez et al. Flagellated bacterial motility in polymer solutions. *Proceedings of the National Academy of Sciences*, **111**, 50 (2014).

[109] A. E. Patteson et al. Running and tumbling with E. coli in polymeric solutions. *Scientific Reports*, **5**, 15761 (2015).

[110] M. D. Manson. Dynamic motors for bacterial flagella, *Proceedings of the National Academy of Sciences*, **107**, 25 (2010).

[111] M. Manghi et al. Hydrodynamic effects in driven soft matter, *Soft Matter*, **2**, 653-668 (2006).

[112] N. Coq et al. Helical beating of an actuated elastic filament. *Journal of Physics: Condensed Matter*, **21**, 204109 (2009).

[113] M. K. Jawed et al. Propulsion and Instability of a Flexible Helical Rod Rotating in a Viscous Fluid, *Physical Review Letters*, **115**, 168101 (2015).

[114] J. J. L. Higdon. The generation of feeding currents by flagellar motions, *Journal of Fluid Mechanics*, **94**, 306-330 (1979).

[115] E. Lauga and T. R. Powers. The hydrodynamics of swimming microorganisms, *Reports on Progress in Physics*, **72**, 096601 (Sept. 2009).

[116] R. E. Pepper et al. Nearby boundaries create eddies near microscopic filter feeders, *Journal of The Royal Society Interface* (2009).

[117] A. P. Petroff et al. Biophysical basis for convergent evolution of two veil-forming microbes, *Royal Society Open Science*, **2**, 150437 (2015).

[118] A. P. Petroff and A. Libchaber. Hydrodynamics and collective behavior of the tethered bacterium Thiovulum majus, *Proceedings of the National Academy of Sciences*, **111**, 5 (2014).

[119] J. S. Guasto, R. Rusconi, and R. Stocker. Fluid Mechanics of Planktonic Microorganisms, *Annual Review of Fluid Mechanics*, **44**, 373-400 (2012).

[120] J. Rotne and S. Prager. Variational Treatment of Hydrodynamic Interaction in Polymers, *Journal of Chemical Physics*, **50**, 4831-4837 (1969).

[121] H. Yamakawa. Transport Properties of Polymer Chains in Dilute Solution: Hydrodynamic Interaction, *J. Chem. Phys.*, **53**, 436 (1970).

[122] G. W. Slater et al. Modeling the separation of macromolecules: A review of current computer simulation methods, *Electrophoresis*, **30**, 792-818 (2009).

[123] G. S. Grest and K. Kremer. Molecular dynamics simulation for polymers in the presence of a heat bath, *Physical Review A*, **33**, 3628-3631 (1986).

[124] J. Hu et al. Modelling the mechanics and hydrodynamics of swimming E. coli, *Soft Matter*, **11**, 40 (2015).

[125] J. P. Cotton. Polymer excluded volume exponent nu: An experimental verification of the n vector model for n=0, *Journal de Physique Lettres*, **41**, L-231-234 (1980).

[126] M. Rubinstein and R. Colby. *Polymer Physics*. Oxford: Oxford University Press, 2003.

[127] J. Yuan and H. C. Berg. Following the Behavior of the Flagellar Rotary Motor Near Zero Load, *Experimental Mechanics2*, **50**, 9 (2010).

[128] J. Xing et al. Torque-speed relationship of the bacterial flagellar motor. *Proceedings of the National Academy of Sciences*, **103**, 5 (2006).

[129] M. Kim et al. A macroscopic scale model of bacterial flagellar bundling, *Proceedings of the National Academy of Sciences*, **100**, 26 (2003).

[130] Kim et al. Particle image velocimetry experiments on a macro-scale model for bacterial flagellar bundling, *Experiments in Fluids*, **37**, 782-788 (2004).

[131] T. S. Yu, E. Lauga, and a. E. Hosoi. Experimental investigations of elastic tail propulsion at low {R}eynolds number, *Phys. Fluids*, **18**, 091701 (2006). arXiv: `0606527v1 [arXiv:cond-mat]`.

[132] S. Zhong et al. The flow field and axial thrust generated by a rotating rigid helix at low Reynolds numbers, *Experimental Thermal and Fluid Science*, **46**, 1-7 (2013).

[133] J. Lighthill. Flagellar Hydrodynamics, *SIAM Review*, **18**, 2 (1976).

[134] B. Rodenborn et al. Propulsion of microorganisms by a helical flagellum, *Proceedings of the National Academy of Sciences*, **110**, 5 (2013).

[135] A. Zöttl and J. M. Yeomans. Bacterial dynamics in macromolecular polymer solutions, *(in preparation)* (2017).

[136] A. K. Balin et al. Biopolymer dynamics driven by helical flagella, *(submitted)* (2017). arXiv: `1706.03961`.

[137] M. D. Graham. Fluid Dynamics of Dissolved Polymer Molecules in Confined Geometries, *Annual Review of Fluid Mechanics*, **43**, 273-298 (2011).

[138] T. N. Shendruk et al. Spin-induced macromolecular spooling, *Physical Review X*, **7**, 031005 (2017).

[139] U. Seifert. Stochastic thermodynamics, fluctuation theorems and molecular machines. *Reports on Progress in Physics*, **75**, 126001 (2012).

[140] R. Ledesma-Aguilar and J. M. Yeomans. Enhanced Motility of a Microswimmer in Rigid and Elastic Confinement, *Physical Review Letters*, **111**, 138101 (2013).

[141] J. K. Wróbel et al. Enhanced flagellar swimming through a compliant viscoelastic network in Stokes flow, *Journal of Fluid Mechanics*, **792**, 775-797 (2016).

[142] A. Ghosh et al. Dynamical configurations and bistability of helical nanostructures under external torque, *Physical Review E*, **86**, 031401 (2012).

[143] S. Gomez et al. Helical propulsion in shear-thinning fluids, *Journal of Fluid Mechanics*, **812**, R3 (2017).

[144] H. Wada and R. R. Netz. Hydrodynamics of helical-shaped bacterial motility, *Physical Review E*, **80**, 021921 (2009).

[145] T. Bittig et al. Dynamics of anisotropic tissue growth, *New Journal of Physics*, **10**, 063001 (2008).

[146] D. Needleman and Z. Dogic. Active matter at the interface between materials science and cell biology, *Nature Reviews Materials*, **2**, 17048 (2017).

[147] A. Solovev et al. Self-propelled nanotools, *ACS Nano*, **6**, 2 (2012).

[148] J. Wang. Can man-made nanomachines compete with nature biomotors?, *ACS Nano*, **3**, 1 (2009).

[149] S. P. Thampi et al. Active micromachines: Microfluidics powered by mesoscale turbulence, *Science Advances*, **2**, e1501854 (2016).

[150] R. Voituriez, J. F. Joanny, and J. Prost. Spontaneous flow transition in active polar gels, *Europhysics Letters (EPL)*, **70**, 3 (2005).

[151] D. Marenduzzo, E. Orlandini, and J. Yeomans. Hydrodynamics and rheology of active liquid crystals: A numerical investigation, *Physical Review Letters*, **98**, 118102 (2007).

[152] D. Marenduzzo et al. Steady-state hydrodynamic instabilities of active liquid crystals: Hybrid lattice Boltzmann simulations, *Physical Review E - Statistical, Nonlinear, and Soft Matter Physics*, **76**, 031921 (2007).

[153] D. Marenduzzo et al. Lattice Boltzmann simulations of spontaneous flow in active liquid crystals: The role of boundary conditions, *Journal of Non-Newtonian Fluid Mechanics*, **149**, 56-62 (2008).

[154] S. A. Edwards and J. M. Yeomans. Spontaneous flow states in active nematics: A unified picture, *EPL (Europhysics Letters)*, **85**, 18008 (2009).

[155] M. Theillard, R. Alonso-Matilla, and D. Saintillan. Geometric control of active collective motion, *Soft Matter*, **13**, 363 (2017).

[156] F. G. Woodhouse and R. E. Goldstein. Spontaneous circulation of confined active suspensions, *Physical Review Letters*, **109**, 168105 (2012).

[157] H. Wioland et al. Confinement stabilizes a bacterial suspension into a spiral vortex, *Physical Review Letters*, **110**, 26 (2013). arXiv: `1304.2875`.

[158] K.-T. Wu et al. Transition from turbulent to coherent flows in confined three-dimensional active fluids, *Science*, **355**, 1284 (2017).

[159] A. Doostmohammadi et al. Stabilization of active matter by flow-vortex lattices and defect ordering. *Nature communications*, **7**, 10557 (2016).

[160] T. N. Shendruk et al. Dancing disclinations in confined active nematics, *Soft Matter*, **13**, 21 (2017).

[161] A. Doostmohammadi et al. Onset of meso-scale turbulence in living fluids, *Nature Communications*, **8**, 15326 (2017).

[162] R. Di Leonardo et al. Bacterial ratchet motors. *Proceedings of the National Academy of Sciences*, **107**, 9541-5 (2010).

[163] A. Sokolov et al. Swimming bacteria power microscopic gears. *Proceedings of the National Academy of Sciences*, **107**, 3 (Jan. 2010).

[164] A. Kaiser et al. Transport Powered by Bacterial Turbulence, *Physical Review Letters*, **112**, 158101 (2014).

[165] A. Kaiser et al. Mechanisms of carrier transport induced by a microswimmer bath, *IEEE Transactions on NanoBioscience*, **14**, 3 (2014).

[166] C. Denniston, E. Orlandini, and J. M. Yeomans. Lattice Boltzmann simulations of liquid crystal hydrodynamics, *Physical Review E*, **63**, 056702 (2001).

[167] J. C. Desplat, I. Pagonabarraga, and P. Bladon. Ludwig: A parallel Lattice-Boltzmann code for complex fluids, (2000). arXiv: `0005213v2`.

[168] S. P. Thampi, R. Golestanian, and J. M. Yeomans. Velocity correlations in an active nematic, *Physical Review Letters*, **111**, 118101 (2013).

[169] A. Thampi, Sumesh Doostmohammadi et al. Intrinsic free energy in active nematics, *Europhysics Letters (EPL)*, **112**, 28004 (2015).

[170] M. L. Blow, S. P. Thampi, and J. M. Yeomans. Biphasic, lyotropic, active nematics, *Physical Review Letters*, **113**, 248303 (2014).

[171] A. J. T. M. Mathijssen et al. Hotspots of boundary accumulation: dynamics and statistics of micro-swimmers in flowing films, *Journal of The Royal Society Interface*, **13**, 20150936 (2016).

[172] G. de Magistris et al. Spontaneous motility of passive emulsion droplets in polar active gels, *Soft Matter*, **10**, 7826-7837 (2014).

[173] S. P. Thampi and J. M. Yeomans. Active turbulence in active nematics, *European Physical Journal: Special Topics*, **225**, 651-662 (2016).

[174] K. B. Petersen and M. S. Pedersen. *The Matrix Cookbook*. 2007.

[175] H. Brenner. Rheology of a dilute suspension of axisymmetric Brownian particles, *International Journal of Multiphase Flow*, **1**, 195-341 (1974).